Theoretical background of optical emission spectroscopy for analysis of atmospheric pressure plasmas

Thierry Belmonte, Cédric Noël, Thomas Gries, Julien Martin, Gérard Henrion

Theoretical background of optical emission spectroscopy for analysis of atmospheric pressure plasmas

Thierry Belmonte[1,2,*], Cédric Noël[1,2], Thomas Gries[1,2], Julien Martin[1,2] and Gérard Henrion[1,2]

[1]Université de Lorraine, Institut Jean Lamour, UMR CNRS 7198, NANCY, F-54042, France

[2]CNRS, Institut Jean Lamour, UMR CNRS 7198, NANCY, F-54042, France

* Corresponding author. Email: thierry.belmonte@univ-lorraine.fr

ABSTRACT

This review contains a theoretical background of optical emission spectroscopy and some selected examples of issues in the field of atmospheric plasmas. It includes elements like line broadening, emission of continua and molecules, radiation models, etc. Modernized expressions figuring the terms hidden in global constants where cgs units prevail are given together with restrictions of use. Easy-to-use formulas are provided to give access to essential plasma parameters.

1. INTRODUCTION

If you have just bought a new spectrometer to diagnose this atmospheric pressure plasma that drives you crazy, you certainly wish to make the most of it. This paper aims at helping a bit in this difficult task that usually takes a while to be mastered, experience being always long to gain. There have been many reference books (*e.g.* (Demtroder 2003), (Griem 1964), (Griem 1974), (Linne 2002), (Thorne *et al* 1999) or (Tkachenko 2006)) on optical emission spectrometry that the reader is invited to delve into for deeper understanding. We shall concentrate here on the inherent issues of optical emission spectroscopy applied to atmospheric pressure plasmas and give some ready-made solutions together with their appropriate conditions of use. *Ab initio* and DFT calculations have brought much to this field recently but they require a specific skill to be applied if they are not made easily available to end-users through tables or abacus. For estimates whose accuracy does not aim to reinvestigate the basic mechanisms of optical spectroscopy, such tools are useless and beyond the scope of this paper.

While preparing this publication, we could notice that formulas are frequently copy-pasted from one work to another, leading to expressions carrying the same typing errors, for instance, or missing terms that make impossible to get even crude estimate of the sought-after quantity. Similar, but not identical, formulas are also spread in the scientific literature which, very conveniently, can be selected on purpose to find suiting or hoped values. Misuse of formulas is not rare either, restrictions of use being often buried with the founding works that established them. Then, it was essential, although nightmarish, to go back to these primary papers to give not only modernized expressions figuring the terms hidden in global constants where cgs units prevail, but also to provide limitations of use that go along.

Atmospheric pressure plasmas can be knotty for several important reasons:

- they host huge gradients,

- they can occupy tiny volumes and when they are confined, surface reactions become non-negligible even though the pressure is high,
- they can be optically thick,
- they are subject to contamination,
- *n*-body collisional processes (with *n*=3 and even 4) are important.

Theoretical guidelines will be presented first. They include elements like line broadening, emission of continua and molecules, radiation models, etc. Easy-to-use formulas are provided to give access to essential plasma parameters. The second main part of this work is devoted to some of these serious interpretation difficulties that are commonly encountered in atmospheric pressure plasmas.

2. THEORETICAL GUIDELINES

2.1. Emission intensity

The intensity I of the light emitted by a given volume per unit time at a frequency ν is related to the intensity recorded by a spectrometer $\tilde{I}$ through the following equation:

$$\tilde{I} = \frac{\Omega}{4\pi} R(\nu) I \tag{1}$$

Ω (expressed in [sr]) is the solid angle through which the emitting volume is observed. $R(\nu)$ is the optical response of the device which is dependent on the wavelength (Figure 1).

Then, the intensity, expressed in [W], of a transition I_{ul} from a higher $|u\rangle$ to a lower $|l\rangle$ state is given by:

$$I_{ul} = A_{ul} h \nu_{ul} V N_u \tag{2}$$

where A_{ul} is the Einstein transition probability of spontaneous emission [s^{-1}], h the Planck constant, ν_{ul} the frequency of the emitted photon [s^{-1}]. V is the emitting volume and N_u is the volume number density of emitting species [m^{-3}] in the $|u\rangle$ state.

For a more detailed description of practical aspects of spectroscopic systems (how to select gratings, subtract the optical response of the spectrometer, set entrance slit aperture, etc.), the reader is referred to the paper of Fanz (2006).

2.2. Types of radiation

2.2.1. Atoms

An atom or ion immersed in a plasma will emit radiation when radiative transitions between various quantum states occur. Bound and discrete energy levels are found below the ionization limit whereas a continuum of levels stands above it (Figure 2).

For hydrogenic ions, the energy level distribution follows the Rydberg formula:

$$E_p = Z^2 \frac{Ry}{1+m_e/m_{pr}}\left(1-\frac{1}{p^2}\right) \approx Z^2 Ry\left(1-\frac{1}{p^2}\right) \tag{3}$$

where Ry is the Rydberg constant and p the principal quantum number. Z is the atomic number. m_e and m_{pr} are the electron and proton masses.

Line radiation occurs for electron transitions between bound levels, leading to line spectra. When a transition from an upper level of principal quantum number u to a lower level l occurs at frequency ν_{ul}, it must satisfy the usual selection rules of spectroscopy.

Recombination (*free-bound*) radiation occurs when an electron in the continuum recombines with the ion. Since the upper level is continuous, the radiation is continuous. However, there is some structure due to the discrete nature of the lower energy levels (the so-called absorption edges). For an electron of mass m_e and velocity v, recombination into state $|u\rangle$ gives:

$$h\nu_{ul} = E_\infty + \frac{1}{2}m_e v^2 - E_u \tag{4}$$

Free-free radiation occurs owing to transitions between two free energy levels. It happens when a moving charge radiates whenever it is accelerated or retarded. Bremsstrahlung is caused by the acceleration of charged particles in the Coulomb field of other charged

particles. The major part of bremsstrahlung is due to electron-ion collisions and, since the initial and final states are continuous, the bremsstrahlung spectrum is also continuous.

2.2.2. Molecules

Molecules can occupy different electronic, vibrational and rotational states. The vibrational levels occupied by a molecule made of two atoms in its electronic level *p* can be described by an anharmonic oscillator.

$$G_p(v)=\left(v+\frac{1}{2}\right)\omega_e(p)-\left(v+\frac{1}{2}\right)^2\omega_e x_e(p)+\left(v+\frac{1}{2}\right)^3\omega_e y_e(p)+\left(v+\frac{1}{2}\right)^4\omega_e z_e(p)+\ldots \quad (5)$$

where v is the vibrational quantum number. ω_e, x_e, y_e and z_e are the harmonic frequency, the first, second and third anharmonicity constants, respectively. The larger the number of terms in this series, the higher the accuracy on the highest vibrational levels.

The ground energy level of a molecule is never null since $E_p=G_p(v=0)$. Concerning the distribution of the rotational levels for given vibrational level and electronic state, one has:

$$F_v(J)=J(J+1)B_v-J^2(J+1)^2D_v+J^3(J+1)^3H_v\ldots \quad (6)$$

J is the quantum number for the total rotational angular momentum. B_v is the energy of a rigid rotator. D_v and H_v are the centrifugal distortion constants. These constants (expressed here in J) can be calculated by using the following expressions:

$$B_v=B_e-\alpha_e\left(v+\frac{1}{2}\right)+\gamma_e\left(v+\frac{1}{2}\right)^2\ldots \quad (7)$$

$$B_e=\frac{h^2}{8\pi^2\mu r_e^2}\ ^{\text{i}} \quad (8)$$

$$\alpha_e=6\frac{\sqrt{\omega_e x_e B_e^3}-B_e^2}{\omega_e} \quad (9)$$

[i] All expressions can be used in cm^{-1}, except this one which becomes: $B_e=\frac{h}{800\pi^2 c\mu r_e^2}$.

$$D_v = D_e + \beta_e\left(v+\frac{1}{2}\right)+\ldots \tag{10}$$

$$D_e = \frac{4B_e^3}{\omega_e^2} \tag{11}$$

$$\beta_e = D_e\left(8\frac{\omega_e x_e}{\omega_e}-\frac{5\alpha_e}{B_e}-\frac{\alpha_e^2\omega_e}{24B_e^3}\right) \tag{12}$$

$$H_v = H_e \tag{13}$$

where α_e, β_e, γ_e, B_e, D_e and H_e are spectroscopic constants (see table 1).

The rotational levels of a given vibrational level v can interpenetrate the rotational levels of the next vibrational level v+1 (Figure 3). Furthermore, the gap in energy between two consecutive rotational levels often increases with J.

The molecular constants are tabulated for most of simple molecules (Hubert and Herzberg, 1979), (NIST 2014), (Rosen 1970). Then, the potential energy curve of any simple molecule, which includes rotational and vibrational energy levels, can be approximated by a Morse potential:

$$V(r) = -G(0)+V_0\left(1-\exp\left(-\beta\left(r-r_e\right)\right)\right)^2 \tag{14}$$

with $\beta = \frac{2\pi}{h}\omega_e\sqrt{\frac{\mu}{2V_0}}$ (in [m]) where μ is the reduced mass of the molecule (in [kg]) and V_0 the dissociation energy of the molecule (in [J]). r_e is the equilibrium internuclear distance (in [m]). Here ω_e in expressed in [J].[ii]

The main issue that comes up here with these formula deals with the maximum number of vibrational and rotational levels. This aspect will be treated hereinafter together with partition functions.

2.3. Total, partial and local thermal equilibrium

[ii] If ω_e is in [cm^{-1}], one has: $\beta = 2\pi\omega_e c\sqrt{\frac{\mu}{2V_0}}$ in [cm].

Let's consider a neutral ionized gas made a hydrogenic species (the problem with non-hydrogenic species being by far more complicated) where the following reversible reactions hold:

Direct process	Reversible reaction		Reverse process
Collisional excitation	$A + e \leftrightarrow A^* + e$	(a)	collisional de-excitation (or superelastic collision)
Collisional ionization	$A + e \leftrightarrow A^+ + e + e$	(b)	3-body recombination
Photoionization	$A + h\nu \leftrightarrow A^+ + e$	(c)	Radiative recombination
Photoexcitation	$A + h\nu \leftrightarrow A^*$	(d)	Spontaneous and stimulated emission

Pairs of inverse processes from (a) to (d) occur in detailed balance and total thermodynamic equilibrium (**T.E.**) is achieved. Then, the Boltzmann-Saha distribution between ionization stages follows the Saha equation:

$$\frac{N_e N_i}{N_{i-1}} = \frac{g_e g_i}{g_{i-1}} \frac{\left(2\pi m_e k_B T\right)^{3/2}}{h^3} \times \exp\left(-\frac{E_i - E_{i-1}}{k_B T}\right) \tag{15}$$

The distribution amongst bound levels (from which the Atomic State Density Function or ASDF is derived) is ruled by a Maxwell-Boltzmann statistics:

$$\frac{N_u}{N_l} = \frac{g_u}{g_l} \times \exp\left(-\frac{E_u - E_l}{k_B T_{exc}}\right) \tag{16}$$

The spectral radiance (in [W sr^{-1} m^{-2} Hz^{-1}]) is given by the Planck function:

$$B_\nu(T) = 2h\frac{\nu^3}{c^2} \frac{1}{\exp\left(\frac{h\nu}{k_B T}\right) - 1} \tag{17}$$

and the normalized electron velocity distribution is Maxwellian:

$$f(v)dv = 4\pi\left(\frac{m_e}{2\pi k_B T_e}\right)^{3/2} \exp\left(\frac{-m_e v^2}{2k_B T_e}\right) v^2 dv \tag{18}$$

where N_e, N_i, N, N_u and N_l are the densities of the electrons, ions, neutral species in a upper and lower excited levels respectively. T_e, T and T_{exc} are the electron, kinetic and excitation temperatures respectively, which are all equal, these distributions being characterized by the same temperature in **T.E.**

For a high density plasma where collisional effects completely dominate radiative ones, thermodynamic arguments can be applied to define the so-called local thermodynamic equilibrium (**L.T.E.**). The same laws that govern the **T.E.**, excepting the one related to radiation, can describe the state of plasma. In other words, there is equilibrium in a weak radiation field, where T_e from the Maxwell distribution is equal to the temperature T from Saha's equation.

The number of excited particles and free electrons decreases with respect to **T.E.** but a new balance ruled by collision processes is reached where radiative emission and recombination processes are negligible. Many discussions have been held to criticize the various necessary though insufficient criteria, usually based on N_e, proposed to account for the **L.T.E.** regime. Electron density required for **L.T.E.**, the plasma being at steady state and homogeneous, is given by Griem (1963):

$$\begin{aligned} N_e\left[cm^{-3}\right] &\geq 10\times\frac{1}{16\sqrt{\pi}}\left(\frac{e^2}{a_0 4\pi\varepsilon_0\eta c}\right)^3 z^7\left(\frac{k_B T_e}{E^i_{H^z}}\right)^{1/2}\left(\frac{Max\left(E_u-E_l\right)}{E^i_{H^z}}\right)^3 \\ N_e\left[cm^{-3}\right] &\geq 9.247\times10^{17}\left(\frac{k_B T_e}{E^i_H}\right)^{1/2}\left(\frac{E_2-E_1}{E^i_H}\right)^3 = 9.247\times10^{17}\left(\frac{k_B T_e}{E^i_H}\right)^{1/2}\left(\frac{E_2}{E^i_H}\right)^3 \end{aligned} \tag{19}$$

z stands here for the effective number of charge (z=1 for neutrals, z=2 for singly charged ions, etc.) $E^i_{H^z} = z^2 E^i_H$. For hydrogen, taking z=1, if T_e = 11604 K, one finds $N_e > 1.0\times10^{17}$ cm^{-3}.

In general, Griem's criterion is too rigorous and yields excessively high electron concentration. This is due to the assumption that resonance radiation escapes the plasma freely, a condition that is never fulfilled in real plasmas, resonance radiation being always strongly reabsorbed. Griem proposed in the same work to reduce the constraint by removing

the factor of 10 he chose to introduce by considering that the resonance lines are indeed optically thick:

$$N_e\left[cm^{-3}\right] \geq 10^{17}\left(\frac{k_B T_e}{E_H^i}\right)^{1/2}\left(\frac{E_2}{E_H^i}\right)^3 \tag{20}$$

Other criteria like McWhirter's:

$$N_e\left[cm^{-3}\right] \geq 1.5\times10^{18}\left(\frac{T_e}{10^6}\right)^{0.55-\left(\frac{0.49}{z}\right)^{3/2}} \tag{21}$$

are commonly referred to but must also be used with caution (see Cristoforetti *et al.* (2010) for a thorough discussion). For atomic hydrogen, if T_e = 11604 K, $N_e > 6.0\times10^{17}$ cm^{-3}, *i.e.* an even higher concentration than that deduced from Griem's formula that usually predicts higher electron densities, but that notoriously gives gross underestimate for H.

Below this critical electron density, collision de-excitation (reverse process of reaction (a)) competes with spontaneous emission (reverse process of reaction (d)). However, both processes do not occur at the same rates for all energy gaps $\left(E_u - E_l\right)$ between excited levels. The excitation/de-excitation by electron impact is more efficient between highly excited levels (inversely proportional to $\left(E_u - E_l\right)$), where $\left(E_u - E_l\right)$ decreases. On the other hand, the radiative decay rate increases with $\left(E_u - E_l\right)$ (see Cristoforetti *et al* (2010) for demonstration). De-excitation by radiative decay is weaker for highly excited levels. Then, when the LTE condition is fulfilled by high-energy excited levels only and not by low-energy levels, the plasma is in partial LTE (**pL.T.E.**). The ASDF contains an upper side where high-energy levels are thermalized, following a Boltzmann distribution and related to the ion population by the Saha equation, and a lower side, where levels do not follow the Boltzmann-Saha distribution. The experimental determination of T_{exc} by using a Boltzmann plot will give values different from T_e.

The electron density required for the p^{th} level to be in equilibrium with the higher levels and the continuum, *i.e.* to have **pL.T.E.** above level *p*, is given by Griem (1963):

$$N_e\left[cm^{-3}\right] \geq \frac{10}{2\sqrt{\pi}}\left(\frac{e^2}{a_0^2 4\pi\varepsilon_0 \eta c}\right)\frac{z^7}{p^{17/2}}\left(\frac{k_B T_e}{E^i_{H^z}}\right)^{1/2} = 7.351\times10^{18}\frac{z^7}{p^{17/2}}\left(\frac{k_B T_e}{z^2 E^i_H}\right)^{1/2} \qquad (22)$$

where *p* is the principal quantum number of the lowest level included in the partial LTE and *z* the effective charge seen by the bound electron.

Example: For hydrogen, if T_e = 11604 K (*i.e.* 1 eV) and taking *p*=2, one finds $N_e > 5.5\times10^{15}$ cm^{-3}.

Fujimoto and McWhirter (Fujimoto and McWhirter 1990) divide **pL.T.E.** plasmas in 3 classes: recombining, ionizing, or in ionization balance. A recombining (respectively ionizing) plasma is defined as one where the population density of the ground state is lower (respectively greater) than the value it would have if the ionization balance was satisfied, the ionization-balance plasma being defined by the equality condition. In each situation, the excited level above which levels are in **pL.T.E.** can be estimated theoretically from expressions available in (Fujimoto and McWhirter 1990).

Because of the development of ultrafast power generators, it is worth giving here an estimate of the minimum time required to establish the excitation and ionization equilibria in transient plasmas. By assuming a sudden departure from the quasi-stationary **L.T.E.** condition, the time τ_{rel} needed by the atomic system to return to **L.T.E.** is given by the characteristic time of the slowest process, which corresponds to collisional excitation to the first excited level. After Griem (1963), one has:

$$\begin{aligned}\tau_{rel} &\approx \frac{1}{8\sqrt{\pi}}\left(\frac{4\pi\varepsilon_0\eta c}{e^2}\right)\frac{1}{a_0^2 c}\frac{z^3}{f_{12}}\frac{\alpha}{N_e}\frac{E_2}{E^i_{H^z}}\left(\frac{k_B T_e}{E^i_{H^z}}\right)^{1/2}\exp\left(\frac{E_2}{k_B T_e}\right)\\ \tau_{rel} &\approx 1.151\times10^{13}\frac{\alpha}{f_{12}N_e}\frac{E_2}{E^i_H}\left(\frac{k_B T_e}{E^i_H}\right)^{1/2}\exp\left(\frac{E_2}{k_B T_e}\right)\end{aligned} \qquad (23)$$

where α is the fraction of ionization for the selected atom.

Example (Griem 1963): Taking $N_e=10^{22}$ m^{-3} as determined from Eq.(20), T_e=11604 K, $E_2=1.635\times10^{-18}$ J (10.2 eV) for H and f_{12}=0.83, one finds using the Saha equation (Eq. (15)), $\alpha \approx 0.43$ and thus: $\tau_{rel} \approx 3.2$ µs.

Other expressions, a bit more accurate, were derived (see *e.g.* Christoforetti *et al.* 2010).

Finally, another limit case is the so-called "**coronal approximation**" (Cooper 1966). This equilibrium occurs when the electron density is too small to achieve the complete LTE. Then, the relative populations of high energy levels are controlled by the collisions between particles. Radiation absorption and photoionization (processes (d) and (c)) are unimportant as well as three-body recombination (process (–b)). Under these conditions, ionization equilibrium is a balance between collisional ionization and radiative recombination, and the actual populations depend critically on the cross sections for the processes.

2.4. Partition functions

The total partition function of a species is the sum of several contributions, including translation, internal and reaction components, the second one being the sum of the electronic, vibrational and rotational partition functions for a molecule or simply the electronic partition function for an atom.

$$Q_{tot} = Q_{trans} + \underbrace{Q_{\text{int}}}_{Q_{elec}+Q_{vib}+Q_{rot}} + Q_{reac} \tag{24}$$

The translation term is:

$$Q_{trans} = \left(\frac{2\pi m k_B T}{h^2} \right)^{3/2} \frac{k_B T}{P} \tag{25}$$

Let's focus now on the internal partition function.

2.4.1. Internal partition functions of atoms

For atoms, it is given by:

$$Q = Q_{\text{int}} = \sum_{j=1}^{p} g_{j(n,l,s)} \exp\left(\frac{-E_j(n,l,s)}{k_B T}\right)^{\text{iii}} \tag{26}$$

where g_j are the statistical weights of the energy levels lying at $E_j(n,l,s)$. p is the number of states to consider. It cannot be infinite otherwise the partition function would tend towards infinity. There are several ways to reduce the number of energy levels to consider in the aforementioned sum.

Using the criterion that no Rydberg states' mean radius should exceed the mean distance between particles, Mihalas (1978) estimated:

$$n_{\max} \approx 30\sqrt{z}\left(N/10^{21}\right)^{-1/6} \tag{27}$$

where N is the total number density (in [m^{-3}]). z is the effective number of charges.

Alternatively, it turns out that temperature as well as pressure can affect the partition function, because of the lowering of the ionization energy. This lowering can be estimated by the Debye-Hückel theory. This theory also applies to determine the energy of possible missing levels in a distribution. The Ritz-Rydberg distribution is given by:

$$E_p = E_i - \frac{Ry}{\left(p + A + \frac{B}{p^2}\right)^2} \quad ; \quad p < p_{\max} \tag{28}$$

where E_i is the ionisation energy, Ry, the Rydberg constant, p the principal quantum number and A and B two constants. Here, p_{max} is the number whose Ritz-Rydberg's energy is inferior to the ionization energy corrected by ΔE^{ion} due to charged particles effects:

$$\Delta E^{ion} = \frac{ze^2}{4\pi\varepsilon_0\lambda_D} \tag{29}$$

z is the effective number of charge. λ_D is the Debye length:

[iii] We just recall here that internal partition functions of doubly ionized helium, protons and electrons are respectively $Q(He^{2+})=1$, $Q_{pr}=1$ and $Q_e=2$.

$$\lambda_D = \left(\frac{1}{\varepsilon_0 k_B} \frac{\sum_{i=1}^{M} q_i^2 N_i}{T} \right)^{-1/2} \tag{30}$$

where q_i is the elementary charge of species i among the M existing charged species and N_i the number density of this species. Then, the partition function is composition-dependent via the Debye length.

Example: For atomic hydrogen, the internal partition function reads:

$$Q_{\text{int}}^H = \sum_{p=1}^{\infty} 2p^2 \exp\left(\frac{-E_{ion}^H \left(1 - \frac{1}{p^2}\right)}{k_B T} \right) \tag{31}$$

This expression diverges when $p \to \infty$. The cut-off is made by resorting to the lowering of the ionization energy. The maximum value of p is given by $E_{ion}^H \left(1 - \frac{1}{p^2}\right) \geq E_{ion}^H + \Delta E^{ion}$ where E_{ion}^H is the ionization energy of hydrogen.[iv] Then, if P=101325 Pa and T=11,604 K, one finds $\Delta E^{ion} = 0.154$ eV, p~10 (Eq.(27) gives also p~10) and $Q_{\text{int}}^H = 2.0017$.

2.4.2. Internal partition functions of molecules

We use the method of the Morse potential to estimate the partition function. One has:

$$Q_{\text{int}} = \sum_{p=1}^{Ne} \left\{ g_p \exp\left(\frac{-E_p}{k_B T} \right) \times \sum_{v=0}^{Nv} \left\{ g_v \exp\left(\frac{-G_p(v)}{k_B T} \right) \times \sum_{r=0}^{Nr} G(S)(2J+1) \exp\left(\frac{-F_v(J)}{k_B T} \right) \right\} \right\} \tag{32}$$

This sum is not complete because it has to include several other contributions: multiplets, Λ–doubling and the hyperfine nuclear structure. The last two give negligible contributions above 1000 K. The first one must be calculated for multiplet states (doublet, triplet, quadruplet, etc.)

[iv] We have to use $E_{ion}^H = \frac{Ry}{1 + m_e / m_{pr}}$ =13.5984337 eV (and not 13.60569253 eV – See Eq. 3) to find the correct energy levels for hydrogen.

For the electronic term, one has:

$$g_p = (2 - \delta_{0,\Lambda})(2S+1) \tag{33}$$

g_p includes the angular and the spin degeneracy. Λ=0 for a Σ state ($\delta_{0,\Lambda}$=1) and $\Lambda \neq 0$ for the others. Except for a few molecules, $g_v = 1$. Otherwise, $G(S)$ is a factor G(S) that accounts for the symmetry and spin considerations which are described in (Denton 1977) for instance.

Concerning the issue of cut-off values for vibrational and rotational distributions, maximum energy levels can be determined by *ab initio* calculations. In most cases, other straightforward approximations can be used. For example, the maximum vibrational quantum number v can be determined as the greatest integer less than the zero of $\partial G(v)/\partial v$ near $v \approx \omega_e/(2\omega_e x_e) - 0.5$ or the zero of B_v near $v \approx B_e/\alpha_e - 0.5$, which excludes unacceptable negative values of v.

For the rotational levels, Irwin (1987) suggests to use the semi-classical linear interpolation law by Khachkuruzov (1967, 1971) as follows:

$$J_{\max}(v) \approx \left(1 - \frac{v}{v_{\max}}\right) J_{\lim} \tag{34}$$

$J_{\lim}$ is the maximum possible rotational quantum number for a Hulbert-Hirschfelder molecular potential.

Most of the partition functions for atoms and simple molecules are also tabulated as a function of the electron temperature (*e.g.* NIST 2014) and usually for a given value of $\Delta E^{ion} = 0.1$ eV (*e.g.* Irwin 1981).

2.5. Temperatures

The rotational temperature of a molecule is often used as a probe of the gas temperature. Indeed, the difference in energy between rotational levels in a molecule is weak, a few hundredths eV, which is in the order of the gas temperature (300 K = 0.0259 eV). In atmospheric pressure plasmas, rotation-translation energy transfers have a high occurrence probability because of the very high neutral concentration. For instance, for nitrogen plasmas

at 2500 K, the neutral-neutral collision frequency is about 10^9 Hz. The optical transition frequency of OH, for instance, is about 10^6 Hz, *i.e.* 3 orders of magnitude lower. This difference usually ensures the consistency between the rotational temperature of the probe molecule and of nitrogen at the spot where radiation is emitted because OH molecule have time to be thermalized before an optical transition happens. According to (Jain 1980), the number of collisions required to reach equilibrium is only 25 in nitrogen. For another molecule like $N_2(C^3\Pi_u)$, the optical transition frequency increases to 2.5×10^8 Hz (Gazeli *et al.* 2013) and it is hit only 4 times in average before deexcitation[v]. So, its rotational temperature will be defined by the way $N_2(C^3\Pi_u)$ is created and not by the equilibrium it could have with colliding species. However, it turns out that the case of $OH(A^2\Sigma^+)$ is more complicated. Indeed, this molecule can undergo an efficient quenching depending on the buffer gas. If the following reaction is considered:

$$OH(A^2\Sigma^+, v'=0) + N_2 \rightarrow OH(X^2\Pi, v''=0) + N_2 \qquad \text{(e)}$$

with a rate constant $k_e=2.5\times10^{-11}$ cm^3 s^{-1}, the mean transition frequency of OH(A) is now $\sim7\times10^7$ Hz. The number of non-quenching collisions of the $OH(A^2\Sigma^+)$ state are limited to about 14 only. Furthermore, the value of k_e also depends on the rotational level J (see Figure 4) and, depending on the conditions, some levels can be in equilibrium and others cannot.

Simulation of rotational spectra can be achieved with commercial software (Specair 2014, Lifbase 2014). They are generally limited to one rotational temperature. If the rotational states are in equilibrium, they are distributed according to a Boltzmann law:

$$N_u = \frac{N_0 g_u}{Q(T_r)} \exp\left(-\frac{E_u}{k_B T_r}\right) \qquad (35)$$

N_u *and* N_0 are the numbers of molecules in level $|u\rangle$ and in the ground state respectively, $Q(T_r)$ is the partition function, which depends on the rotational temperature T_r [K], g_u is the

[v] At 300 K, the number of collisions of $N_2(C^3\Pi_u)$ is ~33 and equilibrium can be reached.

statistical weight of level $|u\rangle$, E_u the energy of this level and k_B the Boltzmann constant. Then, Eq.(35) combined with Eq.(1) and (2) can be linearized, which gives easily:

$$\ln\left(\frac{\tilde{I}_{ul}}{A_{ul}h\nu_{ul}}\right)=\left(-\frac{1}{k_BT_r}\right)E_u-\ln\left(\frac{4\pi Q(T_r)}{N_0 g_u V\Omega R(\nu)}\right) \qquad (36)]$$

If the temperature is constant, N_0, g_p and $Q(T_r)$ are constant. By measuring several transitions whose data (A_{ul}, ν_{ul} and E_u) are known, T_r is readily determined from the slope (equal to $-\frac{1}{k_BT_r}$) of the straight line obtained in a Boltzmann plot where $\ln\left(\frac{\tilde{I}_{ul}}{A_{ul}h\nu_{ul}}\right)=f(E_u)$.

This method is strictly equivalent to spectra simulation, but it is more convenient to determine any discrepancy to equilibrium, especially if two or more temperatures are needed. An example is given in Figure 5.

2.6. Line broadening and shift

For sake of clarity, neither the Half Width at Half Maximum (HWHM), often referred to in publications, nor the Half Half Width at Half Maximum (HHWHM) will be used. Only the Full Width at Half Maximum (FWHM) will be considered. All formulas are given in SI units.

2.6.1. Common line profiles

Line broadening is a very complex topic. We give in this short notice a simplified view for practical use and the reader is invited to comply with the conditions of use prescribed hereinafter.

An emission line is not infinitely thin and it is always naturally broadened. Natural broadening arises because even an unperturbed level has a finite lifetime due to spontaneous emission (in quantum mechanical terms, this is due to Heisenberg's uncertainty principle). The shape of the line is then Lorentzian. It means that the distribution of a *normalized* intensity in wavelength follows the behaviour:

$$L(\nu)=\frac{2}{\pi}\left[\frac{\Delta\nu_L}{\Delta\nu_L^2+4(\nu-\nu_0\pm\nu_s)^2}\right] \qquad (37)]$$

where is $\Delta\nu_L$ the Full Width at Half Maximum (FWHM) of the Lorentzian profile, ν_0 is the central wavelength and ν_s the line shift.

$$\Delta\nu_L = \frac{1}{2\pi}\left[A_{u\rightarrow} + A_{l\rightarrow}\right] \tag{38}$$

$A_{u\rightarrow}$ and $A_{l\rightarrow}$ are the total spontaneous transition probability of levels *u* and *l* to any allowed lower levels, respectively. Nevertheless, natural broadening is very weak (of the order of several tens of MHz, *i.e.* < 10^{-4} nm) and almost always neglected. In general, the shape, the width and the central wavelength of a line may vary under the influence of various convolved effects. When the line profile is Gaussian, it is described once normalized by:

$$G(\nu) = \frac{1}{\Delta\nu_G}\sqrt{\frac{2\ln(4)}{\pi}}\exp\left(-2\ln(4)\frac{(\nu-\nu_0\pm\nu_s)^2}{\Delta\nu_G^2}\right) \tag{39}$$

where is $\Delta\nu_G$ the FWHM of the Gaussian profile.

The Voigt profile is often used to account for the simultaneous presence of various Lorentzian and Gaussian contributions. It reads:

$$V(\nu,\Delta\nu_L,\Delta\nu_G) = \int_{-\infty}^{+\infty} G(x,\Delta\nu_G)\cdot L(\nu-x,\Delta\nu_L)dx \tag{40}$$

In a Voigt profile including several Gaussian and Lorentzian contributions, the following relations apply:

$$\Delta\nu_{G,tot}^2 = \Delta\nu_V\left(\Delta\nu_V - \Delta\nu_{L,tot}\right);\ \Delta\nu_{G,tot}^2 = \sum_i \Delta\nu_{G,i}^2\ ;\ \Delta\nu_{L,tot} = \sum_j \Delta\nu_{L,j} \tag{41}$$

It is often convenient to use the following approximation (accuracy better than 0.02%):

$$\Delta\nu_V = 0.5346\times\Delta\nu_{L,tot} + \sqrt{0.2166\times\Delta\nu_{L,tot}^2 + \Delta\nu_{G,tot}^2} \tag{42}$$

We easily understand here that the main issue in interpreting line profiles stems from the convolution of several phenomena in one single profile that can be described through 3 main parameters: the FWHM, the line shift and the line shape. Concerning the FWHM, its determination can be accurate. The line shift, because it is often limited in practice, requires

usually an evolution as a function of a user parameter like time or pressure to be assessed properly. Concerning the line shape, it can easily be misconstrued. In Figure 6, an example is given showing Gaussian and Lorentzian lines to which a baseline was added in order to simulate a background emission. In the linear-scale, we notice that both lines, even without noise, are close to each other. Using a log-scale can help remove the uncertainty, this process enhancing the contribution of the wings.

2.6.2. Broadening sources

The presence of particles in the vicinity of a radiator (understand a particle that radiates light, also called an emitter) affects the emitted radiation. There may be an associated shift in wavelength. There are two major approximations made in the classical theory used to describe line profiles when such a situation occurs:

- The *impact approximation* is used when the interaction is short enough to be neglected (the emitter is most of time unperturbed except at impact). This approximation is valid at low density and for the central part of the line. This effect depends on both the density and the temperature of the gas.
- In the *quasistatic approximation*, perturbers are considered at rest. This effect depends on the density of the gas, but is rather insensitive to temperature. Perturbation is assumed to be constant in time, contrary to the impact approximation. The quasistatic approximation is valid only at high density or for the wings of the line where the time of interest ($1/\Delta\omega$, the reciprocal of the circular frequency of radiation) is much less than the duration time for a collision.

The emergence of these two distinct theories is worth being told briefly. Historically, Lorentz provided the first quantitative theory in 1906 (*i.e.* the basis of the impact approximation) (Lorentz 1906). He considered that the broadening was due to the interruption by collision of a wave train that is unperturbed during the time between collisions. This theory yields

dispersion profiles with line width that are essentially equal to the frequency of collision. Weisskopf advanced this description to the impact theory in 1932 (Weisskopf 1932). He gave a more satisfactory description by considering the broadening cause as the change in phase of the emitted radiation. Meanwhile, Holtsmark adopted a radically opposite view (Holtsmark 1919). He expressed in 1919 the probability $P(\beta)$ to have a field strength E corresponding to the sum of the elementary fields E_i generated by N_i particles in the plasma. β is simply equal to E/E_n, where E_n is defined as the "normal" field strength ($E_n = 2\pi e(4N_i/15)^{2/3}$). The static microfield distribution is given by:

$$P(\beta) = \frac{2}{\pi}\beta\int_0^\infty x\sin(\beta x)\exp\left(-x^{3/2}\right)dx \tag{43}$$

Let us assume that a spectral line is emitted at the time when the field E exists. It will split the line according to the Stark effect. Let the intensity in this split line be given by:

$$Id\nu = I(E,\nu)d\nu \tag{44}$$

I is the intensity in any relative units for the frequency ν and the field strength E. If we multiply this intensity distribution by the probability for the field strength E and integrate over all E, we obtain the intensity distribution in the broadened line as follows:

$$Id\nu = d\nu\int_0^\infty I(\beta,\nu)P(\beta)d\beta \tag{45}$$

$P(\beta)$ can be developed in series expansions at small and large values of the argument β. The Holtsmark distribution gives the probability to find a definite value E of the electric microfield at a fixed given location in an ideal plasma. This model, belonging to the quasistatic approximation, gave good results although correlations between particles are completely neglected.

Since then, physical models of plasma microfields, including DFT and MD simulations, have become much more sophisticated (see (Demura 2010) for instance for a thorough review),

enabling the prediction of complex line profiles. Broadening of spectral lines is a time-dependent many-body problem that cannot be solved exactly. There is no practical theory that leads to the full static profile in the limit of high density (or low temperature) and to the full impact profile in the limit of low density (or high temperature). It is the intermediate situation that is difficult to describe, because no particular feature can be singled out as providing a weak perturbation on a known physical situation (Peach 1996).

As far as the impact approximation is valid, Lorentz profiles are expected. Otherwise, the shape of the line can be very different. For a given potential $V_n = -C_n / r^n$, Hindmarsh *et al.* (1970) defined the validity of the impact approximation by:

$$\rho_w \approx \left(\frac{2\pi C_n}{\bar{v}} \right)^{\frac{1}{n-1}} << \left(\frac{1}{N_p} \right)^{\frac{1}{3}} \tag{46}$$

The hand-left side term, ρ_w is known as the Weisskopf radius. $\bar{v} = \sqrt{8k_B T / (\pi m_u \mu)}$ is the thermal velocity, μ being the reduced mass of the radiator/pertuber system and m_u the atomic mass unit. N_p is the number density of pertubers.

The most commonly encountered broadening sources are:

2.6.2.1. Stark broadening

Although it is possible to consider Stark broadening as a specific pressure broadening (Griem 1964, see p 63), we choose here to present it separately for it implies charge species, so as to avoid confusing early-stage researchers.

The Stark profiles of atomic lines in plasma are produced predominantly under the action of high-frequency fields of electrons (the linear Stark effect, which causes a shift in energy which is linear in the field strength with $V_2 = -C_2 / r^2$) and marginally under the action of the low-frequency fields of ions (the quadratic Stark effect, which causes a shift in energy which is quadratic in the field strength $V_4 = -C_4 / r^4$).

Theoretical descriptions usually combine the quasi-static approximation for ions whose contribution is weak, and the impact approximation for electrons that are the main source of line broadening (see after the specific case of H). The distribution of fields in some plasmas can smear out the line shifts and the neutral atom line is then unsymmetrically broadened.

The shape and the associated shift of transitions belonging to the Balmer serie of hydrogen ($n_u > n_l = 2$), helium II and some light and medium elements were measured and fitted by Griem (Griem 1964). Approximate formulas, resorting to parametric functions, were derived for an easier use. They are reasonably accurate if $0.05 \le \alpha \le 0.5$ and $r \le 0.8$, these two quantities being defined hereafter. The line width broadened by Stark effect is given by:

$$\Delta\lambda_s = 2\left[1+1.75\alpha\left(1-0.75\kappa r_D\right)\right]w \tag{47}$$

where $w(T_e, N_e)$ and $\alpha(T_e, N_e)$ are two parametric functions tabulated by Griem (1964). They represent the electronic contribution expressed in wavelength and the ion quasi-static broadening parameter. They scale respectively as N_e and $N_e^{1/4}$. So, they are more conveniently written as $w\left(T_e, N_e\right) = \frac{N_e}{N_e^0} w_e\left(T_e\right)$ and $\alpha\left(T_e, N_e\right) = \left(\frac{N_e}{N_e^0}\right)^{1/4} a\left(T_e\right)$ where w_e and a are dependent on T_e only. N_e is the electron density and $N_e^0 = 10^{22}$ m^{-3}. $r_D = \rho_m / \lambda_D$ is the Debye shielding parameter. It is the ratio of the mean distance between ions $\rho_m = \left(\frac{4}{3}\pi N_e\right)^{-1/3}$ and the Debye radius $\rho_D = \sqrt{\frac{\varepsilon_0 k_B T_e}{e^2 N_e}}$. $r_D \approx 8.899\times10^{-3} N_e^{1/6} T_e^{-1/2}$. κ is a constant equal to 1 for a neutral emitter and 1.6 for an ion emitter. Equation (47) reads:

$$\Delta\lambda_s = 2\times10^{-22}\left[1+5.534\times10^{-6} N_e^{1/4} a\left(T_e\right)\left(1-6.742\times10^{-3}\kappa N_e^{1/6} T_e^{-1/2}\right)\right] N_e w_e\left(T_e\right) \tag{48}$$

or, expressed in frequency (in [Hz]):

$$\Delta\nu_s = 2\times10^{-22}\frac{\nu_0^2}{c}\left[1+5.534\times10^{-6} N_e^{1/4} a\left(T_e\right)\left(1-6.742\times10^{-3}\kappa N_e^{1/6} T_e^{-1/2}\right)\right] N_e w_e\left(T_e\right) \tag{49}$$

Here, ν_0 is the central frequency of the unperturbed line. The line shift is given by:

$$d_s = d \pm 2\alpha\left(1 - 0.75\kappa r_D\right)w \tag{50}$$

$d(T_e, N_e)$ is a parametric function tabulated by Griem (1964). It represents the electron impact shift (expressed in m). It scales as N_e and it is usually written as $d\left(T_e, N_e\right) = \frac{N_e}{N_e^0} d_e\left(T_e\right)$.

$$d_s = 1\times10^{-22}\left[\frac{d_e}{w_e} \pm 6.325\times10^{-6} N_e^{1/4} a\left(T_e\right)\left(1 - 6.742\times10^{-3}\kappa N_e^{1/6} T_e^{-1/2}\right)\right] N_e w_e\left(T_e\right) \tag{51}$$

The sign $\pm$ is equal to that of the low-velocity limit for d_e. As line profiles are asymmetric, the shift at half width is different from the line shift and it can be determined by multiplying the term 6.325×10^{-6} by 1.6. Griem's tables (Table 4.5 p 454 and Table 4.6 p 507 in (Griem 1964)) give w_e (in [Å]), a and d_e/w_e between T_e=2,500 and T_e=80,000 K for visible and UV lines of neutral and singly ionized atoms from helium to calcium. Several reviews of experimental Stark widths and shifts for spectral lines of neutral and ionized atoms are also available (Konjević and Roberts 1976, Konjević *et al.* 2002) and can be used.

Example: The Ar I transition (4s'-5p') at 425.936 nm is broadened by Stark broadening. One gives N_e=1.7×10^{22} m^{-3} and T_e=10120 K. From Griem's tables, one finds w_e =1.24×10^{-11} m, a=0.032 and d_e/w_e =0.604. Then $\Delta\nu_s$ =7.26×10^{10} Hz (*i.e.* $\Delta\lambda_s$ =0.044 nm) and d_s=0.0137 nm. In this example, experimental values recommended by Konjević *et al.* (2002) are $\Delta\lambda_s$ =0.035 nm and d_s=0.0190 nm.

The specific case of hydrogen lines

In the specific case of hydrogen lines, which are extremely useful for plasma diagnosis purposes, profiles exhibit complex shapes so that the central part and the wings of the lines must be described with different functions. Roughly, a lorentzian distribution is needed for the

former (impact approximation for electrons) and a Holtsmark distribution for the latter (quasi-static approximation for ions). The Holtsmark distribution is given by:

$$H(\beta) = \frac{2}{\pi\beta}\int_0^\infty x\sin(\beta x)\exp\left(-x^{3/2}\right)dx \tag{52}$$

where $\beta = \frac{F}{F_0}$ is the ratio of the electric field strength and the normal field strength. This integral must be calculated numerically. Approximated formulas exist and we refer the reader to other articles (see *e.g.* Sapar *et al.* 2006) for this. As a consequence, tables were built to assess conveniently Stark broadening.

From a practical point of view, the most useful tables are Griem's. They were based on the quasistatic approximation for the ion microfield and the impact approximation for the electron microfield. The ion dynamics effects and some couplings between the two microfields have been taken into account by Gigosos and Cardeñoso (Gigosos and Cardeñoso 1996). More advanced and accurate tables, based on the accurate analytical treatment of the ion dynamics and of all couplings between the ion and electron microfields, were published by Oks in 2006 (Oks 2006). We describe briefly these three main approaches because of the specific importance of hydrogen lines for plasma diagnostics.

It is possible to determine the FWHM of these lines (and then the electron density) by comparing the experimental line profile with tabulated profiles. Stark profiles of the Balmer series Hα, Hβ, Hγ and Hδ, together with Lα and Lβ from the Lyman series were proposed by Griem (Griem 1964) and by Vidal *et al.* (Vidal *et al.* 1973) who added Lγ and Lδ lines. Griem's tables and Vidal's tables can be used as follows. Let α be the quantity:

$$\alpha = 10^{10}\left(\frac{\lambda - \lambda_0}{F_0}\right) \tag{53}$$

where λ_0 is the central wavelength of the unshifted line and F_0 the normal field strength for singly charged ions:

$$F_0 = \frac{10^4}{c}\frac{e}{4\pi\varepsilon_0}\left(\frac{4\pi}{3}N_i\right)^{2/3}$$ [vi] (54)

The reduced Stark profile $S(\alpha)$ is tabulated for $10^{22} \le N_e \le 10^{25}$. If T_e is known and stands between T_e=10,000 and T_e=40,000 K, varying α describes the S profile. An example for Hα and Hβ is provided in Figure 7.

An easier way to estimate the FWHM is to resort to Kepple-Griem's relation (Kepple and Griem 1968):

$$\Delta\lambda_s = 2.5\times10^{-23}\alpha_{1/2}N_e^{2/3} \quad (55)$$

where the $\alpha_{1/2}$ constant is tabulated in (Kepple and Griem 1968).

A set of tables of the Stark width of the first three lines of Lyman and Balmer series of hydrogen, was provided by Gigosos and Cardeñoso in 1996 (Gigosos and Cardeñoso 1996). These tables are available for N_e between 10^{20} m^{-3} and ~10^{25} m^{-3} and T_e between 2,245 K and 224,856 K for different reduced masses of the emitter-perturber pair μ in the range 0.5-2.0 amu. Their utilization is straightforward and convenient.

More recently, Oks (2006) proposed advanced Stark Broadening Tables, based on an accurate analytical treatment of the ion dynamics and of all couplings between the ion and electron microfields, completing the works by Gigosos and Cardeñoso (Gigosos and Cardeñoso 1996) and by Gigosos, González and Cardeñoso (Gigosos *et al.* 2003) where the ion dynamics and some but not all of the couplings between the two microfields have been taken into account. The reader is referred to Oks' papers for very accurate profiles.

We clearly observed from Figure 7 that the various expressions given above provide rough estimates for the Hα line, whereas it is by far better for the Hβ line (and even better for the

[vi] In CGS, this expression becomes $F_0 = e\left(\frac{4\pi}{3}N_i\left[cm^{-3}\right]\right)^{2/3} \approx 2.6eN_i^{2/3}$ with e = 4.8×10^{-10} statC. A more pratical expression than equation (54) is then $F_0 = 1.25\times10^{-9}\left(N_i\left[cm^{-3}\right]\right)^{2/3}$.

next transitions of the Balmer series). The Hα line is affected by high self-absorption levels and the oldest model do not agree so well with the experiments. Recent approaches, including the ion dynamics effects – which reveal themselves as very important in this line – take into account the temporal behaviour of the microfield and then give better values. Yet, it is still much accurate to use the Hβ transition if available.

2.6.2.2. Pressure broadening

According to the operating force, pressure broadening is named:

Resonance broadening

It occurs for transitions involving a level that is *dipole-coupled to the ground state* (*i.e.* the upper or lower level having an electric dipole transition and the corresponding force derives from the potential $\Delta V = \eta C_3 / r^3$). For instance, if the Ar(4s[3/2]° – 4p[3/2]) transition at 369.945 THz (λ_0 = 810.37 nm) is considered, the lower level 4s[3/2]° is coupled to the ground state via the resonance transition Ar($3p^6\ ^1S$ – 4s[3/2]°) at 2810.47 THz (λ_{res} = 106.67 nm). Because of this, the following transitions must be considered: $g \to l$; $g \to u$ and $l \to u$ where *g*, *l* and *u* are the ground, upper and lower levels.

When present, the resonance broadening is usually the dominant effect and at low densities the shape is Lorentzian. The FWHM is given by:

$$\Delta\nu_{res} = \frac{2}{4\pi\varepsilon_0}\frac{e^2}{8m_e}\left[\frac{k_{gl}f_{gl}}{\nu_{lg}}\sqrt{\frac{g_g}{g_l}}N_g + \frac{k_{gu}f_{gu}}{\nu_{ug}}\sqrt{\frac{g_g}{g_u}}N_g + \frac{k_{lu}f_{lu}}{\nu_{ul}}\sqrt{\frac{g_l}{g_u}}N_l\right]^{\text{vii}} \qquad (56)$$

[vii] We find different available expressions where $\frac{e^2}{8m_e}$ (*e.g.* Malvern *et al.* 1980) in Eq. (56) is replaced by $\frac{e^2}{m_e\pi}$ (*e.g.* Lewis *et al.* 1969), $\frac{e^2}{2\sqrt{3}m_e\pi}$ (*e.g.* Laporte and Damany 1979 or Rival *et al.* 1993), $\frac{3}{4}\frac{e^2}{m_e\pi}$ (*e.g.* Griem 1964) or $\frac{3}{8}\frac{e^2}{m_e\pi}$ (*e.g.* Xiong *et al.* 2011).

Noting J and J' the angular momenta of levels j and j' of the transition $j \rightarrow j'$ (g_j = 2J+1 and $g_{j'}$ = 2J'+1 being their respective statistical weights), $k_{jj'}$ is a numerical constant which is known for each transition and close to 1. $f_{jj'}$ is the absorption oscillator strength. $\nu_{jj'}$ is the frequency of the transition. N_j is the number density of level j. The second and third terms of the previous equation are usually small and then, one has:

$$\Delta\nu_{res} = \frac{2}{4\pi\varepsilon_0}\frac{e^2}{8m_e}k_{gl}\sqrt{\frac{g_g}{g_l}}\frac{f_{gl}}{\nu_{lg}}N_g \text{ [viii]} \tag{57}$$

The link with the coefficient $C_{3,gl}$ [in J·m^3] is readily derived from:

$$C_{3,gl} = \frac{\eta}{4\pi}\frac{1}{4\pi\varepsilon_0}\frac{e^2}{m_e}\frac{f_{gl}}{\nu_{lg}} \tag{58}$$

and equation (57) reads:

$$\Delta\nu_{res} = \pi k_{gl}C'_{3,gl}\sqrt{\frac{g_g}{g_l}}N_g \tag{59}$$

by introducing $C'_{3,gl}\left[m^3\cdot s^{-1}\right] = \frac{C_{3,gl}\left[J\cdot m^3\right]}{\eta}$.

$C_{3,gl}$ is related to Einstein's coefficient for spontaneous emission A_{lg} by $C_{3,gl} = \frac{\eta}{32\pi^3}\frac{c^3}{\nu_{gl}^3}\frac{g_l}{g_g}A_{lg}$ with $f_{gl} = \frac{4\pi\varepsilon_0}{8\pi^2}\frac{c^3 m_e}{e^2\nu_{lg}^2}\frac{g_l}{g_g}A_{lg}$. [ix]

Resonance broadening usually results in unshifted dispersion (Lorentz) profiles (Griem 1964).

Example (Malvern et al. 1980): The helium He I (1*s*3*s* ^{1}S$_0$-1*s*2*p* ^{1}P$_1$) transition at 728.135 nm is affected by the resonance transition at 58.433 nm from the He(1*s*2*p* ^{1}P$_1$) state down to the ground state, *i.e.* the He I (1*s*2*p* ^{1}P$_1$-1*s*^{2} ^{1}S$_0$) transition. Considering a density N_g=10^{24}

[viii] Note here that it is indeed the ground state and the lower state of the transition that must be chosen (and not the upper and lower states).

[ix] We remind here that $f_{gl} = \frac{g_g}{g_l}f_{lg}$.

m^{-3}, k_{gl}=1.53, f_{gl}=0.27625, one finds with g_g=3 and g_l=3, $C'_{3,gl}$ =1.085×10^{-15} m^3 s^{-1}. Then, $\Delta\nu_{res}$ =5.216×10^9 Hz (*i.e.* $\Delta\lambda_{res}$ =0.00923 nm). This gives $\Delta\nu_{res}/N_g$ =5.216×10^{-15} Hz m^3 to be compared to 4.617×10^{-15} Hz m^3 which is the experimental value determined by Malvern *et al.* (1980).

Collisional broadening

The excited atom interacts with a ground-state atom of a background *rare gas* by inducing a dipole in the latter through a short-range interaction. The polarized rare gas atom affects in return the energy levels of the excited atom. The evaluation of the short range interaction is important. The first works by Hindmarsh and Thomas (Hindmarsh and Thomas 1961) were made on argon using a Van der Waals potential $\Delta V = \eta C_6/r^6$. Next, there have been a number of attempts to improve on this formalism by replacing the $1/r^6$ dependent van der Waals potential by a more realistic interaction potential. Behmenburg (Behmenburg 1964) and Hindmarsh *et al.* (Hindmarsh *et al* 1967) have calculated the effects of inclusion of a repulsive term using a Lennard Jones 6-12 potential. This resulted in some improvement in that the width/shift ratio for a van der Waals broadened line could take on more accurate values. However, the interpretation of the collision-broadened spectral line was not entirely unambiguous and the inclusion of a new parameter C_{12}, associated with the $1/r^{12}$ repulsive term, led to problems associated with its evaluation. Dyne (Dyne 1971) used an exp(-λr) repulsive term with much the same results. Fullerton and Cowley (Fullerton and Cowley 1970) expanded the van der Waals potential and found significant enhancement of the broadening coefficients, decreasing the disparity between theory and experiment. Here are practical expressions for relatively accurate estimations.

<u>*Van der Waals potential*</u> *(*$V_6 = -C_6/r^6$*)*

The following van der Waals broadening expressions are valid only within the impact approximation. The line shape is Lorentzian and its width is solely a result of the strong collisions. Griem provides the following expression:

$$\Delta\omega_{vdw}^{1/2} = \pi\left(\frac{9\pi\eta^5\left|\left\langle \overline{R}_u^2\right\rangle - \left\langle \overline{R}_l^2\right\rangle\right|}{16m_e^3E_u^2}\right)^{2/5}\bar{v}^{3/5}N \tag{60}$$

where N is the number density of the gas. $\omega = 2\pi\nu$ is the angular frequency (in [rad s^{-1}]). E_u is the energy of the upper level. The mean square radius $\left\langle \overline{R}_j^2\right\rangle$ of the atom in its excited level j can be estimated by the hydrogenic approximation:

$$\left\langle \overline{R}_j^2\right\rangle = \frac{n_j^{*2}}{2}\left(5z^2n_j^{*2} + 1 - 3l(l+1)\right)a_0^2 \tag{61}$$

where l is the azimuthal quantum number. z is the effective number of charge (Griem 1964). n_j^{*2} is the effective principal quantum number given by:

$$n_j^{*2} = \frac{E_{ion}^H}{E_{ion} - E_j} \tag{62}$$

Eq.(61) can return negative values which are not acceptable. Then, another more accurate approximation must be used to evaluate $\left\langle \overline{R}_j^2\right\rangle$.

The thermal velocity is given by:

$$\bar{v} = \sqrt{\frac{8k_BT}{\pi\mu m_u}} \tag{63}$$

where μ is the reduced mass for the collision $\mu = \frac{M_{emit}M_{pert}}{M_{emit} + M_{pert}}$ and m_u the atomic mass unit.

By introducing the polarisability of the emitter, $\alpha = 4\pi\varepsilon_0\frac{a_0^2h^2}{\pi e^2m_e}\left(\frac{3}{4}\frac{E_{ion}^H}{E_u}\right)^2$, one finds:

$$\Delta\nu_{vdw} = \left(\frac{2\pi e^2}{4\pi\varepsilon_0 h}\alpha\left|\left\langle \overline{R}_u^2\right\rangle - \left\langle \overline{R}_l^2\right\rangle\right|a_0^2\right)^{2/5}\bar{v}^{3/5}N \tag{64}$$

as $C_6\left[J\cdot m^6\right]=\eta C_6^{'}\left[m^6\cdot s^{-1}\right]$[x] is the van der Waals dispersion coefficient, it reads:

$$\Delta\nu_{vdw}=\left|C_6^{'}\right|^{2/5}\bar{v}^{3/5}N \text{ [xi]} \tag{65}$$

with $C_6^{'}=\frac{2\pi e^2}{4\pi\varepsilon_0 h}\alpha\left|\left\langle\bar{R}_u^2\right\rangle-\left\langle\bar{R}_l^2\right\rangle\right|a_0^2$. C_6 can be estimated from the Lennard-Jones coefficients (ε_0,σ) with $C_6=4\varepsilon_0\sigma^6$.

Lines purely broadened by van der Waals interactions possess a $T^{0.3}$ dependence for $\Delta\nu_{vdw}$ and d_{vdw} (with the same unit as $\Delta\nu_{vdw}$), as predicted by Foley and Lindholm who also showed that:

$$d_{vdw}/\Delta\nu_{vdw}=-0.363 \tag{66}$$

The line is usually red-shifted (minus sign).

In the quasi-static approximation, the FWHM expressed in frequency is given by:

$$\Delta\nu_{vdw}^{qs}=\frac{1}{2\pi}\left|\hat{C}_6^{'}\right|\left(\frac{4\pi}{3}N\Gamma\left(\frac{1}{2}\right)\cos\left(\frac{3\pi}{12}\right)\right)^2=\frac{4\pi^2}{9}\left|\hat{C}_6^{'}\right|N^2 \tag{67}$$

Here, $\hat{C}_6^{'}$ can be slightly different from $C_6^{'}$, the difference could be associated with dependences on the angular momentum quantum numbers (Demura *et al.* 2011). The line profile is asymmetric and its form is taken according to Margenau (1935):

$$M(\nu)=\begin{cases}-\sqrt{\dfrac{\Delta\nu_{vdw}^{qs}}{(\nu-\nu_0)^3}}\exp\left(-\dfrac{\pi}{4}\dfrac{\Delta\nu_{vdw}^{qs}}{\nu-\nu_0}\right) & \text{if } \nu<\nu_0\\ 0 & \text{if } \nu\geq\nu_0\end{cases} \tag{68}$$

Example (Leo et al. 1992): The line He I ($1s3p\ ^3P_{0,1,2}$ - $1s2s\ ^3S_1$) at 388.865 nm is broadened by van der Waals collision with He (self-broadening). Triplet helium state cannot be self-broadened by resonance. Here, E_{ion}=3.940×10^{-18} J (24.5901 eV), E_l=3.176×10^{-18} J

[x] We also find $C_6\left[J\cdot m^6\right]=hC_6^{''}\left[rad\cdot m^6\cdot s^{-1}\right]$.

[xi] Sometimes, we find $\bar{\omega}\left[cm^{-1}\right]/N\left[cm^{-3}\right]=8.16\left|C_6\left[erg\cdot cm^6\right]\right|^{2/5}\left(\bar{v}\left[cm\cdot s^{-1}\right]\right)^{3/5}$ where γ is the FWHM. It gives exactly the same result as $\Delta\nu_{vdw}=\left|C_6^{'}\right|^{2/5}\bar{v}^{3/5}N$ [SI]).

(19.8218 eV) with l=0; E_{ion}^{H}=2.180×10^{-18} J (13.6057), E_u=3.687×10^{-18} J (23.0097 eV) with l=1. μ=2. At T=300 K and N=10^{24} m^{-3}. We get α=3.662×10^{-31} m^3. Eq.(61) gives $\left|\left\langle \overline{R}_u^2 \right\rangle - \left\langle \overline{R}_l^2 \right\rangle\right|$ =3.974×10^{-19} m^2 (142.00 a_0^2). Then, C_6=3.357×10^{-77} J·m^6 ($C_6^{'}$=3.184×10^{-43} m^6·s^{-1}), and finally $\Delta\nu_{vdw}$=8.948×10^8 Hz (*i.e.* $\Delta\lambda_{vdw}$=0.000451 nm). This gives $\Delta\nu_{vdw}/N_g$ =8.948×10^{-16} Hz m^3 to be compared to 1.57×10^{-15} Hz m^3 which is the value determined by Leo *et al.* (1992).

<u>*Lennard-Jones potential*</u> ($V_{12} = C_{12}/r^{12} - C_6/r^6$)

For Lennard-Jones potential, Hindmarsh *et al.* (1967) derived the following expression for the frequency broadening:

$$\Delta\nu_{lj} = 2N\bar{v}\int_0^\infty \rho(1-\cos\eta(\rho))d\rho \tag{69}$$

With the dimensionless quantity:

$$\eta(\rho) = \int_{-\infty}^{\infty} \frac{C_{12}^{'}}{r^{12}} - \frac{C_6^{'}}{r^6}\,dt = \frac{63\pi}{256}\frac{1}{\bar{v}}\frac{C_{12}^{'}}{\rho^{11}} - \frac{3\pi}{8}\frac{1}{\bar{v}}\frac{C_6^{'}}{\rho^5} \tag{70}$$

where ρ is the collision of impact parameter. Noting $x^{-5} = \frac{3\pi}{8}\frac{1}{\bar{v}}\frac{|C_6^{'}|}{\rho^5}$, one finds:

$$\eta(\rho) = \alpha x^{-11} - x^{-5} \tag{71}$$

With, in SI units, $\alpha = \frac{21}{32}\left(\frac{8}{3\pi}\right)^{6/5}\bar{v}^{6/5}\frac{C_{12}^{'}}{|C_6^{'}|^{11/5}} \approx 0.539\bar{v}^{6/5}\frac{C_{12}^{'}}{|C_6^{'}|^{11/5}}$ [xii]

Then, Eq.(69) reads:

$$\Delta\nu_{lj} = 4\left(\frac{3\pi}{8}\right)^{2/5}\bar{v}^{3/5}|C_6^{'}|^{2/5}B(\alpha)N \tag{72}$$

where $B(\alpha)$ is given by:

[xii] $C_6^{'}$ and $C_{12}^{'}$ can theoretically adopt negative values, but are most often positive.

$$B(\alpha)=\int_0^{\infty} x\sin^2\left(\frac{1}{2}\left(\frac{\alpha}{x^{11}}-\frac{1}{x^5}\right)\right)dx \tag{73}$$

The shift is given by:

$$d_{lj}=N\bar{v}\int_0^{\infty}\rho\sin\eta(\rho)d\rho \tag{74}$$

and, after calculation:

$$d_{lj}=\frac{\lambda^2}{2c}\Delta\nu_{lj}\frac{S(\alpha)}{2B(\alpha)} \tag{75}$$

with

$$S(\alpha)=\int_0^{\infty} x\sin\left(\frac{\alpha}{x^{11}}-\frac{1}{x^5}\right)dx \tag{76}$$

$B(\alpha)$ and $S(\alpha)$ are tabulated functions given as a function of α (Table 2).

Example (Hammond 1975): The Ca II H line at 396.847 nm is broadened by helium. At a concentration of 2.05×10^{27} m^{-3}, using $C_6 = 3.4\times10^{-78}$ J m^6 and $C_{12} = 2.1\times10^{-134}$ J m^{12}, one finds $\alpha = 1.58$, $B(\alpha) = 0.254$, $S(\alpha) = -0.114$, $\Delta\nu_{lj} = 1.57\times10^{12}$ s^{-1} ($\Delta\lambda_{lj} = 0.82$ nm) and $d_{lj} = -0.092$ nm.

2.6.2.3. Doppler broadening

Molecules in a gas possess a Maxwell velocity distribution. Hence the velocity components along any direction of observation produce a Doppler effect which induces a shift in frequency in the emitted radiance. The line profile is Gaussian and its FWHM is:

$$\Delta\nu_D=\nu_0\sqrt{\frac{8\ln 2\times RT}{Mc^2}} \tag{77}$$

where ν_0 is the frequency of the transition, T is the gas temperature and M is the molar weight (expressed in [kg·mol^{-1}]) of radiating atoms. The line shift due to the Doppler effect is usually negligible since $d_D=\frac{v}{c}\nu_0$ where v is the atom velocity.

Example: For the Hα line at 656.28 nm, taking M=0.001 kg·mol^{-1}, T=11604 K, $\Delta\nu_D$ = 3.524×10^{10} Hz (*i.e.* $\Delta\lambda_D = 0.0506$nm).

Doppler broadening can also stem from the flow of the gas itself, if it is very high (supersonic) along the line of sight:

$$\Delta\nu_D = \sqrt{\ln(2)}\left(\frac{v_{flow}}{c}\right)\frac{c}{\lambda_0} \tag{78}$$

2.6.2.4. Instrumental broadening

When we record a line emitted by a He-Ne laser at 632.8 nm, its width being about 1.3 pm, we usually observe a much broader line. This is due to the apparatus itself which introduces an instrumental broadening. The line shapes thus obtained with good spectrometers are approximately Gaussian (in fact, mostly the central part of the line).

2.7. Emission of continua and molecules

Several different mechanisms, which are listed hereafter, can lead to the emission of continua. In the following section, only optically thin media will be considered.

2.7.1. Planck's continuum

The emissivity $\varepsilon_P(\nu,T)$ expressed in [W·m^{-3}·sr^{-1}·Hz^{-1}] radiated by a plasma at a temperature T is related to the Planck law by the Kirchhoff law:

$$\varepsilon_P(\nu,T) = \kappa_P(\nu,T)B_\nu(T) \tag{79}$$

with :

$$B_\nu(T) = \frac{2h\nu^3}{c^2}\frac{1}{\exp\left(\frac{h\nu}{k_BT}\right)-1} \tag{80}$$

in [W·m^{-2}·sr^{-1}·Hz^{-1}]. The Planck continuum is composed of a large number of individual emission lines which can be broadened and shifted. Considering only one of these lines, we

can express the corresponding absorption coefficient which is linked to the cross sections for absorption and stimulated emission by:

$$\kappa_P^{u\to l}(T) = N_l\sigma_{ul} - N_u\sigma_{lu} \tag{81}$$

In terms of Einstein's coefficients, it reads:

$$\kappa_P^{u\to l}(T) = \frac{h\nu}{c}\phi(\nu)\left(N_l B_{lu} - N_u B_{ul}\right) \tag{82}$$

where $\phi(\nu)\cong 1/\Delta\nu$ is the normalized shape of the spectral line (in [s]). B_{lu} is the Einstein absorption coefficient and B_{ul} is the stimulated emission coefficient (both terms in $[m^3\cdot J^{-1}\cdot s^{-2}]$). If the densities are distributed according to a Boltzmann law, one finds:

$$\kappa_P^{u\to l}(T) = \frac{h\nu}{c}\phi(\nu)\frac{g_l}{Q_0}B_{lu}N\exp\left(-\frac{E_l}{k_B T}\right)\left[1-\exp\left(-\frac{h\nu}{k_B T}\right)\right] \tag{83}$$

as $g_l B_{lu} = g_u B_{ul}$. Q_0 is the partition function of the considered species of density N and g_l the statistical weight of the lower level. The estimation of $\kappa_P(\nu,T)$ from $\kappa_P^{u\to l}(T)$ is usually complex since it requires a large set of basic data (energy levels of transitions, Einstein's coefficients, statistical weights, etc.)

2.7.2. Continuum emission from electron-ion recombination

The emission intensity for the electron–ion recombination (free–bound transitions) and for the bremsstrahlung (free–free transitions) of hydrogenic ions can be treated as a whole. It must be treated from scratch to make understandable the restrictions that apply to the main formulas.

Let's start by considering the following recombination process:

$$X^{i+} + e \to X_p^{(i-1)+} + h\nu \tag{a}$$

The reverse process is photoionization:

$$X_p^{(i-1)+} + h\nu \to X^{i+} + e \tag{−a}$$

i is the ion charge and *p* is the excited level of the *hydrogenic* species $X^{(i-1)+}$ whose atomic number is *Z*. Process (a) emits a photon with the energy:

$$h\nu = \frac{1}{2}m_e v_e^2 + \left(E_1^i - E_p^{i-1}\right) = \frac{1}{2}m_e v_e^2 + \left(Z^2 Ry - \frac{Z^2 Ry}{p^2}\right) \tag{84}$$

Here, E_1^i and E_p^{i-1} are the ionization energy of $X^{(i-1)+}$ and the energy of level *p* respectively. *Ry* is the Rydberg constant: $Ry = \frac{2\pi^2 e^4 m_e}{(4\pi\varepsilon_0)^2 h^2}$.

The cross section of the photoionization process (–a) is given by:

$$\sigma_{p\nu} = \frac{2^6\pi}{3\sqrt{3}}\underbrace{\left(\frac{e^2}{4\pi\varepsilon_0 \eta c}\right)}_{\alpha}\underbrace{\left(\frac{2\pi^2 m_e e^4}{(4\pi\varepsilon_0)^2 h^2}\frac{1}{h}\right)^3}_{\nu_c}\underbrace{\left(\frac{\eta^2 4\pi\varepsilon_0}{m_e e^2}\right)^2}_{a_0}\frac{Z^4}{\nu^3}\frac{g_{fb}}{p^5} \tag{85}$$

where α is the fine structure constant, a_0 is the Bohr radius and $\nu_c = Ry/h$ is a critical frequency equal to 3.290×10^{15} Hz (*i.e.* λ_c = 91 nm). g_{fb} is the free–bound Gaunt factor, the other terms having their usual meaning. g_{fb} accounts for the misfit between quantum and classical predictions. It depends on each considered level.

The cross section of the direct collision (process (a)) is given by the Milne relation:

$$\sigma_{\nu p} = \frac{g_{i-1}(p)}{g_i}\left(\frac{h\nu}{m_e v_e c}\right)^2 \sigma_{p\nu} = \frac{2p^2}{g_i}\left(\frac{h\nu}{m_e v_e c}\right)^2 \sigma_{p\nu}$$ [xiii] (86)

and finally:

$$\sigma_{\nu p} = \frac{1}{(4\pi\varepsilon_0)^5}\frac{2^7\pi^4 e^{10}}{3\sqrt{3}\times m_e c^3 h^4}\frac{Z^4}{\nu}\frac{g_{fb}}{p^3 v_e^2} \tag{87}$$

v_e is the electron velocity. The emissivity of level *p*, $\varepsilon_p(\nu, T_e)$ expressed in [W·sr^{-1}·m^{-3}·Hz^{-1}], due to the recombination process is given by:

$$\varepsilon_{R,p}^{ei}(\nu, T_e)d\Omega d\nu = \frac{d\Omega d\nu}{4\pi}\int_0^\infty h\nu N_e N_i f(v_e) v_e \sigma_{vp} dv_e \tag{88}$$

N_e and N_i are the electron and ion (here of X^{i+}) densities respectively. $f(v_e)$ is the electron velocity distribution function. Assuming a Maxwellian distribution, *i.e.*

[xiii] For hydrogenic ions, g_i=1 and this term disappears at this stage.

$f(v_e) = 4\pi\left(\frac{m_e}{2\pi k_B T_e}\right)^{3/2} \exp\left(-\frac{1}{2}\frac{m_e v_e^2}{k_B T_e}\right) v_e^2$ in [s·m^{-1}] and using $\frac{1}{2}m_e v_e^2 = h\nu - \frac{Z^2 Ry}{p^2}$, one finds:

$$\varepsilon_{R,p}^{ei}(\nu, T_e) d\nu d\Omega = \frac{1}{(4\pi\varepsilon_0)^2} \frac{16 e^4 h}{3 m_e^2 c^3 \sqrt{3\pi}} \left(\frac{Ry}{k_B T_e}\right)^{3/2} N_e N_i \frac{Z^4}{p^3} \bar{g}_{fb} \exp\left(-\frac{h\nu}{k_B T_e}\right) \exp\left(\frac{Z^2 Ry}{p^2 k_B T_e}\right) d\nu d\Omega \quad (89)$$

$\bar{g}_{fb}(\nu, T_e)$ is called the thermally averaged free–bound Gaunt factor because it is averaged over a Maxwellian electron velocity distribution function. Most often, it is close to 1 but accurate tabulated values are available in (Karzas and Latter 1961)

To access the total emission, the summation over all the permitted quantum levels, *i.e.* those that verify the condition: $h\nu = \frac{1}{2}m_e v_e^2 + \frac{Z^2 Ry}{p^2} \geq \frac{Z^2 Ry}{p^2}$, must be done.

$$\varepsilon_R^{ei}(\nu, T_e) = \sum_{p \geq \sqrt{\frac{Z^2 Ry}{h\nu}}}^{\infty} \varepsilon_{R,p}^{ei}(\nu, T_e) \quad (90)$$

Because of the narrowing of the higher levels, it is possible to define the threshold p^* so that at large values of p, the summation over p can be replaced by an integral (Unsöld 1938).

$$\varepsilon_R^{ei}(\nu, T_e) = \sum_{p \geq \sqrt{\frac{Z^2 Ry}{h\nu}}}^{p^*} \varepsilon_{R,p}^{ei}(\nu, T_e) + \sum_{p^*+1}^{\infty} \varepsilon_{R,p}^{ei}(\nu, T_e) \quad (91)$$

with:

$$\sum_{p^*+1}^{\infty} \frac{1}{p^3} \exp\left(\frac{Z^2 Ry}{p^2 k_B T_e}\right) = -\frac{1}{2} \int_{1/(p^*+1)^2}^{0} \exp\left(\frac{Z^2 Ry}{p^2 k_B T_e}\right) d\left(\frac{1}{p^2}\right) \quad (92)$$

Then:

$$\sum_{p^*+1}^{\infty} \varepsilon_{R,p}^{ei}(\nu, T_e) d\nu d\Omega = -\frac{1}{(4\pi\varepsilon_0)^2} \frac{8 e^4 h}{3 m_e^2 c^3 \sqrt{3\pi}} \left(\frac{Ry}{k_B T_e}\right)^{3/2} N_e N_i Z^4 \bar{g}_{fb} \exp\left(-\frac{h\nu}{k_B T_e}\right) \int_{1/(p^*+1)^2}^{0} \exp\left(\frac{Z^2 Ry}{p^2 k_B T_e}\right) d\left(\frac{1}{p^2}\right) d\nu d\Omega \quad (93)$$

The value of p^* can be evaluated by resorting for example to the Inglis–Teller limit for singly charged perturbers:

$$\log p^* \approx 3.21 - 0.143 \log n_e \left[cm^{-3}\right] \tag{94}$$

2.7.3. Continuum emission from electron-ion bremsstrahlung

To include bremsstrahlung, Unsold (1955) extended the above range of integration, assuming that the "binding" energy of free electrons is negative and has no bounds. The recombination into free states is then given by:

$$\sum_{p^*+1}^{\infty} \varepsilon_{B,p}^{ei}(\nu, T_e) d\nu d\Omega = -\frac{1}{(4\pi\varepsilon_0)^2}\left(\frac{Ry}{k_B T_e}\right)^{3/2} \frac{8e^4 h}{3m_e^2 c^3 \sqrt{3\pi}} N_e N_i Z^4 \bar{g}_{ff} \exp\left(-\frac{h\nu}{k_B T_e}\right) \int_{-\infty}^{0} \exp\left(\frac{Z^2 Ry}{p^2 k_B T_e}\right) d\left(\frac{1}{p^2}\right) d\nu d\Omega \tag{95}$$

where $\bar{g}_{ff}(\nu, T_e)$, which replaces $\bar{g}_{fb}(\nu, T_e)$, is now the thermally averaged free–free Gaunt factor. Integration is readily made:

$$\varepsilon_B^{ei}(\nu, T_e) d\nu d\Omega = \frac{1}{(4\pi\varepsilon_0)^2} \frac{8e^4 h}{3m_e^2 c^3 \sqrt{3\pi}} \frac{Ry^{1/2}}{(k_B T_e)^{1/2}} Z^2 N_e N_i \exp\left(-\frac{h\nu}{k_B T_e}\right) \bar{g}_{ff} d\nu d\Omega \tag{96}$$

The following equivalent expression is more commonly found today:

$$\varepsilon_B^{ei}(\nu, T_e) d\nu d\Omega = \frac{16\pi e^6}{3c^3 (4\pi\varepsilon_0)^3 \sqrt{6\pi k_B m_e^3}} \frac{N_e(x) N_i(x, T_e)}{\sqrt{T_e}} Z^2 \bar{g}_{ff}(\nu, T_e) \exp\left(-\frac{h\nu}{k_B T_e}\right) d\nu d\Omega \tag{97}$$

The radiated power per unit volume (in [W·m^{-3}]) is obtained from an integral over the frequency spectrum and over 4π sr:

$$P_B^{ei}(T_e) = \int_0^{4\pi} \int_0^{\infty} \varepsilon_B^{ei}(\nu, T_e) d\nu d\Omega \tag{98}$$

One finds:

$$P_B^{ei}(T_e) = \frac{64 k_B \pi^2 e^6}{3c^3 (4\pi\varepsilon_0)^3 h \sqrt{6\pi k_B m_e^3}} N_e(x) N_i(x, T_e) Z^2 \bar{\bar{g}}_{ff}(T_e) \sqrt{T_e} \tag{99}$$

where $\bar{\bar{g}}_{ff}(\nu, T_e)$ is the total free–free Gaunt factor, *i.e.* integrated over the frequency range. with $\frac{64\pi^2 e^6}{3c^3 (4\pi\varepsilon_0)^3 h \sqrt{6\pi k_B m_e^3}} = 1.429 \times 10^{-40}$ J m^3·K$^{-1/2}$. Tabulated values are given by van Hoof *et al.* (2014).

2.7.4. Electron-ion recombination: Schlüter's approach

Thanks to computers, there is no need today to separate the summation in two terms. This method is rather convenient to explain how Bremsstrahlung was introduced. Then, the emissivity due to electron–ion (free–bound) recombination simply reads:

$$\varepsilon_R^{ei}(\nu,T_e)=\frac{64\pi^3e^{10}}{3h^2c^3\sqrt{6m_e\pi}}\frac{1}{(4\pi\varepsilon_0)^5}\frac{Z^4}{(k_BT_e)^{3/2}}N_eN_i\exp\left(-\frac{h\nu}{k_BT_e}\right)\sum_{\sqrt{\frac{Z^2Ry}{h\nu}}}^{\infty}\frac{\bar{g}_{fb}}{p^3}\exp\left(\frac{Z^2Ry}{p^2k_BT_e}\right) \quad (100)$$

This contribution is plotted in Figure 8.

The radiated power per unit volume (in [W·m^{-3}]) is obtained from an integral over the spectrum, and one finds:

$$P_R^{ei}(T_e)=\frac{256\pi^4e^{10}}{3h^3c^3\sqrt{6m_e\pi}}\frac{1}{(4\pi\varepsilon_0)^5}\frac{Z^4}{(k_BT_e)^{1/2}}N_eN_i\sum_{\sqrt{\frac{Z^2Ry}{h\nu}}}^{\infty}\frac{\bar{\bar{g}}_{fb}}{p^3}\exp\left(\frac{Z^2Ry}{p^2k_BT_e}\right) \quad (101)$$

where $\bar{\bar{g}}_{fb}(\nu,T_e)$ is the total free–bound Gaunt factor, *i.e.* integrated over the frequency range.

Schlüter (1968) proposes another approach to evaluate free-bound recombination. He starts directly from the photoionization process (–a) and calculates the absorbance instead of the emission of the plasma, both contributions being linked by the Kirchhoff law. Then, he relates the corresponding cross section (Eq.85) to the emissivity by:

$$\varepsilon_R^{ei}(\nu,T_e)=\left(\sum_{p^*}^{\infty}\sigma_{p\nu}N_p\right)B_\nu(T_e)\left\{1-\exp\left(-\frac{h\nu}{k_BT_e}\right)\right\} \quad (102)$$

where the term in curly brackets accounts for the induced emission. $B_\nu(T_e)$ in [W·m^{-2}·sr^{-1}·Hz^{-1}] is the Kirchhoff–Planck function:

$$B_\nu(T_e)=\frac{2h\nu^3}{c^2}\frac{1}{\exp\left(\frac{h\nu}{k_BT_e}\right)-1} \quad (103)$$

The sum starts only at level p^* defined by $p^*=\sqrt{\frac{Z^2Ry}{h\nu}}$, otherwise the photon energy would be too low to produce level *p*. The absorption coefficient in [m^{-1}],

$$\kappa_R^{ei}(\nu,T_e)=\sum_{p^*}^{\infty}\sigma_{p\nu}N_p=\sum_{p^*}^{\infty}\left(\frac{2^6\pi^4e^{10}m_e}{3\sqrt{3}\times ch^6}\frac{1}{(4\pi\varepsilon_0)^5}\frac{Z^4}{\nu^3}\frac{\bar{g}_{fb}}{p^5}\right)N_p \tag{104}$$

if a Boltzmann distribution is considered,

$$N_p=\frac{g_p}{Q_{i-1}}\exp\left(-\frac{E_p}{k_BT_e}\right)N_{i-1} \tag{105}$$

reads:

$$\sum_{p^*}^{\infty}\sigma_{p\nu}N_p=\sum_{p^*}^{\infty}\left(\frac{2^6\pi^4e^{10}m_e}{3\sqrt{3}\times ch^6}\frac{1}{(4\pi\varepsilon_0)^5}\frac{Z^4}{\nu^3}\frac{\bar{g}_{fb}}{p^5}\right)\frac{g_p}{Q_{i-1}}\exp\left(\frac{Z^2Ry}{k_BT_e}\left(\frac{1}{p^2}-1\right)\right)N_{i-1} \tag{106}$$

Using Eq.(92) and $g_p=2p^2$, one finds:

$$\kappa_R^{ei}(\nu,T_e)=-\left(\frac{2^6\pi^4e^{10}m_e}{3\sqrt{3}\times ch^6}\frac{1}{(4\pi\varepsilon_0)^5}\frac{Z^4}{\nu^3}\bar{g}_{fb}\frac{N_{i-1}}{Q_{i-1}}\right)\int_{(1/p^*)^2}^{0}\exp\left(\frac{Z^2Ry}{k_BT_e}\left(\frac{1}{p^2}-1\right)\right)d\left(\frac{1}{p^2}\right) \tag{107}$$

and thus:

$$\kappa_R^{ei}(\nu,T_e)=\left(\frac{2^5\pi^2e^6}{3\sqrt{3}\times ch^4}\frac{k_B}{(4\pi\varepsilon_0)^3}\frac{Z^2}{\nu^3}\bar{g}_{fb}\frac{N_{i-1}}{Q_{i-1}}\right)T_e\left[\exp\left(\frac{h\nu}{k_BT_e}\right)-1\right]\exp\left(-\frac{Z^2Ry}{k_BT_e}\right) \tag{108}$$

At this stage, Schlüter does not need assume **L.T.E**. We do so here to compare the emissivity deduced from Eq.(108) with Eq.(100).[xiv] Indeed, both expressions must give strickly identical results, at least for hydrogenic ions and in LTE conditions. Then, using Saha's equation:

$$\frac{N_eN_i}{N_{i-1}}=\frac{2Q_i}{Q_{i-1}}\frac{(2\pi m_ek_BT_e)^{3/2}}{h^3}\exp\left(-\frac{Z^2Ry}{k_BT_e}\right) \tag{109}$$

one finds:

$$\kappa_R^{ei}(\nu,T_e)=\left(\frac{2^4\pi e^6}{3\sqrt{6\pi k_Bm_e^3}\times ch}\frac{1}{(4\pi\varepsilon_0)^3}\frac{Z^2}{\nu^3}\bar{g}_{fb}\frac{N_eN_i}{Q_{i-1}}\right)\frac{1}{\sqrt{T_e}}\frac{Q_{i-1}}{2Q_i}\left[\exp\left(\frac{h\nu}{k_BT_e}\right)-1\right] \tag{110}$$

Then, with Eq. (102):

[xiv] The calculation including the **L.T.E.** assumption was made by Schulz-Gulde (1970)

$$\varepsilon_R^{ei}(\nu,T_e)=\left(\frac{2^5\pi e^6}{3c^3\sqrt{6\pi k_B m_e^3}}\frac{Z^2}{(4\pi\varepsilon_0)^3}\bar{g}_{fb}\frac{N_e N_i}{Q_{i-1}}\right)\frac{1}{\sqrt{T_e}}\frac{Q_{i-1}}{2Q_i}\left[1-\exp\left(-\frac{h\nu}{k_B T_e}\right)\right] \quad (111)$$

and finally:

$$\varepsilon_R^{ei}(\nu,T_e)=\left(\frac{2^4\pi e^6}{3c^3\sqrt{6\pi k_B m_e^3}}\frac{Z^2}{(4\pi\varepsilon_0)^3}\right)\frac{N_e N_i}{\sqrt{T_e}}\frac{1}{Q_i}\bar{g}_{fb}\left[1-\exp\left(-\frac{h\nu}{k_B T_e}\right)\right] \quad (112)$$

This equation cannot be used *as such*. When it is compared with equation (100), we notice from Figure 8 that the saw-teeth shape of expression (100) caused by the quantified energy levels (the absorption edges) is replaced by a smooth behaviour. Schlüter introduces the so-called Biberman-Schlüter function $\xi_{fb}(\nu,T_e)$[xv] to make his expression match Eq.(100) (Ansatz). He gives the following expression:

$$\xi_{fb}(\nu,T_e)=\frac{Z^2 Ry}{k_B T_e}\exp\left(\frac{Z^2 Ry}{k_B T_e}\right)\left[\exp\left(\frac{h\nu}{k_B T_e}\right)-1\right]^{-1}\sum_{p=\sqrt{\frac{Z^2 Ry}{h\nu}}}^{\infty} g_p\frac{\bar{g}_{fb}}{p^5}\exp\left(-\frac{E_p}{k_B T_e}\right)\text{xvi} \quad (113)$$

where γ accounts for the non-hydrogenic behavior of the atom. The Gaunt factor is removed from Eq.(112) to be included in $\xi(\nu,T_e)$.

$$\kappa_R^{ei}(\nu,T_e)=\left(\frac{2^5\pi e^6}{3\sqrt{6\pi k_B m_e^3}\times ch}\frac{1}{(4\pi\varepsilon_0)^3}\frac{Z^2}{\nu^3}\right)\frac{N_e N_i}{\sqrt{T_e}}\left[\exp\left(\frac{h\nu}{k_B T_e}\right)-1\right]\frac{\gamma}{Q_i}\xi_{fb}(\nu,T_e) \quad (114)$$

Since $g_p=2p^2$ and $E_p=Z^2 Ry\left(1-1/p^2\right)$, it reads:

$$\kappa_R^{ei}(\nu,T_e)=\left(\frac{2^6\pi e^6}{3\sqrt{6\pi k_B m_e^3}\times ch}\frac{1}{(4\pi\varepsilon_0)^3}\frac{Z^4}{\nu^3}\frac{N_e N_i}{\sqrt{T_e}}\right)\frac{Ry}{k_B T_e}\frac{\gamma}{Q_i}\sum_{p=\sqrt{\frac{Z^2 Ry}{h\nu}}}^{\infty}\frac{\bar{g}_{fb}}{p^3}\exp\left(\frac{Z^2 Ry}{p^2 k_B T_e}\right) \quad (115)$$

and then:

$$\varepsilon_R^{ei}(\nu,T_e)=\left(\frac{2^6\pi^3 e^{10}}{3h^2c^3\sqrt{6\pi m_e}}\frac{1}{(4\pi\varepsilon_0)^5}\right)\frac{Z^4}{(k_B T_e)^{3/2}}N_e N_i\frac{\gamma}{Q_i}\exp\left(-\frac{h\nu}{k_B T_e}\right)\sum_{\sqrt{\frac{Z^2 Ry}{h\nu}}}^{\infty}\frac{\bar{g}_{fb}}{p^3}\exp\left(\frac{Z^2 Ry}{p^2 k_B T_e}\right) \quad (116)$$

[xv] $\xi_{fb}(\nu,T_e)$ is sometimes confused with the Gaunt factor.
[xvi] Z^2 is missing in the original expression by Schülter.

which is exactly Eq.(100) if we set $\gamma = Q_i$, *i.e.* the parent ion partition function, for the hydrogenic case. The main interest of Schlüter's approach is to get rid of the atomic data needed to evaluate $\xi_{fb}(\nu,T_e)$. These data are not always known. Then, the Biberman-Schlüter function is determined experimentally and includes not only the discrete variations observed in the spectra due to quantified energy levels but also the non-hydrogenic behavior of the studied atom thanks to the factor γ. Using $\xi(\nu,T_e)$ as an input data (Meiners and Weiss 1976, Manola *et al.* 1991), bound-free emission can be readily determined by:

$$\varepsilon_R^{ei}(\nu,T_e) = \left(\frac{16\pi e^6}{3c^3(4\pi\varepsilon_0)^3\sqrt{6\pi k_B m_e^3}}\right)\frac{N_e N_i}{\sqrt{T_e}} Z^2 \frac{\gamma}{Q_i}\xi_{fb}(\nu,T_e)\left[1-\exp\left(-\frac{h\nu}{k_B T_e}\right)\right] \qquad (117)$$

Emission by electron-ion interactions (free-free from Eq.(97) and free-bound) is then:

$$\varepsilon_R^{ei} + \varepsilon_B^{ei} \approx 5.444\times10^{-52}\frac{N_e N_i}{\sqrt{T_e}} Z^2\left\{\xi_{ff}\exp\left(-\frac{h\nu}{k_B T_e}\right)+\frac{\gamma\xi_{fb}}{Q_i}\left[1-\exp\left(-\frac{h\nu}{k_B T_e}\right)\right]\right\} \qquad (118)$$

In this expression, the Gaunt factor for free-free interaction $\bar{g}_{ff}$ is replaced by the Biberman-Schlüter function ξ_{ff} to include non-hydrogenic atoms. In figure 9, examples of ξ_{fb} functions are given.

2.7.5. Continuum emission from electron-neutral bremsstrahlung

Let us consider the following deceleration process of an electron with the energy $\varepsilon = \frac{1}{2}m_e v_e^2$:

$$X + e(\varepsilon) \rightarrow X + e(\varepsilon - h\nu) + h\nu \qquad (b)$$

The differential cross section $\frac{d\sigma_{oe}(\nu)}{d\nu}$ [m^2·s] for this emission process is:

$$\frac{d\sigma_{oe}(\nu)}{d\nu} = \frac{8\pi e^2}{3\eta^3 c^3}\frac{m_e^2}{4\pi\varepsilon_0}\nu^3\frac{k_f}{k_i}|M|^2 \qquad (119)$$

$|M|^2$ is the matrix element expressed here in [m^8].

$$|M|^2 = \frac{64\pi^2}{\left(k_i^2 - k_f^2\right)^4}\left[k_i^2\sigma^m(\varepsilon - h\nu) + k_f^2\sigma^m(\varepsilon)\right] \tag{120}$$

with $k_f^2 = \frac{2m_e}{\eta^2}(\varepsilon - h\nu)$ and $k_i^2 = \frac{2m_e}{\eta^2}\varepsilon$ where k_i and k_f are in [m $^{-1}$]. One finds easily:

$$|M|^2 = \frac{8\pi^2\eta^6}{m_e^3(h\nu)^4}\varepsilon\left[\sigma^m(\varepsilon - h\nu) + \left(1 - \frac{h\nu}{\varepsilon}\right)\sigma^m(\varepsilon)\right] \tag{121}$$

As $\frac{k_f(\varepsilon - h\nu)}{k_i(\varepsilon)} = \left(1 - \frac{h\nu}{\varepsilon}\right)^{1/2}$, equation (119) reads:

$$\frac{d\sigma_{oe}(\nu)}{d\nu} = \frac{1}{4\pi\varepsilon_0}\frac{8e^2}{3c^3m_e}\left(\frac{\varepsilon}{h\nu}\right)\left(1 - \frac{h\nu}{\varepsilon}\right)^{1/2}\left[\sigma^m(\varepsilon - h\nu) + \left(1 - \frac{h\nu}{\varepsilon}\right)\sigma^m(\varepsilon)\right]^2 \tag{122}$$

$\frac{1}{4\pi\varepsilon_0}\frac{8e^2}{3c^3m_e} \approx 2.507\times10^{-23}$ s.

The cross section $\sigma_{eo}(\nu)$ in (m^2·m^3) for the reverse process (–b):

$$X + e(\varepsilon) + h\nu \rightarrow X + e(\varepsilon + h\nu) \tag{–b}$$

is obtained by detailed balance:

$$\sigma_{eo}(k_f) = \frac{\eta}{8\pi m_e}\frac{k_i^2}{k_f}\frac{c^2}{\nu^2}\frac{d\sigma_{oe}(k_i)}{d\nu} \tag{123}$$

and then,

$$|M|^2 = \frac{8\pi^2\eta^6}{m_e^3(h\nu)^4}\left[(\varepsilon + h\nu)\sigma^m(\varepsilon) + \varepsilon\sigma^m(\varepsilon + h\nu)\right] \tag{124}$$

With $k_i(\varepsilon + h\nu) = \sqrt{\frac{2m_e(\varepsilon + h\nu)}{\eta^2}}$. Thus:

$$\sigma_{eo}(k_i) = \frac{\eta}{8\pi m_e}\frac{c^2}{\nu^2}\frac{8\pi e^2}{3\eta^3c^3}\frac{m_e^2}{4\pi\varepsilon_0}\nu^3\frac{8\pi^2\eta^6}{m_e^3(h\nu)^4}\sqrt{\frac{2m_e}{\eta^2}}\varepsilon^{3/2}\left(1 + \frac{h\nu}{\varepsilon}\right)^{1/2}\left[\left(1 + \frac{h\nu}{\varepsilon}\right)\sigma^m(\varepsilon) + \sigma^m(\varepsilon + h\nu)\right] \tag{125}$$

After simple algebra, one finds:

$$\sigma_{eo}(k_i) = \frac{\sqrt{2}}{m_e^{3/2}}\frac{e^2h^2}{3\pi c}\frac{1}{4\pi\varepsilon_0}\frac{1}{\varepsilon^{3/2}}\left(\frac{\varepsilon}{h\nu}\right)^3\left(1 + \frac{h\nu}{\varepsilon}\right)^{1/2}\left[\left(1 + \frac{h\nu}{\varepsilon}\right)\sigma^m(\varepsilon) + \sigma^m(\varepsilon + h\nu)\right] \tag{126}$$

with $\frac{\sqrt{2}}{m_e^{3/2}}\frac{e^2h^2}{3\pi c}\frac{1}{4\pi\varepsilon_0}\approx 5.831\times10^{-59}$ [xvii]

The absorption coefficient (in [m^{-1}]) is given by:

$$\kappa^{eo}(\nu,T_e)d\Omega d\nu=\frac{d\Omega d\nu}{4\pi}\int_0^\infty N_eN_a f(v_e)\sigma_{eo}dv_e \tag{127}$$

So, if *f* is Maxwellian:

$$\begin{aligned}\kappa^{eo}(\nu,T_e)d\Omega d\nu&=\frac{d\Omega d\nu}{4\pi\varepsilon_0}\frac{N_eN_a}{(k_BT_e)^{3/2}}\frac{1}{\sqrt{2}m_e^{3/2}}\frac{e^2h^2}{3\pi^{5/2}c}\\&\int_0^\infty\frac{1}{\varepsilon}\left(\frac{\varepsilon}{h\nu}\right)^3\exp\left(-\frac{\varepsilon}{k_BT_e}\right)\left(1+\frac{h\nu}{\varepsilon}\right)^{1/2}\left[\left(1+\frac{h\nu}{\varepsilon}\right)\sigma^m(\varepsilon)+\sigma^m(\varepsilon+h\nu)\right]d\varepsilon\end{aligned} \tag{128}$$

[xviii]

with $\frac{1}{4\pi\varepsilon_0}\frac{1}{k_B^{3/2}}\frac{1}{\sqrt{2}m_e^{3/2}}\frac{e^2h^2}{3\pi^{5/2}c}=1.021\times10^{-25}$.

This expression matches exactly Lawler's (Lawler 2004) if it is integrated over 4π sr. The emissivity is obtained with the Kirchhoff law (Eq. 102) where the induced emission is introduced. Finally, the emissivity reads:

$$\begin{aligned}\varepsilon^{eo}(\nu,T_e)d\nu&=\frac{\sqrt{2}}{3\pi}\frac{N_eN_a}{(\pi m_ek_BT_e)^{3/2}}\frac{e^2h^3}{\varepsilon_0}\frac{\nu^3}{c^3}\exp\left(-\frac{h\nu}{k_BT_e}\right)d\nu\\&\int_0^\infty\frac{1}{\varepsilon}\left(\frac{\varepsilon}{h\nu}\right)^3\exp\left(-\frac{\varepsilon}{k_BT_e}\right)\left(1+\frac{h\nu}{\varepsilon}\right)^{1/2}\left[\left(1+\frac{h\nu}{\varepsilon}\right)\sigma^m(\varepsilon)+\sigma^m(\varepsilon+h\nu)\right]d\varepsilon\end{aligned} \tag{129}$$

2.7.6. Emission of continua by molecules

Continuum emission of molecules with three or more atoms can arise not only from the previous free-free or free-bound mechanisms, but also from thermal heating and

[xvii] The coefficient $\frac{\sqrt{2}}{m_e^{3/2}}\frac{e^2h^2}{3\pi c}\frac{1}{4\pi\varepsilon_0}\approx 5.831\times10^{-59}$ is related to the value 1.844×10^{-42} of Dalgarno and Lane's (1966) work by converting energies from [erg] into [J], *i.e.* $\left(1\times10^{-7}\right)^{3/2}$ and cross sections from [cm] to [m].

[xviii] In the paper by Dalgano and Lane (1966), this expression is divided by the electron pressure $P_e=N_ek_BT_e$ and integrated over 4π sr.

chemiluminescence process. The most studied example is probably NO_2 because of its importance in air chemistry. Thermal heating:

$$NO_2 + M \rightarrow NO_2^* + M \qquad \text{(f)}$$

(between 972 and 1335 K after Paulsen *et al.* 1970) or chemiluminescence reactions, like *e.g.*:

$$NO + O + M \rightarrow NO_2^* + M \qquad \text{(g)}$$

can excite NO_2 molecules that emit so many transition lines that their overlapping create a continuum emission (Paulsen *et al.* 1970). Because of the extreme complexity of the NO_2 absorption spectrum (see Figure 10), the excited states of NO_2 are not well characterized, although significant advances have been made both experimentally (*e.g.* Butler *et al.* 1975) and theoretically (*e.g.* Gillispie *et al.* 1974). Similar emissions by SO_2 molecules from O + SO, CO_2 from CO + O or HNO from H and NO are observed in afterglow (Gold and Trush 1975). The maximum of the continuum depends highly on the excitation mechanism. For instance, HNO emission differs if it created by H+NO+M instead of O+NO+CH_3CHO (Ishiwata *et al.* 1973).

2.8. Radiative transfer

2.8.1. Optically thin media

When the plasma is optically thin, the emission coefficients and the observed intensities are proportional. However, once some radiation is absorbed, radiative transfer has to be considered.

The equation of radiative transfer can be written as:

$$\frac{1}{\kappa(\nu, x)} \frac{dI(\nu, x)}{dx} = -I(\nu, x) + \frac{\varepsilon(\nu, x)}{\kappa(\nu, x)} \qquad (130)$$

where $I(\nu,x)$ is the intensity of radiation at frequency ν along the line of sight (Ox) at point x [W sr^{-1} m^{-2} Hz^{-1}], $\kappa(\nu,x)$ is the absorption coefficient (in [m^{-1}]) and $\varepsilon(\nu,x)$ the spectral emission coefficient (*i.e.* the power radiated at point x per unit solid angle, volume and

frequency in [W sr^{-1} m^{-3} Hz^{-1}]). $S(x) = \varepsilon(\nu,x)/\kappa(\nu,x)$ is called as the source function. The optical depth τ is dimensionless quantity defined by:

$$d\tau = -\kappa(\nu, x)dx \tag{131}$$

so that equation (130) can be rewritten as:

$$\frac{dI(\nu, x)}{d\tau} = I(\nu, x) - S(x) \tag{132}$$

This is the differential radiative transfer equation (RTE). Integrating equation (132) over x gives the radiant flux density at the far field:

$$I(\nu) = \frac{\int_{-\infty}^{+\infty} \exp\left[\int_{-\infty}^{+\infty} \kappa(\nu, x)dx\right] \varepsilon(\nu, x)dx}{\exp\left[\int_{-\infty}^{+\infty} \kappa(\nu, x)dx\right]} \tag{133}$$

Estimating $I(\nu)$ requires to have $\varepsilon(\nu,x)$ and $\kappa(\nu,x)$ as a function of x. Using the Einstein coefficients, A_{ul} (emission), B_{ul} (induced emission) and B_{lu} (absorption), one has:

$$\kappa(\nu, x) = \frac{h\nu}{c}\left[B_{lu}N_l(x) - B_{ul}N_u(x)\right]S(x, \nu) \tag{134}$$

$$\varepsilon(\nu, x) = \frac{h\nu}{4\pi}A_{ul}N_u(x)S(x, \nu) \tag{135}$$

$N_l(x)$ and $N_u(x)$ are the population densities of the lower and upper levels, respectively. h is the Planck constant, c the light velocity. The function $S(x, \nu)$ gives the spectral distribution of the $u \to l$ transition for a given x. It is a function of both quantities ν and x and it is normalized in frequency: $\int_{-\infty}^{+\infty} S(x, \nu)d\nu = 1$. From there on, spatial distributions of emitting and absorbing levels, but also of all the other parameters that affect line broadening (T_g, T_e and N_e) must be provided.

2.8.2. Abel inversion

These parameters are often determined by probing the emitting volume linearly if it is optically thin. This volume is usually axially symmetric and thanks to this, getting the radial distribution of species is a quite easy task.

The reconstruction of a circularly symmetric two-dimensional function from its projection onto an axis is known as Abel inversion or inverse Abel transformation of the projection. The measured intensity, $I(x)$ where x is the displacement of the intensity profile, is given in terms of emission coefficients, $\varepsilon(r)$ where r is the radial distance in the source, through the Abel transform:

$$I(x) = 2\int_x^\infty r \frac{\varepsilon(r)}{\sqrt{r^2 - x^2}} dr \tag{136}$$

The inversion integral, or the inverse Abel transform, is given by:

$$\varepsilon(r) = -\frac{1}{\pi}\int_r^\infty \frac{dI/dx}{\sqrt{x^2 - r^2}} dx \tag{137}$$

Because of the difficulty to treat information emitted in the vicinity of the $r = 0$ region, the central part of the plasma is often removed.

2.8.3. Self-absorption

Self-absorption originates from density variation (from a hot light core to a cold dense outer region) forming layers where light is trapped. When a photon is emitted with a wavelength close to the centre of the line, it can be trapped by an atom in the lower state standing on its optical path. This process is all the more efficient that the density of atoms in the lower state is high, and if the lower state is the ground state (*i.e.* if the transition is resonant) the process is extremely efficient. On the other hand, a photon emitted with a shifted energy due to broadening sources (the wing of the line) cannot be captured by an atom in the lower state standing on the path. When the phenomenon is patent, the line centre exhibits readily recognizable self-reversal. Most often, lines are only distorted and the resulting broadening is easily misattributed to another phenomenon. The self-consistency of the assumption that the

plasma is optically thin should always be checked by calculating the optical depth, using emission coefficients and temperature (Griem 1964). For sources of cylindrical symmetry, the total optical depth along a ray designated by its *x* coordinate is:

$$\tau \approx 2\pi \int_x^{r_p} \frac{c^2}{h\nu^3}\left[\exp\left(\frac{h\nu}{k_B T}\right)-1\right]\frac{r}{\sqrt{r^2-x^2}}\varepsilon\, dr \tag{138}$$

where r_p is the plasma radius. ε is calculated with Eq.(137). This equation is not difficult to solve numerically and the accuracy is usually higher than experimental tests. These latter consist in putting a mirror after the plasma to check that the recorded intensity is twice larger when the optical path is doubled. An example of the influence of τ on a Lorentzian line is given in Figure 11.

In the specific case of a Doppler-broadened line, the optical depth is:

$$\tau = \int_0^L \kappa dx \approx \sigma_l \frac{NL}{\Delta\nu} \tag{139}$$

$\sigma_l = \frac{1}{4\pi\varepsilon_0}\frac{\pi e^2}{m_e c} f_{ul}$ is the line-integrated optical depth. Then, the line is thin if $\tau < 1$ with:

$$\tau \approx \frac{1}{4\pi\varepsilon_0}\frac{\pi e^2}{m_e c} f_{ul} \frac{NL}{\nu_0\sqrt{8\ln 2}}\sqrt{\frac{Mc^2}{RT}} \approx 1.611\times 10^{-3} f_{ul}\lambda_0\sqrt{\frac{M}{T}}NL \tag{140}$$

3. APPLICATION TO APP

The terminology "atmospheric pressure plasma" spans over a large range of possible sources. Thorough reviews are available (*e.g.* (Schütze *et al.* 1998) or (Laroussi and Akan 2007)). We chose here to select examples of APPs to illustrate the different aspects of optical emission spectroscopy as described theoretically in the former part.

3.1. Emission intensity

Too many works do not index all transition lines appearing in spectra. This MUST be done. Similarly, very weak lines emitted by metastable states are too often neglected. Measurements

of these lines (like the green line of O due to the O(^{1}S – ^{1}D) transition at ~557.7 nm or the atmospheric band of O_2 due to the $O_2(b^1\Sigma_g^+ - X^3\Sigma_g^-)$ transition at ~762 and 864 nm for instance in late Ar-O_2 afterglows – see Jeong *et al.* (2000)) can be very useful. With iCCD detectors, such measurements are easier, although they remain sometimes difficult to achieve.

Jeong *et al.* (2000) studied the emission of the $O_2(a^1\Delta_g - X^3\Sigma_g^-)$ transition at ~1268 nm. To eliminate the background, they used a lock-in amplifier to enhance the raw signal recorded by an infrared InGaAs detector with an optical chopper run at 100 Hz. The RF power supply was pulsed by a trigger signal. When the delay between the chopper and the RF power supply is set properly, only the light emitted during the afterglow is collected by the spectrometer. The signal varies as the wavelengths are swept, thereby producing the transition profile.

Calibration is needed to get absolute concentration values. This can be done with lamps. This method is well described and not really convenient to apply. The main issues are the positioning of the lamp in place of the plasma, the definition of the solid angle viewed through the slit of the spectrometer, the knowledge of the lamp response (that changes in years) and the optical response of the spectrometer. To circumvent all these problems, an atmospheric pressure plasma can be used. We selected a surfatron discharge excited at 2450 MHz in a 4 mm inner diameter tube (6 mm outer diameter) made of fused silica. If the absorbed power is 200 W, the Ar-0.3vol.%N_2 plasma should be made of 2 filaments of ~5 cm in length for a total flow rate of 10 slm (standard litre per minute). This leads to an afterglow where the nitrogen atom density is 0.22×[N_2], *i.e.* 8.0×10^{21} m^{-3}, 10 cm downstream the end of the plasma where the gas temperature is 600 K.

The line at 580.4 nm of the $N_2(B^3\Pi_g, v'=11\text{-}A^3\Sigma_u^+, v''=7)$ transition is due to the following processes:

$$N(^4S) + N(^4S) + M \rightarrow N_2(B^3\Pi_g, v'=11) + M \qquad \text{(h)}$$

$$N_2(B^3\Pi_g, v'=11) \rightarrow N_2(A^3\Sigma_u^+, v''=7) \qquad \text{(i)}$$

$$N_2(B^3\Pi_g, v'=11) + M \rightarrow products \qquad \text{(j)}$$

k_{Ar}^{11} is the rate constant (in [m^6 s^{-1}]) of the three-body recombination process (h). Radiative de-excitation (process (i)) and quenching (process (j)) of $N_2(B^3\Pi_g,v'=11)$ occurs at a frequency $\nu_r(11,7)$ and rates $k_{Q,11}^M$. *M* is either Ar, N_2 or N. Assuming a quasi-steady state for $N_2(B^3\Pi_g,v'=11)$, one can derive from Eqs. (1) and (2) a practical relation between $\tilde{I}$ and [N]:

$$\tilde{I} = \frac{\Omega}{4\pi} R(\lambda) V \frac{hc}{\lambda_{580}} A_r(11,7) \frac{k_{Ar}^{11}[N]^2[Ar] + k_{N_2}^{11}[N]^2[N_2]}{A_r(11,7) + k_{Q,11}^{Ar}[Ar] + k_{Q,11}^{N_2}[N_2]} \qquad (141)$$

Using constant values that are only applicable to the $N_2(B^3\Pi_g,v'=11\text{-}A^3\Sigma_u^+,v''=7)$ transition at 580.4 nm and available in (Callede *et al.* 1991), (Ricard *et al.* 1988) and (Ricard *et al.* 2013), *i.e.* $A_r(11,7)=2\times10^5$ s^{-1}, $k_{Ar}^{11}=8.2\times10^{-47}$ m^6 s^{-1}, $k_{N_2}^{11}=4.4\times10^{-46}$ m^6 s^{-1}, $k_{Q,11}^{Ar}=5.5\times10^{-18}$ m^3 s^{-1} and $k_{Q,11}^{N_2}=2.8\times10^{-17}$ m^3 s^{-1}, one finds:

$$\tilde{I} = 66.2 \frac{\Omega}{4\pi} R(\lambda) V \qquad (142)$$

With such a "lamp", if the optical path is kept unchanged, replacing the microwave plasma by the plasma jet gives access to absolute concentrations of emissive species (within a factor of 2) if the change in the emissive volume is known and the optical response of the spectrometer given. This method applies whatever the excitation source if the density of N atoms at one spot of the Ar-N_2 afterglow is known. It can be determined by any method (laser induced fluorescence, mass spectrometry, electron spin resonance, NO titration, etc.)

3.2. Recombining and ionizing plasmas

The so-called "torche à injection axiale" or TIA is a microwave plasma jet. Argon and helium plasmas were investigated in details by several groups ((Álvarez *et al.* 2005), (Bae *et al.* 2006), (Benoy *et al.* 1993), (Cobine and Wilbur 1951), (Moisan *et al.* 1994) or (Swift 1964)). Its behaviour is complex. Bae *et al.* (2006) claim that the TIA is in the proximity of local thermodynamic equilibrium but they used a wrong expression of the Griem criterion,

underestimating the critical electron density by a factor of 10^6 (with respect to Eq.(19) and only 10^5 with respect to Eq.(20) that should be used here). In fact, the TIA is far from **L.T.E.**, as showed by Rodero *et al.* (1996) using the b_1 parameter that represents the equilibrium deviation of the ground state and is equal to the ratio between its real population and the corresponding Saha–Boltzmann population. Jonkers *et al.* (1996) and later Timmermans *et al.* (2003) determined the ASDF in argon and in helium (figure 12). These plasma jets are qualified as "ionizing" plasmas because the lowest states of the ASDF are overpopulated with respect to the equilibrium, in agreement with the definition given by Fijimoto and McWhirter (1990) for a **pL.T.E.** Rodero *et al.* (1996) showed that the population of the excited states scales as p^{-6},[xix] as proposed by Fijimoto and McWhirter (1990). However, the larger difference with the electron temperature deduced from the Saha equation is obtained for the highest levels whereas, if **pL.T.E.** prevailed, it should be the lowest ones. So, the TIA is not even in **pL.T.E.**

More recently, Sismanoglu *et al.* (2009) used a microtubular cathode non-thermal DC microplasma jet, a specific case of micro-hollow cathode discharge, and determine the value of the excitation T_{exc} and T_e electron temperatures. These authors employed four different methods: They used 2 Ar I lines and found T_{exc} ~ 8,000 K. They applied the same method with two copper lines and got the same excitation temperature. The Boltzmann-plot method for 4p–4s and 5p–4s Ar I transition lines gave T_{exc} ~ 12,000 K and the Saha–Boltzmann method which has resulted in T_{exc} ~ 4,500 K, far from other results. Although all these results do not agree, this approach is certainly the best to apply. Checking the consistency of a set of results is the only way to get reliable data.

[xix] p is here an effective principal quantum number (hydrogenic approximation) and it can be fractional.

Then, taking the excitation temperature of the upper part of the ASDF to determine the electron temperature can be completely wrong. At least, the lower part should be included to get an idea of the discharge behaviour in terms of excitation processes.

3.3. Temperatures

The rotational spectra of the $OH(A^2\Sigma^+,v'=0 \rightarrow X^2\Pi,v''=0)$ transition at 306-312 nm, $N_2(C^3\Pi_u,v' \rightarrow B^3\Pi_g,v''=v'+2)$ transition at 368-382 nm are the most frequently used to determine the gas temperature of atmospheric plasma jets (Laroussi and Lu (2005), Hong and Uhm (2006) or Machala *et al.* (2007)).

As explained in paragraph 2.4, if several rotational temperatures are found, *i.e.* if the simulation of experimental spectra does not give accurate results, the Boltzmann plot method should be preferred. Sarani *et al.* (2010) observe in a two-electrode plasma jet excited by a sinusoidal wave voltage generated at a frequency of 71 kHz that an error in the estimation of the temperature of the OH radical by spectrum simulation increases with the increase in water content in the argon discharge. These authors found three different domains in terms of quantum rotational number J. They measured T_r = 625 K if $J < 13$, T_r = 5,000 K if $13 < J < 25$ and observed another region for $J > 25$ characterized by a fast depopulation of rotational-vibrational levels. The origins of the two different temperatures were assigned to the following formation processes of the $OH(A^2\Sigma^+)$ radical:

$$OH(X^2\Pi)+e \rightarrow +OH(A^2\Sigma^+)^* +e \ (E_{threshold} = 4\ eV) \qquad (k)$$

$$H_2O(X^1A_1)+e \rightarrow H_2O(B^1A_1)+e \rightarrow OH(A^2\Sigma^+)^{**} +H+e \ (E_{threshold} = 10\ eV) \qquad (l)$$

where $OH(A^2\Sigma^+)^{**}$ are radicals at high excited levels. Population of radicals above J = 25 is depleted because the excitation energy of these levels is close to the predissociation of OH radicals.

It is important to note here that in atmospheric plasma jets submitted to strong gradients, because different excitation mechanisms are possible at different locations, accurate spatially-

defined information is needed. Recently, Mašláni and Sember (2014) showed in a plasma jet generated by a plasma torch with hybrid water-argon stabilization that rotational temperatures near the jet axis, in spite of well-defined Boltzmann plots, do not represent kinetic temperatures of the plasma but describe the region surrounding the hot core. In this hotter area, the plasma is thermalized and a Boltzmann distribution is observed even for high rotational numbers and simultaneously, it is cold enough to have high concentration in OH molecules. In the jet periphery, the medium departs from thermal equilibrium and excited OH is likely produced from water by other mechanisms than those mentioned previously like charge transfer and dissociative recombination, which enhances higher rotational states.

For a probe molecule like $N_2(C^3\Pi_u)$, although equilibrium can be reach at room temperature (see footnote v), we showed that at higher temperature, the distribution of its rotational levels is defined by the way this excited nitrogen molecule is created. In argon, $N_2(C^3\Pi_u)$ can be produced by non-resonance excitation of N_2 after collision with argon metastable states:

$$N_2(X^1\Sigma_g^+) + Ar^* \rightarrow + N_2(C^3\Pi_u) + Ar \qquad \text{(m)}$$

Sarani *et al.* (2010) showed that the rotational temperature of $N_2(C^3\Pi_u)$ molecules is highly overestimated because of this specific reaction pathway.

So, before fitting any molecular rotational spectrum, a careful analysis of the plasma gradients, the possible deviations from equilibrium and the chemical pathways at stake in the different plasma areas has to be done. Another reliable method to determine gas temperature is to resort to line broadening.

3.4. Broadened lines

Dielectric Barrier Discharge (DBD) plasma jets are usually low temperature, low ($<10^{20}$ m^{-3}) electron density media. Then, Doppler and Stark broadening can be neglected. For non-resonant transitions, van der Waals collisions are the main broadening source and the FWHM of the lines must evolve as $T_g^{-0.7}$ (Eq. 65) once subtracted the instrumental broadening. This

method can be used to determine the gas temperature of such sources. Horvatic *et al.* (2014) studied the broadening of specific helium lines together with that of Hα and Hβ lines in a capillary DBD-discharge. As the plasma operates at room temperature, only resonant and van der Waals broadening had to be considered. Stark broadening was negligible with an electron density lower than ~10^{18} m^{-3}. They could determine the broadening parameters of the two hydrogen lines due to collision with neutral helium.

On the other hand, transitions in arc discharges in **L.T.E.** with high electron density (>10^{22} m^{-3}) are broadened and shifted by Stark effect. Then, T_e and N_e can be determined. Most of the works made with atmospheric plasma jets used the Hβ line to determine the electron density only (*e.g.* Ashkenazy *et al.* (1991), Qiuping *et al.* (2009) or Xiao *et al.* (2014)). The electron densities are often close to 10^{20} m^{-3} because lines of other elements are not sufficiently broadened to be used. When the electron density reaches 10^{22} m^{-3}, other lines can be used to measure the electron density. For instance, Yugeswaran and Selvarajan (2006) used the Ar I transition at 430.01 nm. Xiong *et al.* (2013) used the He I transition at 447.1 nm.

3.5. Continua

One of the main issues in the interpretation of continua emission comes from the limited information brought by a smoothly varying intensity spanning over a limited range of wavelengths. Having spectra extended to the UV (or even in the VUV) region or to the near-infra red region facilitates comparison with theoretical prediction.

There are plenty of methods available to determine the electron temperature and the electron density. The reader is begged to refer to the review paper by Hahn and Omenetto (2010). We focus here on the so-calle "line-to-continuum ratio" method (Lockman and Brown (1975), Bastiaans and Mangold (1985), Sola *et al.* (1995)). When electron-ion recombination dominates, the line-to-continuum ratio method can be useful to determine the excitation temperature and to check the possible deviation to equilibrium. This method consists of

evaluating the ratio resulting from the measurement of a line transition and the underlying continuum. This dimensionless ratio is defined from Eqs. (105), (109) and (118), the emissivity being integrated over 4π sr and expressed over the whole plasma volume *V*. Indeed, what is measured experimentally from the continuum is intensity over a finite spectral bandwidth $\Delta\nu_{ul}$. Thus, one has:

$$\frac{I_{ul}}{V\left(\varepsilon_R^{ei}+\varepsilon_B^{ei}\right)4\pi\Delta\nu_{ul}}=\left(\frac{3^{3/2}c^3h^3\left(4\pi\varepsilon_0\right)^3}{256\pi^3e^6k_B}\right)\frac{A_{ul}g_u}{T_eQ_iZ^2}\frac{h\nu_{ul}}{\Delta\nu_{ul}}\frac{\exp\left(\frac{Z^2Ry}{k_BT_e}\right)\exp\left(-\frac{E_u}{k_BT_{exc}}\right)}{\xi_{ff}\exp\left(-\frac{h\nu}{k_BT_e}\right)+\frac{\gamma\xi_{fb}}{Q_i}\left[1-\exp\left(-\frac{h\nu}{k_BT_e}\right)\right]} \quad (143)$$

where $\Delta\nu_{ul}$ is the frequency bandwidth. The two temperatures T_e and T_{exc} must be equal. If T_{exc} is measured independently by the Boltzmann approach for instance, the ratio $\frac{I_{ul}}{V\left(\varepsilon_R^{ei}+\varepsilon_B^{ei}\right)4\pi\Delta\nu_{ul}}$ being determined experimentally, Eq.(143) must give T_e=T_{exc}. Any discrepancy between the two values is attributed to a departure from **L.T.E.** Note that, since the line and the continuum are measured practically at the same wavelength, no calibration of the detection system is necessary.

Concerning the continuum emission by molecules, Lommatzsch *et al.* (2007) observed the emission of continua 3-4 mm downstream the nozzle of an atmospheric pressure plasma jet system run in dry air (Figure 13). The yellow continuum emission of excited NO_2 molecules (450–800 nm) is generated by the chemiluminescence reaction (g). Obviously, there is another continuum emission centred at ~280 nm. It might correspond to the Hartley band of ozone which consists of a broad continuum absorption in the spectral region from 200 to 310 nm. Continua with low-intensity are often difficult to identify and most often, their presence only permits a minimum interpretation (*e.g.* Milosavljevic *et al.* 2014).

3.6. Getting, improving or completing spectroscopic data

Optical emission spectroscopy can be used to get, improve or complete our knowledge on emitting systems. We present here the example of the atmospheric band of O_2 around 760 nm produced by the transition $O_2\left(b^1\Sigma_g^+, v'=0\right)\rightarrow O_2\left(^3\Sigma_g^-, v''=0\right)$ and around 770 nm by the transition $O_2\left(b^1\Sigma_g^+, v'=1\right)\rightarrow O_2\left(^3\Sigma_g^-, v''=1\right)$. Although the corresponding transition intensities are weak since they are produced from metastable states, they can be studied in atmospheric pressure microwaves afterglow at atmospheric pressure (see (Cardoso *et al.* 2011) for a description of the plasma source and the experimental conditions). The atmospheric band of O_2 is interesting first, because oxygen afterglows are weakly luminescent and this system is the most intense available and second, because it may be used to determine the concentration in oxygen atoms. Touzeau *et al.* (1991) used it to determine the rotational temperature in the positive column of a luminescent discharge.

The theoretical data required to simulate the two transitions are taken from Touzeau *et al.* (1991). But these data are incomplete and insufficient to describe the whole spectra measured in our conditions. Indeed, data corresponding to transitions with rotational levels $J' > 40$ for $O_2\left(b^1\Sigma_g^+, v'=0\right)\rightarrow O_2\left(^3\Sigma_g^-, v''=0\right)$ and $J' > 24$ $O_2\left(b^1\Sigma_g^+, v'=1\right)\rightarrow O_2\left(^3\Sigma_g^-, v''=1\right)$ for have never been determined to our knowledge. Indeed, at low gas temperature (*i.e.* a few hundreds of K), as those found in the discharges of Touzeau *et al.* (1991) or Macko and Veis (1999), these levels are too weakly populated to give sensitive contributions in the spectrum. In the microwave afterglow used here, the gas temperature is close to 2000 K (Cardoso *et al.* 2011) and these contributions cannot be neglected. Then, experimental spectra may be used to determine lacking data. The following equations, given by Hertzberg (1950), and the required constants, given by Kuprenie (1972) have to be solved. For the upper level $O_2\left(b^1\Sigma_g^+\right)$, energies F' of the rotational levels are determined as a function of $J' = K'$ (because it is a singlet state) and v' through:

$$F'(v', J') = T_e' + G'(v') + B_{v'}' \times J'(J'+1) - D_{v'}' \times [J'(J'+1)]^2 \quad (144)$$

$$G'(v') = \omega_e' \times \left(v'+\frac{1}{2}\right) - \omega_e' x_e' \times \left(v'+\frac{1}{2}\right)^2 + \omega_e' y_e' \times \left(v'+\frac{1}{2}\right)^3 \quad (145)$$

with the molecular constants $T_e', \omega_e', \omega_e' x_e', \omega_e' y_e', B_{v'}', D_{v'}'$ given in table 3. For the ground state $O_2\left(X\,^3\Sigma_g^-\right)$, energies F'' of rotational levels J'' are determined as a function of *J″* = K''+1, *K″* or *K″*-1 (because it is a triplet state) and *v″* through:

$$\begin{aligned} F''(v'', J'') = {} & G''(v') + B_{v''}'' \times K''(K''+1) - D_{v''}'' \times [K''(K''+1)]^2 \\ & + (2K''+3)B_{v''}'' - \lambda - \sqrt{(2K''+3)^2 B_{v''}''^{\,2} + \lambda^2 - 2\lambda B_{v''}''} + \gamma(K''+1) \qquad \text{if J''} = \text{K''}+1 \end{aligned}$$

$$F''(v'', J'') = G''(v') + B_{v''}'' \times K''(K''+1) - D_{v''}'' \times [K''(K''+1)]^2 \qquad \text{if J''} = \text{K''} \quad (146)$$

$$\begin{aligned} F''(v'', J'') = {} & G''(v') + B_{v''}'' \times K''(K''+1) - D_{v''}'' \times [K''(K''+1)]^2 \\ & - (2K''-1)B_{v''}'' - \lambda + \sqrt{(2K''-1)^2 B_{v''}''^{\,2} + \lambda^2 - 2\lambda B_{v''}''} - \gamma K'' \qquad \text{if J''} = \text{K''}-1 \end{aligned}$$

$$G''(v'') = \omega_e'' \times \left(v''+\frac{1}{2}\right) - \omega_e'' x_e'' \times \left(v''+\frac{1}{2}\right)^2 + \omega_e'' y_e'' \times \left(v''+\frac{1}{2}\right)^3 \quad (147)$$

with the molecular constants $\omega_e'', \omega_e'' x_e'', \omega_e'' y_e'', B_{v''}'', D_{v''}''$ and the splitting constant λ and γ given in Table 3. The Höln-London factors S(*J′*,*J″*) are needed next and they are calculated for each branch as done by Touzeau *et al.* (1991) – see also Table 3 –.

The theoretical data required to simulate the rotational spectra of the two selected transitions up to J'=100 are calculated. The wavelength of the different lines is given by:

$$\lambda = \frac{10^{-7}}{F'(v', J') - F''(v'', J'', K'')} \quad (148)$$

Knowing the energy *F′*(*v′*,*J′*) of the upper level of the transition and the Höln-London factor S(*J′*,*J″*), the intensity of the line reads:

$$I = C \times S(J', J'') \times \exp\left(-\frac{hcF'(v', J')}{k_B T_r}\right) \quad (149)$$

The supplementary data are compared to the set given by Touzeau *et al.* (1991) in figure 14. Finally, the best theoretical spectra with each set of data are presented in figure 15, the one proposed in this work leading to a much better agreement with the experimental data for a realistic value of the rotational temperature, the gas temperature in this case being close to 2000 K.

3.7. Examples

In this last part, we wish to give examples of discharge studies by optical emission spectroscopy. For the sake of conciseness, only examples of Surface-Wave driven microwave Discharges (SWD) excited by a surfatron will be presented.

In figure 16, a survey spectrum of an argon SWD at atmospheric pressure generated in a fused silica tube of 1 mm in inner diameter is depicted (power 71 W, argon flow rate = 1000 standard cubic centimetres per minute, measured plasma length = 32 mm). The spectrum is given in two parts: one below 650 nm and one above. Indeed, because of the difference in intensity between the argon lines in each spectral domain, it is necessary to increase the gain of the iCCD to observe the continuum emission around 450 nm. The spectrum is characterised by argon transitions and by three other weak contributions due to H (Hα line at 656 nm and Hβ line at 486 nm) and OH (rotational spectrum at 306 nm – not provided for it is the only one visible below 400 nm). These contributions are due to water, always present as impurity in atmospheric pressure plasmas. The fact that the Hα line is hardly visible, contrary to the Hβ line, is due to the modification of the iCCD gain. Thanks to these impurities, the electron density is determined from the stark broadening of hydrogen lines (n_e = 1.0 ± 0.5 10^{14} cm^{-3}) and the rotational temperature of OH is assumed to be in equilibrium with the background gas (here T = 950 ± 50 K). The excitation temperature is given by the Boltzmann plot using argon transitions. The continuum is generally attributed to electron-ion recombination and it can be used to determine the electron temperature (Sola *et al.* 1995), (Moussounda *et al.* 1985).

Values around 1 eV are generally obtained for both T_e and T_{exc}. Collisional broadening of neutral argon lines can be used also to determine the electron density and gas temperature. The gas temperature can be obtained from the Van der Waals broadening, provided that the Stark broadening is negligible. This can be achieved by using lines from low-lying levels (close to the ground state). On the other hand, lines corresponding to transitions from high-lying levels, which are more sensitive to Stark (quadratic) broadening, can be utilized to determine electron density (Christova *et al.* 2004).In figure 17a, a spectrum of the same kind of SWD in argon is presented (Jiménez *et al.* 2008). The discharge is created in a fused silica tube of 1.5 mm in inner diameter (power 200 W, argon flow rate = 500 standard cubic centimetres per minute, measured plasma length = 70 mm). The presence of NH lines is due to air impurities, nitrogen leading also to other emission bands of N_2 and N_2^+. Species obtained from the decomposition of the alcohol molecules introduced into the discharge give new contributions, reforming of alcohols being interesting for the synthesis of molecular hydrogen. Emissions from molecular species such as CN, C_2 and a minority contribution of CH are detected. If Jiménez *et al.* (2008) noticed an increase in the OH band, they could not detect neither the hydrogen Fulcher band emitting in the 560–640 nm interval nor the CO bands at 288.3 observed under reduced pressure conditions (Yanguas-Gil *et al.* 2004). Henriques *et al.* (2011) showed also the presence of atomic transitions of atomic carbon at 244.9 and 248.9 nm. They estimated the electron density from the stark component of the Hα broadening within the range 3.3×10^{13} cm^{-3} – 5.4×10^{14} cm^{-3}, the Hβ transition being not observed. Indeed, estimations showed that resonance and natural broadening were negligible and the van der Waals broadening was determined by knowing the gas temperature estimated from the OH rotational spectrum (~3000 K). Because fused silica cannot host such a hot plasma (the melting temperature of the tube being around 2000 K), either OH is not in equilibrium or huge temperature gradients exist. Rincón *et al.* (2014) studied an argon-ethanol

discharge confined in the tube (same experimental device as Jiménez *et al.* (2008)), thus suppressing the influence of air impurities. Then, no CN or NH emission was observed. They determined a higher electron density n_e = 4.0×10^{14} cm^{-3} at 200 W and a lower gas temperature (1400 K). They also observed the presence of the atomic carbon lines.

From these different studies, we notice that optical emission spectroscopy can give very spread data, depending on the experimental conditions. All the information available in these spectra is not exploited. Only partial results are obtained and an overall understanding of the discharge lacks either to crosscheck data and evaluated their consistency or to understand the causes of their discrepancy.

(Santos *et al.* 2014) developed a thorough collisional-radiative model to describe the behavior of a SWD in helium in a fused silica tube of 3 mm in inner diameter (power 180 W, argon flow rate = 2100 standard cubic centimetres per minute, measured plasma length = 1 cm). The spectrum is typical of helium plasmas where impurities can play an essential role if their concentrations exceed several hundreds of ppm (Cardoso *et al.* 2007), air impurities being not reliable probes in general to estimate the gas temperature. Sodium is released from walls of the fused silica tube whereas argon comes from helium bottles which usually contains small amounts of argon. Second and even third order rotational spectra of OH are clearly visible and can be exploited for simulations with improved resolution. The electron density was determined from the Hβ Stark broadening, the gas temperature from the ro-vibrational transitions of OH and the populations of excited states in the energy region 22.7–24.2 eV, whose spectrum allows determining the excitation temperature. Measurements yielded n_e = 2.45×10^{13} cm^{-3}, T_g = 1700 K and T_{exc} = 2793 K. The model predictions at n_e = 1.7×10^{13} cm^{-3} are in very good agreement with measurements yielding T_g = 1800 K, T_{exc} = 2792K (for ∼30% average relative error between calculated and measured excited-state densities), and a power absorbed by the plasma per unit length of 165 W cm^{-1}. Then, the emission of the

continuum centred around 450 nm cannot be attribution to electron-ion recombination, the electron density being too small.

4. CONCLUDING REMARKS

Optical emission spectroscopy is the easiest method to characterize *in situ* a plasma without altering it. However, it brings reliable information only if the data can be cross-checked, either among them (the gas temperature obtained by a rotational spectrum must be the same as the gas temperature needed to evaluate the broadening of a line by Van der Waals collisions) or with data derived from other diagnostics (LIF, Thomson scattering, probes, etc.).

In atmospheric plasma jets, gradients are essential, and OES measurements are very powerful to map them with a good precision if the medium is optically thin, or say, thin enough. Of course, it can be tricky because of the complex geometry the jet can have, because of the optical thickness or because of the low dimension of the jet, especially for micro-discharges.

A key issue of OES is that what you see is usually not what matters most. Ground state or metastable atoms or molecules often determine the important chemical pathways at stake in the plasma. Surface processes cannot be investigated directly, even though some information can be obtained from their impact on gas phase emission.

Any OES campaign will be exciting first, because of the large amount of new information it will have brought, and frustrating next, because of the lack of information that are sought. This will open the way to more specified and complementary diagnostics, and also to comparison with theory, which remains essential for a thorough understanding of plasmas.

Constants

α	Fine structure constant	[–]	7.29735257×10^{-19}
e	Electron charge	[C]	1.60217657×10^{-19}
c	Light speed in vacuum	[m s^{-1}]	2.99792458×10^{8}
ε_0	Vacuum permittivity	[F m^{-1}]	8.85418782×10^{-12}
m_e	Electron mass	[kg]	9.10938970×10^{-31}
a_0	Bohr's radius	[m]	5.29176813×10^{-11}
R_∞	Infinity Rydberg's constant	[m^{-1}]	1.09737316×10^{7}
Ry	Rydberg's constant	[J]	2.17987218×10^{-18}
h	Planck's constant	[m^2 kg s^{-1}]	6.62606957×10^{-34}
$\hbar$	Reduced Planck's constant	[m^2 kg s^{-1}]	1.05457173×10^{-34}
m_u	Atomic mass unit	[kg]	1.66053892×10^{-27}
k_B	Boltzmann's constant	[J K^{-1}]	1.3806488×10^{-23}

Variables

A_{ul}	Einstein's coefficient for spontaneous emission	[s^{-1}]
B_{lu}	Einstein's absorption coefficient	[$m^3 \cdot J^{-1} \cdot s^{-2}$]
B_{ul}	Einstein's stimulated emission coefficient	[$m^3 \cdot J^{-1} \cdot s^{-2}$]
B_e, D_e, H_e	Spectroscopic constants	[J]
B_v	Energy of a rigid rotator	[J]
B_ν	Spectral radiance (Planck's function)	[W sr^{-1} m^{-2} Hz^{-1}]
D_v, H_v	Centrifugal distorsion constants	[J]
E	Level energy	[J]

F_0	Normal field strength	[V m^{-1}]
f	Electron velocity distribution function	[s m^{-1}]
f_{ij}	Oscillation strength of the $i \rightarrow j$ transition	[s m^{-1}]
g	Statistical weight	[–]
G	Vibrational energy level	[W]
I	Intensity	[W]
J	Rotational quantum number	[–]
l	Azimuthal quantum number	[–]
m	Mass	[kg]
n	Principal quantum number	[–]
N	Number density	[m^{-3}]
P	Pressure	[Pa]
P	Radiated power per unit volume	[W·m^{-3}]
Q	Partition function	[–]
q_i	Elementary charge of species i	[C]
r	radius	[m]
r_D	Debye's shielding parameter	[m]
r_e	equilibrium internuclear distance	[m]
$\left\langle \overline{R}_j^2 \right\rangle$	mean square radius of atom in excited level j	[m]
s	spin quantum number	[–]

T	Temperature	[K]
v	Velocity	[m s^{-1}]
v	Vibrational quantum number	[–]
V	Volume	[m^3]
V	Potential energy	[J]
x_e, y_e, z_e	Anharmonicity constants	[–]
z	Effective number of charge	[–]
Z	Atomic number	[–]

Greek variables

α_e, β_e, γ_e	Spectroscopic constants	[J]
α	Polarisability	[m^3]
ε	emissivity	[W m^{-3} sr^{-1} Hz^{-1}]
κ	Absorption coefficient	[m^{-1}]
λ	Wavelength	[m]
λ_D	Debye's length	[m]
μ	Reduced mass	[kg]
ν	Frequency	[s^{-1}]
ρ_w	Weisskopf's radius	[m]
ρ_m	Mean distance between ions	[m]
ρ_D	Debye's radius	[m]

σ	Cross section	[m^2]
τ	time constant	[s]
ω	Angular frequency	[rad s^{-1}]
$\overline{\omega}$	Wavenumber	[cm^{-1}]

Subscript

B	Bremsstrahlung
D	Doppler
e	Electron
eo	electron-neutral
ei	electron-ion
elec	electronic
exc	Excitation
H	Atomic hydrogen
H^z	Hydrogenic ion
i	Ion
int	Internal
l	Lower level
lj	Lennard-Jones
P	Planck
pr	Proton
qs	Quasi-static
R	Recombination
reac	Reaction
rel	Relaxation
res	Resonance
rot	Rotation

s	*Stark*
th	Thermal
tot	Total
trans	Translation
u	Upper level
vib	Vibration
vdw	van der Waals
0	Central or ground
∞	Infinity

Formulary

$$\overline{\omega} = \frac{0.01}{\lambda} \qquad \omega = \frac{2\pi c}{\lambda} = 2\pi\nu$$

$$\Delta\lambda = -\frac{\lambda^2}{c}\Delta\nu$$

$$\Delta\omega = -\frac{2\pi c}{\lambda^2}\Delta\lambda$$

REFERENCES

(Álvarez *et al.* 2005) R Álvarez, M C Quintero and A Rodero 2005 *J. Phys. D: Appl. Phys.* **38** 3768

(Ashkenazy *et al.* 1991) Ashkenazy J, Kipper R and Caner M 1991 *Phys. Rev. A* **43** 5568

(Bae *et al.* 2006) Bae Y S, Lee W C, Ko K B, Lee Y H, Namkung W and Cho M H 2006 *J. Korean Phys. Soc.* **48** 67

(Behmenburg 1964) Behmenburg W 1964 *J. Quant. Spectrosc. Radiat. Transfer* **4** 177

(Benoy *et al.* 1993) Benoy D A, van der Mullen J A M and Schram D C 1993 *J. Phys. D: Appl. Phys.* **26** 1408

(Butler *et al.* 1975) Butler S, Kahler C and Levy D H 1975 *J. Chem. Phys.* **62** 815

(Callede *et al.* 1991) Callede G, Deschamps J, Godart J L and Ricard A 1991 *J. Phys. D: Appl. Phys.* **24** 909

(Cardoso *et al.* 2007) Cardoso R P, Belmonte T, Keravec P, Kosior F and Henrion G 2007 *J. Phys. D: Appl. Phys.* **40** 1394

(Cardoso *et al.* 2011) Cardoso R P, Belmonte T, Kosior F, Henrion G and Tixhon E 2011 *Thin Solid Films* **519** 4177

(Cobine and Wilbur 1951) Cobine J D and Wilbur D A 1951 *J. Appl. Phys.* **22** 835

(Cooper 1966) Cooper J 1966 *Rep. Prog. Phys.* **29** 35

(Cristoforetti *et al.* 2010) Cristoforetti G, De Giacomo A, Dell'Aglio M, Legnaioli S, Tognoni E, Palleschi V and Omenetto N 2010 *Spectrochim. Acta B* **65** 86

(Christova *et al.* 2004) Christova M, Castanos-Martinez E, Calzada M D, Kabouzi Y, Luque J M and Moisan M 2004 *Appl. Spectrosc.* **58** 1032

(Dalgarno and Lane 1966) Dalgarno A and Lane N F 1966 *Astrophys. J.* **145** 623

(Demtroder 2003) Demtroder W 2003 *Laser spectroscopy: Basic Concepts and Instrumentation* 3rd ed. (Springer)

(Demura 2010) Demura A V 2010 *Int. J. Spectrosc.* **2010** 671073

(Demura *et al.* 2011) Demura A V, Umanskii S Ya, Scherbinin A V, Zaitsevskii A V, Demchenko G V, Astapenko V A and Potapkin B V 2011 *Int. Rev. At. Mol. Phys.* **2** 109

(Denton 1977) Denton J C 1977 *Energy Conv.* **17** 147

(Dyne 1971) Dyne R J 1971 *Proc. Astron. Soc. Aust.* **2** 38

(Fanz 2006) Fanz U 2006 *Plasma Sources Sci. Technol.* **15** S137

(Fujimoto and McWhirter 1990) Fujimoto T and McWhirter R W P 1990 *Phys. Rev. A* **42** 6588

(Fullerton and Cowley 1970) Fullerton W and Cowley C R 1970 *Astrophys. J.* **162** 327

(Gazeli *et al.* 2013) Gazeli K, Noël C, Clément F, Daugé C, Svarnas P and Belmonte T 2013 *Plasma Sources Sci. Technol.* **22** 025020

(Gigosos and Cardeñoso 1996) Gigosos M A and Cardeñoso V 1996 *J. Phys. B: At. Mol. Opt. Phys.* **29** 4795

(Gigosos *et al.* 2003) Gigosos M A, González M Á and Cardeñoso V 2003 *Spectrochim. Acta B: At. Spectrosc*. **58** 1489

(Gillispie *et al.* 1974) Gillispie G D, Khan A U, Hosteney R P, Wahl A C and Krauss M 1974 *Symp. Mol. Struct. Spectrosc.*, 29th Ohio State Univ., Colombus.

(Gold and Trush 1975) Gold M F and Trush B A 1975 *Adv. in atomic and molecular Physics, vol. 11* (Published by Bates D R, Academic Press Inc. New York) pp. 361

(Griem 1963) Griem H R 1963 *Phys. Rev.* **131** 1170

(Griem 1964) Griem H R 1964 *Plasma spectroscopy* (Mc Graw Hill)

(Griem 1974) Griem H R 1974 *Spectral line broadening by plasmas* (Academic press 1974)

Hahn and Omenetto (2010) Hahn D W and Omenetto N 2010 *Appl. Spectrosc.* **64** 335A

(Hammond 1975) Hammond G L 1975 *Astrophys. J.* **196** 291

(Hemming *et al.* 2001) Hemming B L, Crosley D R, Harrington J E and Sick V 2001 *J. Chem. Phys.* **115** 3099

(Henriques *et al.* 2011) Henriques J, Bundaleska N, Tatarova E, Dias F M and Ferreira C M 2011 *Int. J. Hydrogen Energy* **36** 345

(Hertzberg 1950) Herzberg G 1950 *Molecular Spectra and Molecular Structure (Spectra of Diatomic Molecules)* (2^{nd} Ed. New York, Van Nostrand)(Hindmarsh and Thomas 1961) Hindmarsh W R and Thomas K A 1961 *Proc. Phys. Soc.* **77** 1193 and **78** 145

(Hindmarsh *et al* 1967) Hindmarsh W R, Petford D and Smith G 1967 *Proc. Roy. Soc. London* **297A** 296

(Hindmarsh *et al* 1970) Hindmarsh W R, Du Plessis A N and Farr J M 1970 *J. Phys. B: At. Mol. Opt. Phys.* **3** L5

(Hofsaess 1978) Hofsaess D 1978 *J. Quant. Spectrosc. Radiat. Transfer* **19** 339

(Holtsmark 1919) Holtsmark J 1919 *Ann. Phys.* **363** 577

(Hong and Uhm 2006) Hong Y C and Uhm H S 2006 *Appl. Phys. Lett.* **89** 221504

(Horvatic *et al.* 2014) Horvatic V, Müller S, Veza D, Vadla C and Franzke J 2014 *J. Anal. At. Spectrom.* **29** 498

(Huber and Herzberg 1979) Huber K P and Herzberg G 1979 *Molecular Structure and Molecular Spectra. IV. Constants of Diatomic Molecules* (Van Rostrand-Reinhold, New York)

(Irwin 1981) Irwin AW 1981 *Astrophys. J. Suppl. Series* **45** 621

(Irwin 1987) Irwin AW 1987 *Astron. Astrophys.* **182** 348

(Ishiwata *et al.* 1973) Ishiwata T, Akimoto H and Tanaka I 1973 *Chem. Phys. Lett.* **21** 322

(Jain 1980) Jain P C 1980 *J. Phys. D: Appl. Phys.* **13** 25

(Jeong *et al.* 2000) Jeong J Y, Park J, Henins I, Babayan S E, Tu V. J., Selwyn G S, Ding G and Hicks R F 2000 *J. Phys. Chem. A* **104** 8027

(Jiménez *et al.* 2008) Jiménez M, Yubero C and Calzada M D 2008 *J. Phys. D: Appl. Phys.* **41** 175201

(Jonkers *et al.* 1996) Jonkers J, Vos H P C, van der Mullen J A M and Timmermans E A H 1996 *Spectrochim. Acta Part B* **51** 457

(Karzas and Latter 1961) Karzas W J and Latter R 1961 *Astrophys. J. Suppl. Series* **6** 167

(Kepple and Griem 1968) Kepple P and Griem H H 1968 *Phys. Rev.* **173** 317

(Khachkuruzov 1967) Khachkuruzov G A 1967 *Optics Spectrosc.* **22** 11

(Khachkuruzov 1971) Khachkuruzov G A 1971 *Optics Spectrosc.* **30** 455

(Konjević and Roberts 1976) Konjević N and Roberts J L 1976 *J. Phys. Chem. Ref. Data* **5** 216

(Konjević *et al.* 2002) Konjević N, Lesage A, Fuhr J R and Wiese W L 2002 *J. Phys. Chem. Ref. Data* **31** 819

(Kuprenie 1972) Krupenie P H 1972 *J. Phys. Chem. Ref. Data.* **1** 423

(Laporte and Damany 1979) Laporte P and Damany H 1979 *J. Phys.* **40** 9

(Laroussi and Akan 2007) Laroussi M and Akan T 2007 *Plasma Proc. Polym.* **4** 777

(Laroussi and Lu 2005) Laroussi M and Lu X 2005 *Appl. Phys. Lett.* **87** 113902

(Lawler 2004) Lawler J E 2004 *J. Phys. D: Appl. Phys.* **37** 1532

(Leo *et al.* 1992) Leo P J, Mullamphy D F T, Peach G and Whittingham I B 1992 *J. Phys. B: At. Mol. Opt. Phys.* **25** 1161

(Lewis *et al.* 1969) Lewis E L, Rebbeck M M and Vaughan J M 1969 *Phys. Lett.* **30A** 50

(Lifbase 2014) Luque J and Crosley D R 1999 "LIFBASE: Database and Spectral Simulation Program (Version 1.5)", SRI International Report MP 99-009. http://www.sri.com/cem/lifbase.

(Linne 2002) Linne M A 2002 *Spectroscopic measurements. An introduction to the fundamentals* (San Diego, Elsevier Science Ltd)

(Lockman and Brown 1975) Lockman F J and Brown R L 1975 *Astrophys. J.* **201** 134

(Lommatzsch *et al.* 2007) Lommatzsch U, Pasedag D, Baalmann A, Ellinghorst G and Wagner H-E 2007 *Plasma Process. Polym.* **4** S1041

(Lorentz 1906) Lorentz H A 1906 *Proc. Royal Acad. Arts Sci.* **8** 591

(Machala *et al.* 2007) Machala Z, Janda M, Hensel K, Jedlovský I, Leštinská L, Foltin V, Martišovitš V and Morvová M 2007 *J. Molec. Spectrosc.* **243** 194

(Macko and Veis 1999) Macko P and Veis P (1999) *J. Phys. D: Appl. Phys.* **32** 246

(Malvern *et al.* 1980) Malvern A R, Pinder A C, Stacey D N and Thompson R C 1980 *Proc. R. Soc. London A* **371** 259

(Manola *et al.* 1991) Manola S, Dević S and Lesage A 1991 *J. Quant. Spectrosc. Radiat. Transfer* **46** 577

(Margenau 1935) Margenau H 1935 *Phys. Rev.* **48** 755

(Mašláni and Sember 2014) Mašláni A and Sember V 2014 *J. Spectrosc.* **2014** 952138

(Meiners and Weiss 1976) Meiners D and Weiss C O 1976 *J. Quant. Spectrosc. Radiat. Transfer* **16** 213

(Mihalas 1978) Mihalas D 1978 *Stellar Atmospheres* (Ed. Freeman, 2nd Edition, San Francisco)

(Milosavljevic *et al.* 2014) Milosavljevic V, Donegan M, Cullen P J and Dowling D P 2014 *J. Phys. Soc. Jap.* **83** 014501

(Moisan *et al.* 1994) Moisan M, Sauvé G, Zakrzewski J and Hubert J 1994 *Plasma Sources Sci. Technol.* **3** 584

(Moussounda *et al.* 1985) Moussounda P S, Ranson P and Mermet J M 1985 *Spectrochim. Acta B* **40** 641

(NIST 2014) NIST Chemistry WebBook, Standard Reference Database 69, Eds. P.J. Linstrom and W.G. Mallard, National Institute of Standards and Technology, Gaithersburg MD, 20899, http://webbook.nist.gov, (accessed Sept. 26, 2014).

(Oks 2006) Oks E 2006 *Stark Broadening of Hydrogen and Hydrogenlike Spectral Lines on Plasmas* (The Physical Insight. Alpha Science International, Oxford).

(Paulsen *et al.* 1970) Paulsen D E, W F and Huffman R E 1970 *J. Chem. Phys.* **53** 647

(Peach 1996) Peach G 1996 "Collisional Broadening of Spectral Lines" in *Atomic, Molecular, & Optical Physics Handbook* (Drake G W F, AIP Press, New York) pp. 669

(Qiuping *et al.* 2009) Qiuping Z, Cheng C and Yuedong M 2009 *Plasma Sci. Technol.* **11** 560

(Ricard *et al.* 1988) Ricard A, Besner A, Hubert J and Moisan M 1988 *J. Phys. B: At. Mol. Opt. Phys.* **21** L579

(Ricard *et al.* 2013) Ricard A, Oh S-G and Guerra V 2013 *Plasma Sources Sci. Technol.* **22** 035009

(Rincón *et al.* 2014) Rincón R, Jiménez M, Munõz J, Saéz M and Calzada M D 2014 *Plasma Chem. Plasma Process.* **34** 145

(Rival 1993) Rival R, Legentil M, Pasquiers S and Puech V 1993 *J. Phys. B: At. Mol. Opt. Phys.* **26** 4065

(Rodero *et al.* 1996) Rodero A, García M C, Quintero M C, Sola A and Gamero A 1996 *J. Phys. D: Appl. Phys.* **29** 681

(Rosen 1970) Rosen B 1970 *Données spectroscopiques relatives aux molécules diatomiques* (Pergamon Press Vol. 17).

(Sakurai and Broida 1969) Sakurai K and Broida H P 1969 *J. Chem. Phys.* **50** 2404

(Santos *et al.* 2014) Santos M, Noël C, Belmonte T and Alves L L 2014 *J. Phys. D: Appl. Phys.* **47** 265201

(Sapar *et al.* 2006) Sapar A, Poolamäe R and Sapar L 2006 *Baltic Astron.* **15** 435

(Sarani *et al.* 2010) Sarani A, Nikiforov A Yu and Leys C 2010 *Phys. Plasma* **17** 063504

(Schlüter 1968) Schlüter D 1968 *Z. Physik* **210** 80

(Schulz-Gulde 1970) Schulz-Gulde E 1970 *Z. Physik* **230** 449

(Schütze *et al.* 1998) Schütze A, Jeong J Y, Babayan S E, Park J, Selwyn G S and Hicks R F 1998 *IEEE Trans. Plasma Sci.* **26** 1685

(Sismanoglu *et al.* 2009) Sismanoglu B N, Amorim J, Souza-Corrêa J A, Oliveira C and Gomes M P 2009 *Spectrochim. Acta Part B* **64** 1287

(Sola *et al.* 1995) Sola A, Calzada M D and Gamero A 1995 *J. Phys. D Appl. Phys.* **28** 1099

(Specair 2014) Laux C O 2002, "Radiation and Nonequilibrium Collisional-Radiative Models" von Karman Institute Lecture Series 2002-07, Physico-Chemical Modeling of High Enthalpy and Plasma Flows (eds. Fletcher D, Charbonnier J-M, Sarma G S R and Magin T, Rhode-Saint-Genèse, Belgium) See http://www.specair-radiation.net/.

(Swift 1964) Swift J 1964 *Proc. IREE Australia* **25** 779

(Thorne *et al* 1999) Thorne A, Litzen U and Johansson S 1999 *Spectrophysics, Principles and Applications* (Berlin Heidelberg: Springer-Verlag)

(Timmermans *et al.* 2003) Timmermans E A H, van de Sande M J and van der Mullen J J A M 2003 *Plasma Sources Sci. Technol.* **12** 324

(Tkachenko 2006) Tkachenko N V 2006 *Optical Spectroscopy. Methods and Instrumentations* (Oxford: Elsevier).

(Touzeau *et al.* 1991) Touzeau M, Vialle M, Zellagui A, Gousset G, Lefebvre M, Pealat M 1991 *J. Phys. D: Appl. Phys.* **24** 41

(van Hoof *et al.* 2014) van Hoof P A M, Williams R J R, Volk K, Chatzikos M, Ferland G J, Lykins M, Porter R L and Wang Y 2014 *Mon. Not. R. Astron. Soc.* **444** 420

(Vidal *et al.* 1973) Vidal C R, Cooper J and Smith E W 1973 *Astrophys. J. Suppl. Series No.214* **25** 37

(Walsh *et al.* 2007) Walsh J L and Kong M G 2007 *Appl. Phys. Lett.* **91** 221502

(Weisskopf 1932) Weisskopf V 1932 *Z. Physik* **75** 287

(Xiao *et al.* 2014) Xiao D, Cheng C, Shen J, Lan Y, Xie H, Shu X, Meng Y, Li J and Chu P K 2014 *Phys. Plasma* **21** 053510

(Xiong *et al.* 2011) Xiong Q, Nikiforov A, Britun N, Snyders R, Leys C and Lu X 2011 *J. Appl. Phys.* **110** 073302

(Xiong *et al.* 2013) Xiong Q, Nikiforov A Y, González M Á, Leys C and Lu X P 2013 *Plasma Sources Sci. Technol.* **22** 015011

(Yanguas-Gil *et al.* 2004) Yanguas-Gil A, Hueso J L, Cotrino J, Caballero A and Gonzalez-Elipe A R 2004 *Appl. Phys. Lett.* **85** 4004.

(Yugeswaran and Selvarajan 2006) Yugeswaran S and Selvarajan V 2006 *Vacuum* **81** 347

FIGURE CAPTIONS

Figure 1: Example of optical path followed by the light emitted by a given volume, collected by an optical fiber and crossing the optical arrangement of a spectrometer.

Figure 2: Schematic energy level diagram for a hydrogenic species of charge Z–1. After (Cooper 1966).

Figure 3: Potential energy diagram of H_2. Inset: Magnification of the $X\left(^1\Sigma_g^+\right)$ state near the minimum energy, showing the first vibrational levels and the first rotational level of the v=0 state.

Figure 4: Quenching cross section of OH(A,v=0,J) molecules by N_2. After (Hemming *et al.* 2001). Reproduced with permission from the Journal of Chemical Physics (AIP Publishing).

Figure 5: a) Synthetic CH($A^2\Delta$-$X^2\Pi$) transitions for one or two rotational temperatures. b) Corresponding Boltzmann plot.

Figure 6: Example of Lorentzian and Gaussian profiles plotted in a Y-log scale (left Y scale) and in a Y-lin scale (Right Y scale).

Figure 7: a) Hα profile calculated from Griem's tables and Vidal's tables, together with FWHM estimates by Kepple-Griem and Gigoso according to data available in references (Kepple and Griem 1968) and (Gigosos and Cardeñoso 1996).

Figure 8: Evolution of the emissivity due to free-bound, free-free collision for the hydrogen atom.

Figure 9: Evolution of the Ar I free-bound Biberman-Schlüter function as a function of the wavelength for temperatures ranging from 6,000 to 30,000 K. After Hofsaess (1978). Reproduced with permission from the Journal of Quantitative Spectroscopy and Radiative Transfer (Elsevier Publishing).

Figure 10: Fluorescence spectra of NO_2 excited by different laser lines. The pressure of NO_2 is 0.1 torr. Excitation wavelength dependence of spectra is clear. After Sakurai and Broida (1969). Reproduced with permission from the Journal of Chemical Physics (AIP Publishing).

Figure 11: Influence of the optical thickness on the profile of a Lorentzian line. After Xiong *et al.* (2011). Reproduced with permission from the Journal of Applied Physics (AIP Publishing).

Figure 12: The atomic state distribution functions (ASDF) in helium and in argon for a "torche à injection axiale" (TIA). After (Jonkers *et al.* 1996)

Figure 13: Continuum emission observed 3-4 mm from the nozzle of an atmospheric pressure plasma jet system in dry air. After (Lommatzsch *et al.* 2007). Reproduced with permission from Plasma Processes and Polymers (WILEY-VCH Verlag GmbH & Co. KGaA)

Figure 14: Theoretical intensity of the $O_2\left(b^1\Sigma_g^+, v'=0\right)\rightarrow O_2\left(^3\Sigma_g^-, v''=0\right)$ and $O_2\left(b^1\Sigma_g^+, v'=1\right)\rightarrow O_2\left(^3\Sigma_g^-, v''=1\right)$ transitions of the O_2 atmospheric band. Comparison between the present set of data and the one given by Touzeau *et al.* (1991).

Figure 15: Synthetic spectrum the $O_2\left(b^1\Sigma_g^+, v'=0\right)\rightarrow O_2\left(^3\Sigma_g^-, v''=0\right)$ and $O_2\left(b^1\Sigma_g^+, v'=1\right)\rightarrow O_2\left(^3\Sigma_g^-, v''=1\right)$ transitions of the O_2 atmospheric band. a) Best fit with the data set by Touzeau *et al.* (1991). b) Best fit with the present data set. Microwave afterglow of a resonant cavity plasma. Ar-10%vol.O_2. Total flow rate: 1.1 standard litres per minute. Power: 500 W.

Figure 16: Optical emission spectrum of an argon surface-wave discharge at atmospheric pressure generated in a fused silica tube of 1 mm in inner diameter. (Flow rate = 1 standard litre per minute. Power = 71 W).

Figure 17: a) Optical emission spectrum of an argon surface-wave discharge at atmospheric pressure generated in a fused silica tube of 1.5 mm in inner diameter. b) Typical optical

emission spectrum for an argon-alcohol mixture, the alcohol being either methanol, ethanol, butanol or propanol diluted at 20%. (Flow rate = 0.5 standard litre per minute. Power = 200 W). After (Jiménez *et al.* 2008). Reproduced with permission from Journal of Physics D: Applied Physics (Institute of Physics Publishing).

Figure 18: a) Optical emission spectrum of a helium surface-wave discharge at atmospheric pressure generated in a fused silica tube of 3 mm in inner diameter. (Flow rate = 2.1 standard litre per minute. Power = 180 W).

Table 1: Molecular constants of some H_2 states. For all theses states, ω_e z_e=0.0, γ_e=0.0 and H_e=0.0. After (Rosen 1970) and (NIST 2014). Conversion to Joules (SI units –values in italics) is obtained by multiplying each term expressed in cm^{-1} by $100 \cdot h \cdot c = 1.98644568 \times 10^{-23}$. r_e in Å is converted in m.

Table 2: Parameters tabulated by Hindmarsh *et al.* (1967) and needed to determine broadening width and line shift caused by collisions with molecules interacting with a Lennard-Jones potential.

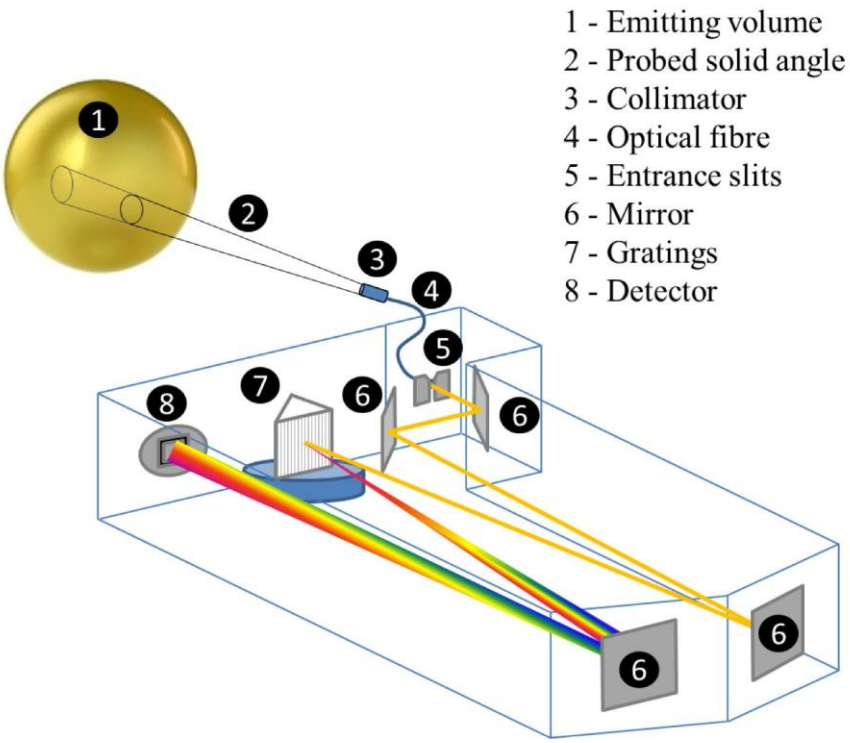

Figure 1: Example of optical path followed by the light emitted by a given volume, collected by an optical fiber and crossing the optical arrangement of a spectrometer.

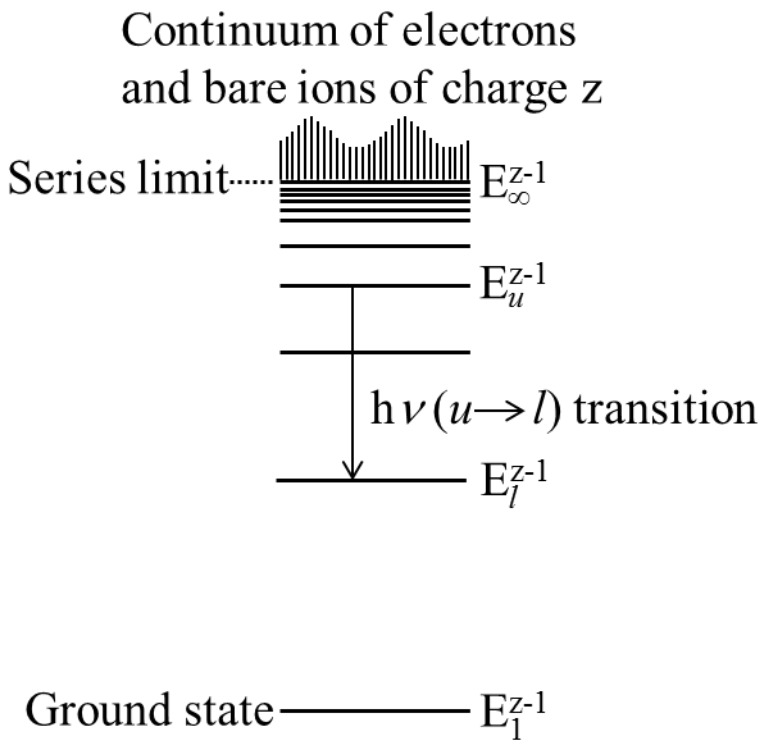

Figure 2: Schematic energy level diagram for a hydrogenic species of charge Z–1. After (Cooper 1966).

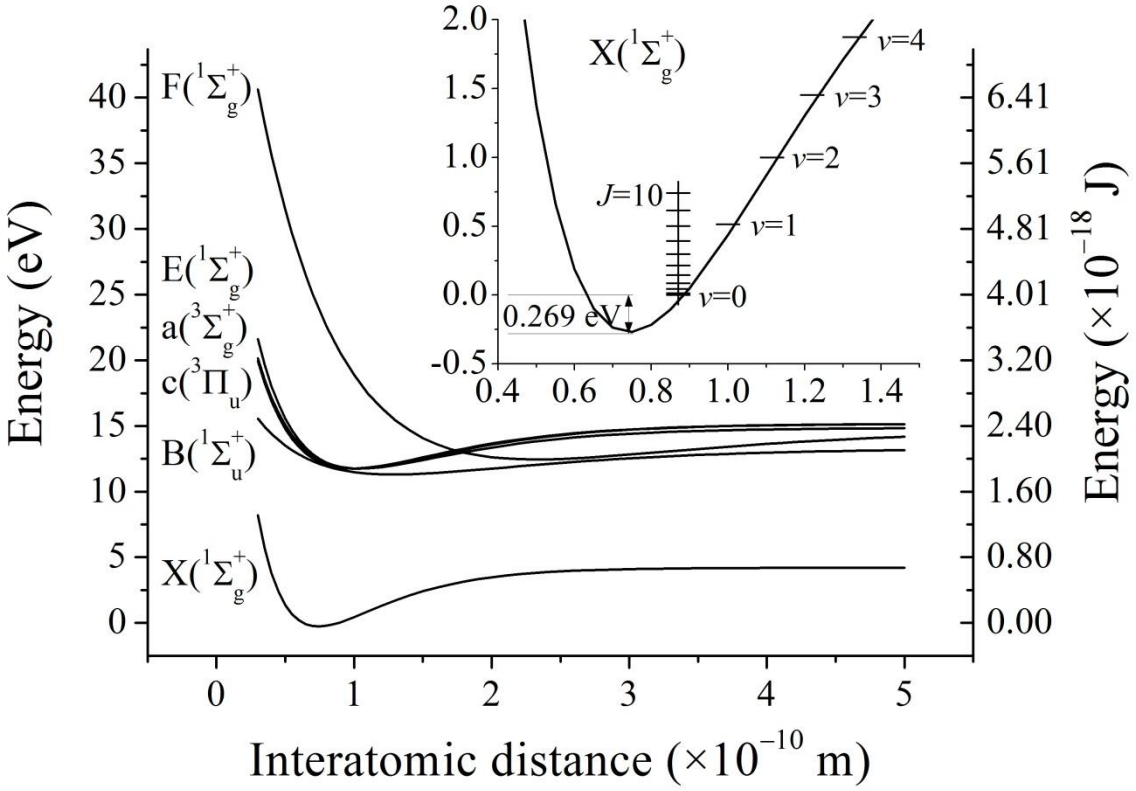

Figure 3: Potential energy diagram of H_2. Inset: Magnification of the $X\left(^1\Sigma_g^+\right)$ state near the minimum energy, showing the first vibrational levels and the first rotational level of the v=0 state.

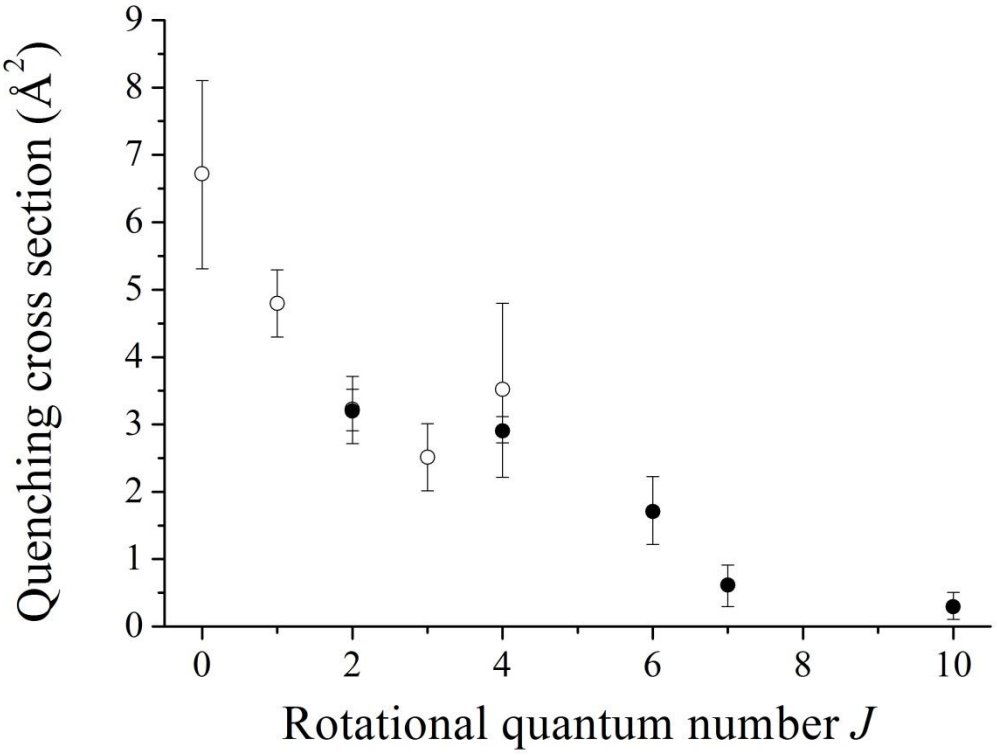

Figure 4: Quenching cross section of OH(A,v=0,J) molecules by N_2. After (Hemming *et al.* 2001). Reproduced with permission from the Journal of Chemical Physics (AIP Publishing).

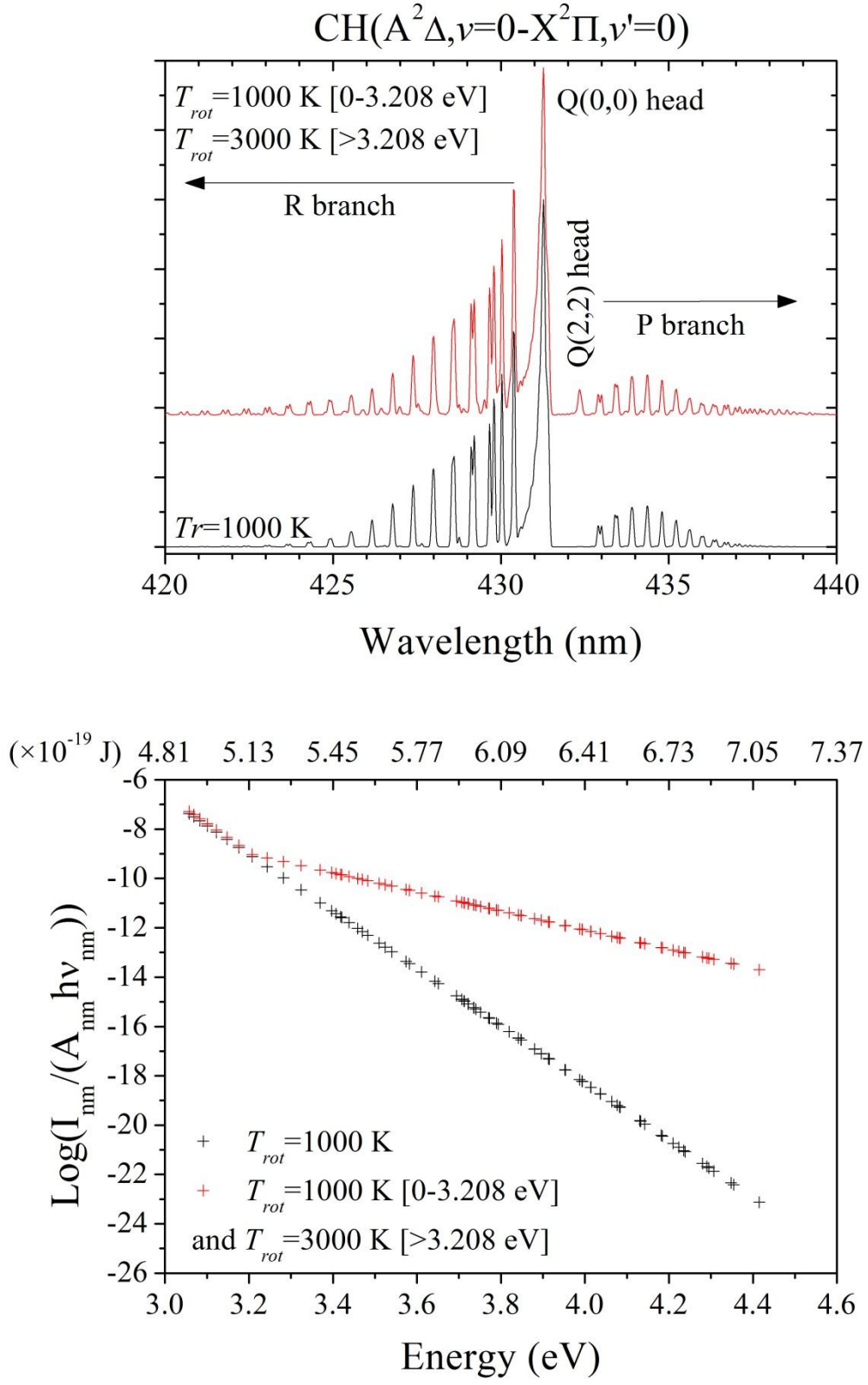

Figure 5: a) Synthetic CH(A-X) transitions for one or two rotational temperatures. b) Corresponding Boltzmann plot.

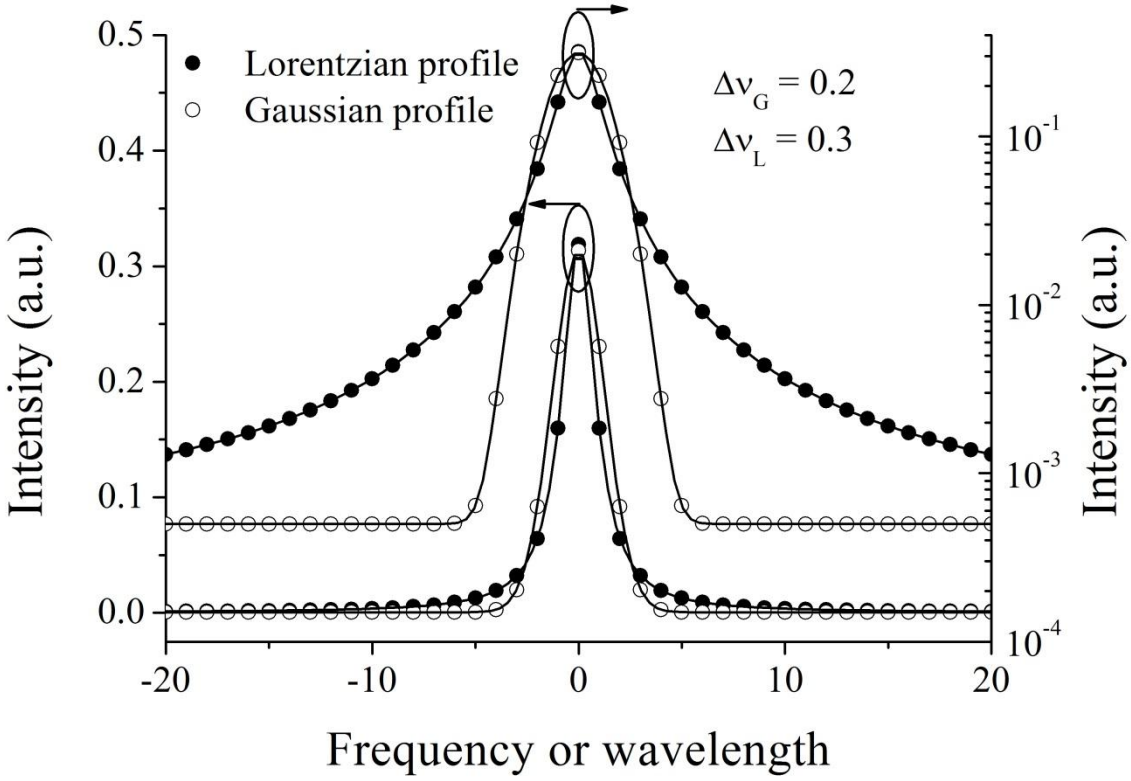

Figure 6: Example of Lorentzian and Gaussian profiles plotted in a Y-log scale (left Y scale) and in a Y-lin scale (Right Y scale).

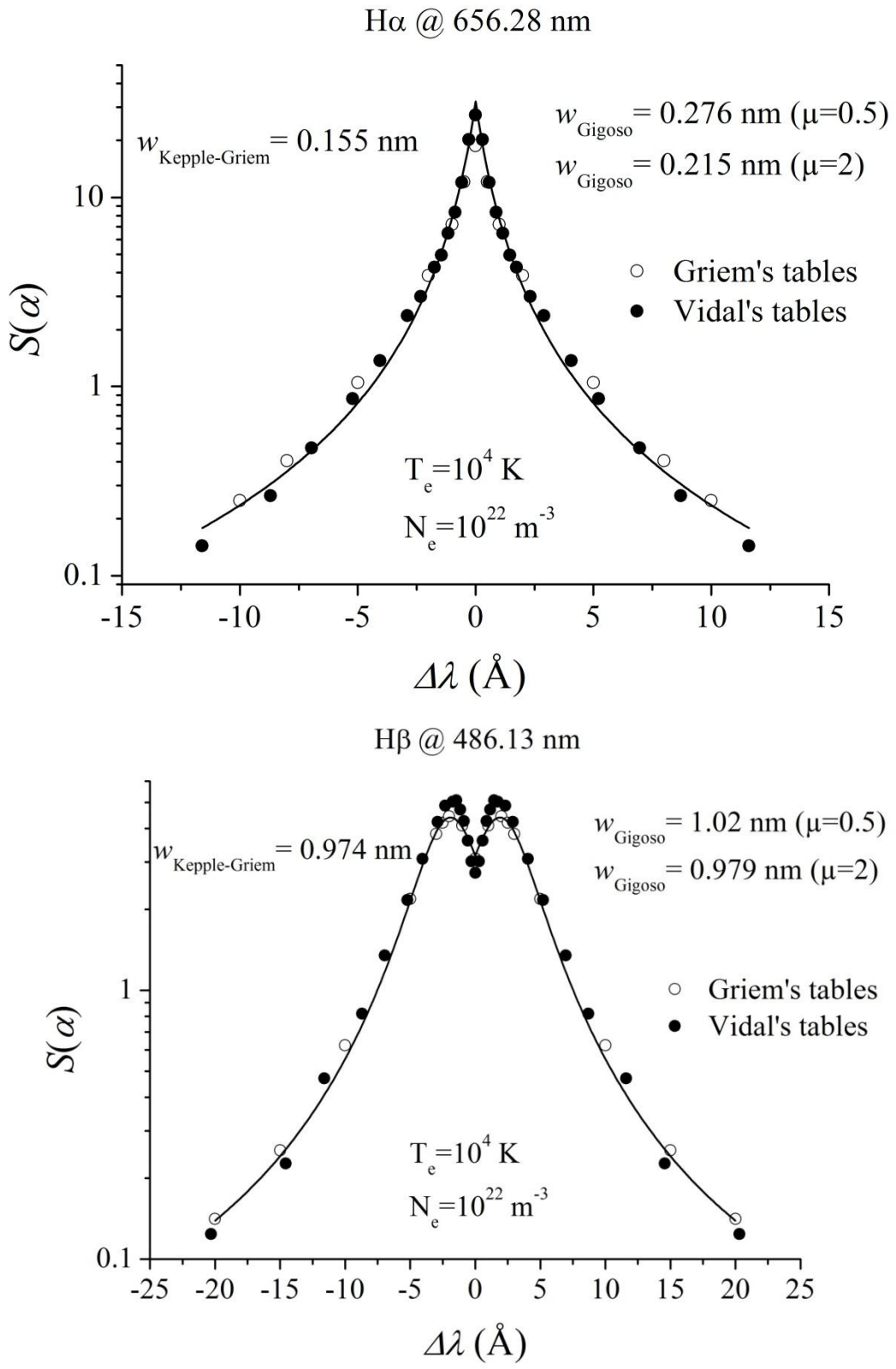

Figure 7: a) Hα profile calculated from Griem's tables and Vidal's tables, together with FWHM estimates by Kepple-Griem and Gigoso according to data available in references (Kepple and Griem 1968) and (Gigosos and Cardeñoso 1996). b) Idem with Hβ.

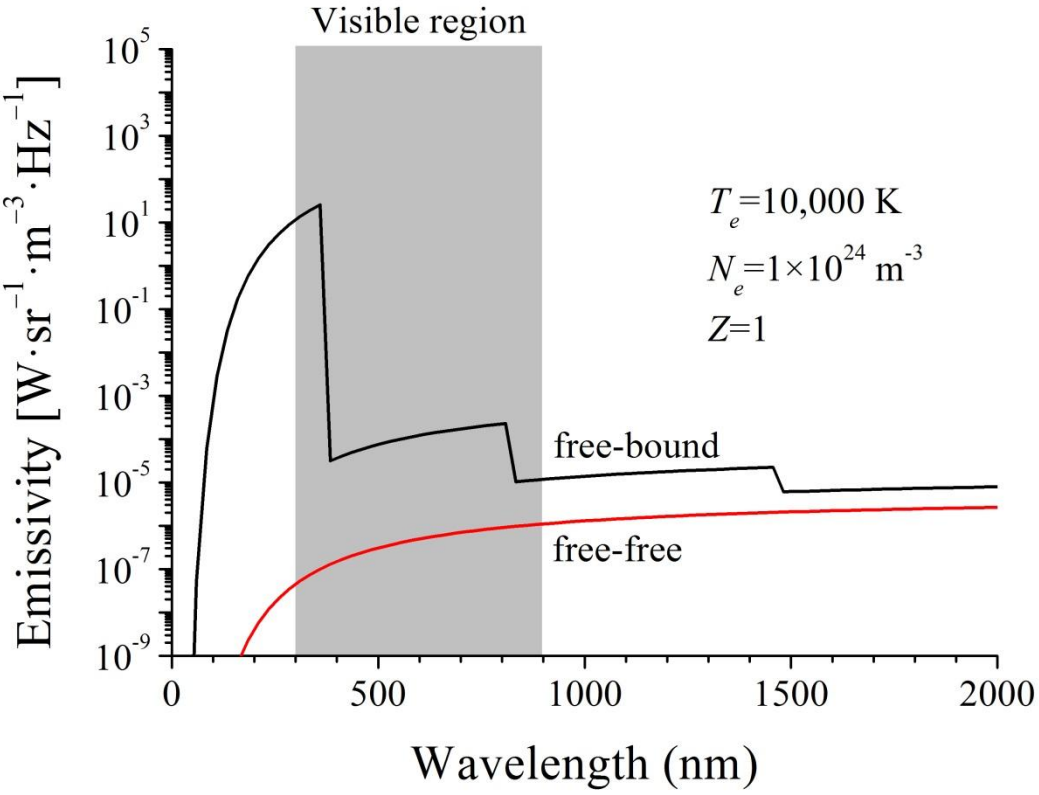

Figure 8: Evolution of the emissivity due to free-bound and free-free collision for the hydrogen atom.

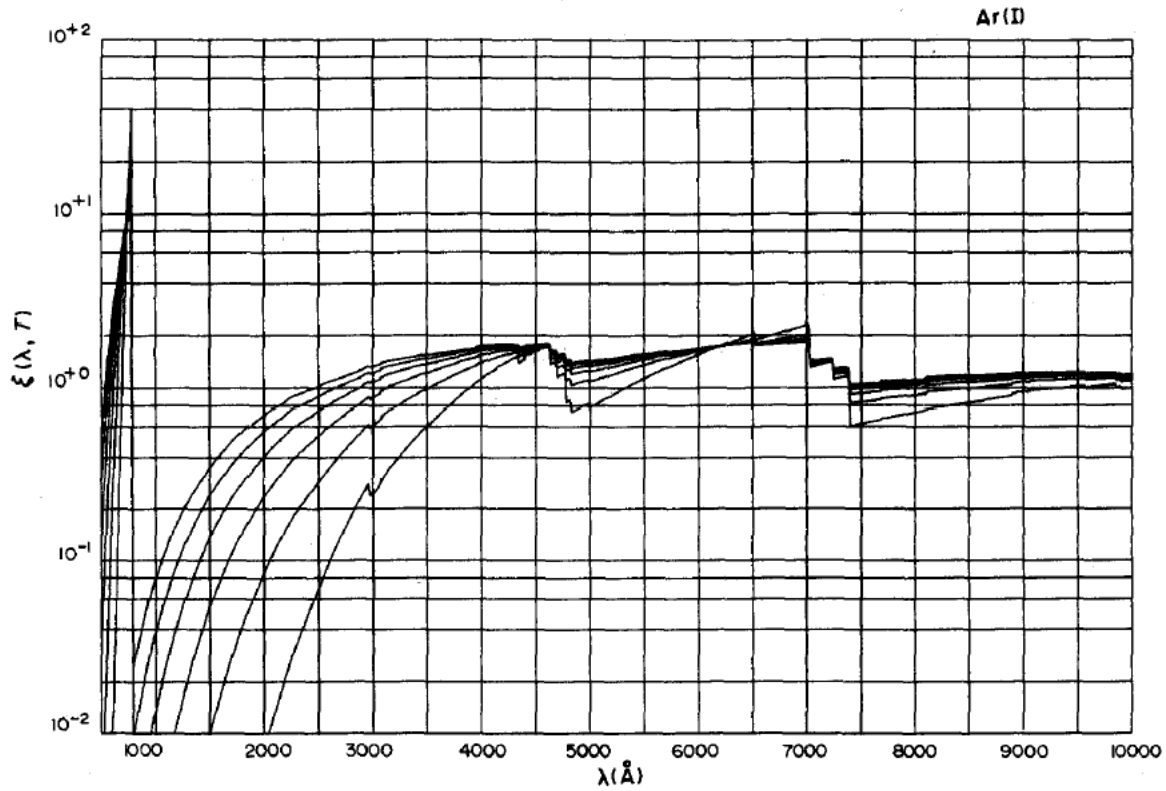

Figure 9: Evolution of the Ar I free-bound Biberman-Schlüter function as a function of the wavelength for temperatures ranging from 6,000 to 30,000 K. After Hofsaess (1978). Reproduced with permission from the Journal of Quantitative Spectroscopy and Radiative Transfer (Elsevier Publishing).

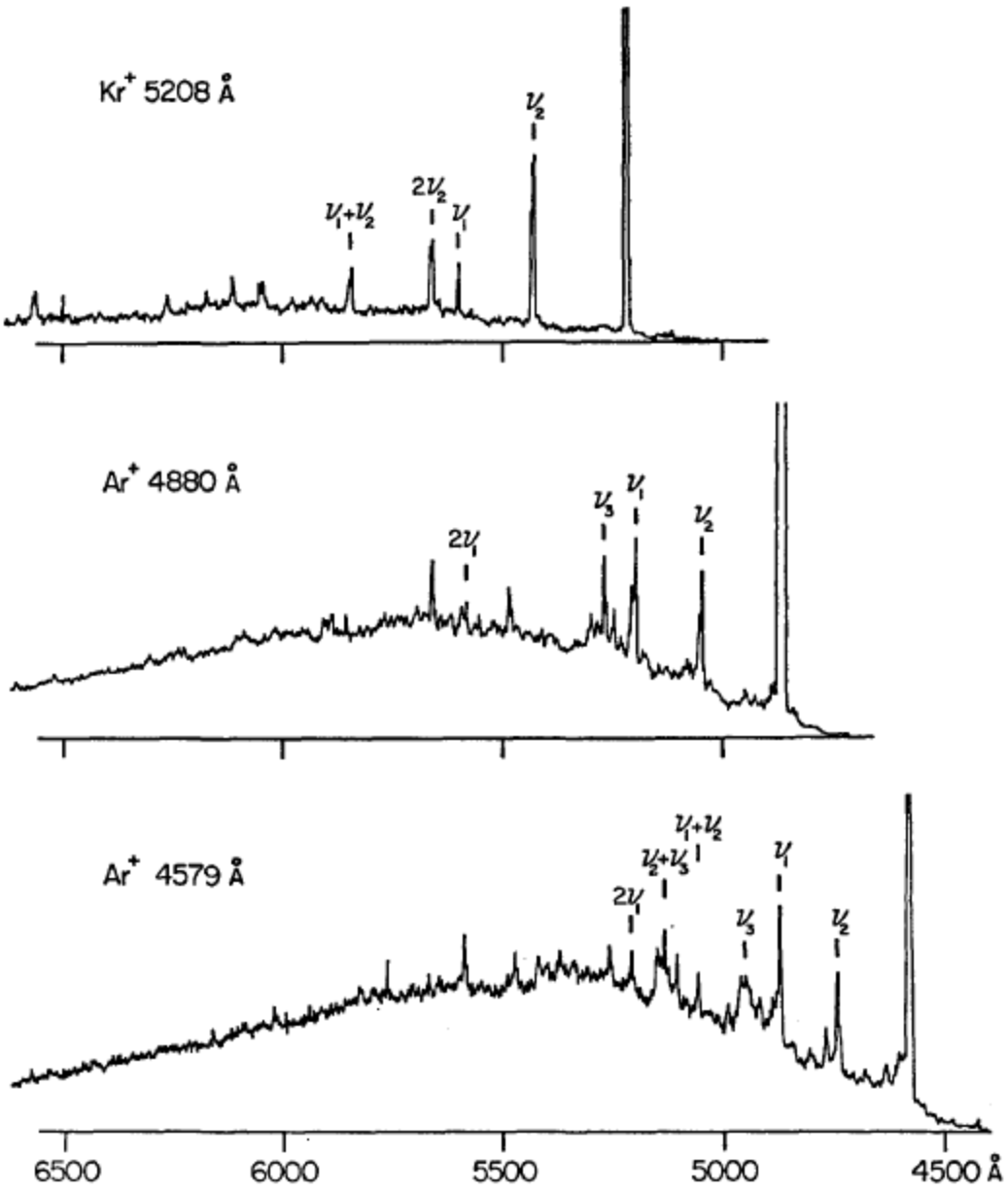

Figure 10: Fluorescence spectra of NO_2 excited by different laser lines. The pressure of NO_2 is 0.1 torr. Excitation wavelength dependence of spectra is clear. After Sakurai and Broida (1969). Reproduced with permission from the Journal of Chemical Physics (AIP Publishing).

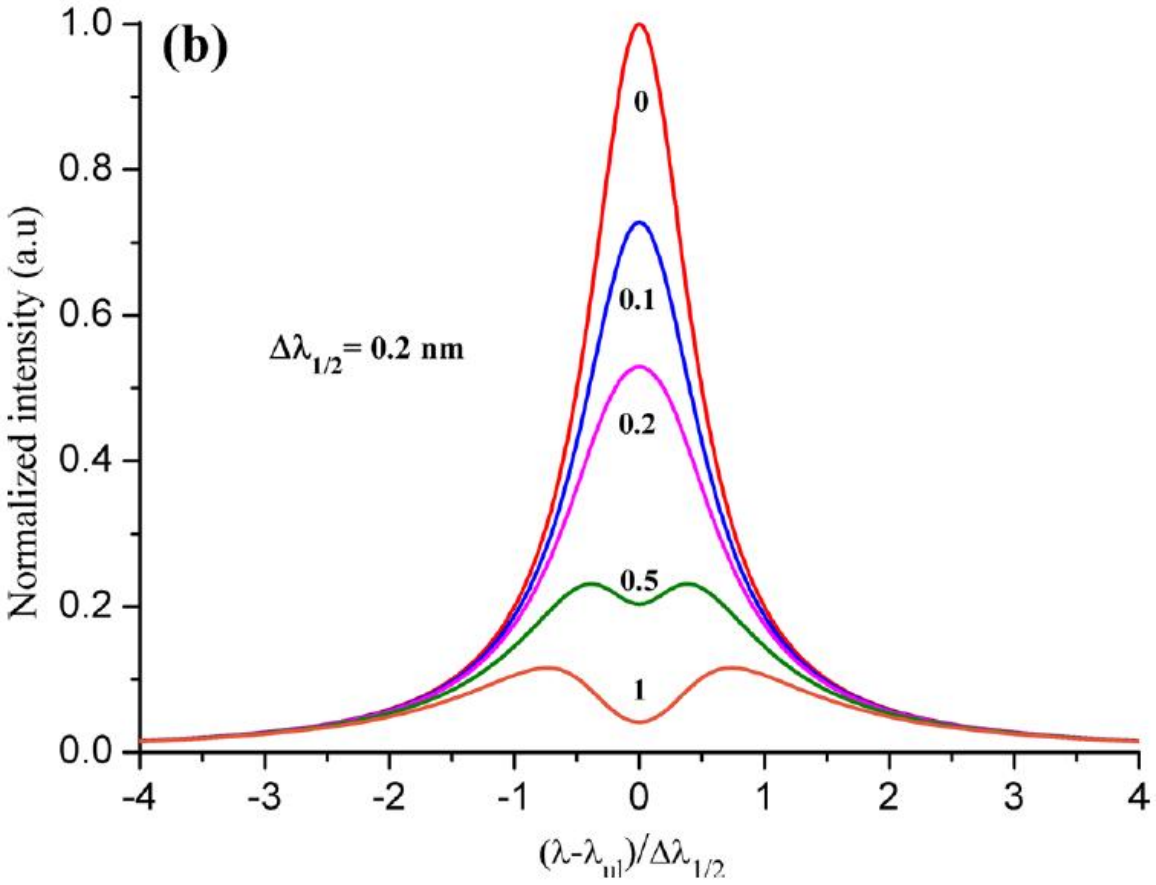

Figure 11: Influence of the optical thickness on the profile of a Lorentzian line. After Xiong *et al.* (2011). Reproduced with permission from the Journal of Applied Physics (AIP Publishing).

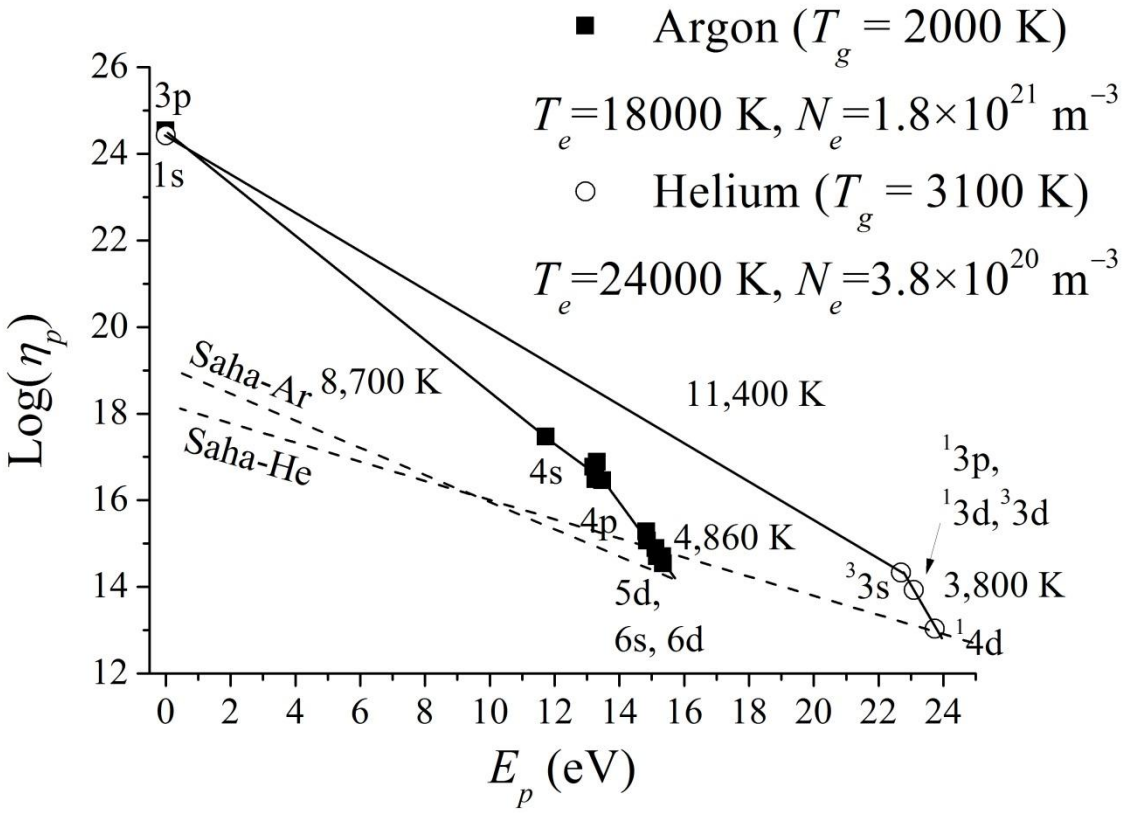

Figure 12: The atomic state distribution functions (ASDF) in helium and in argon for a "torche à injection axiale" (TIA). After (Jonkers *et al.* 1996) and (Timmermans *et al.* 2003).

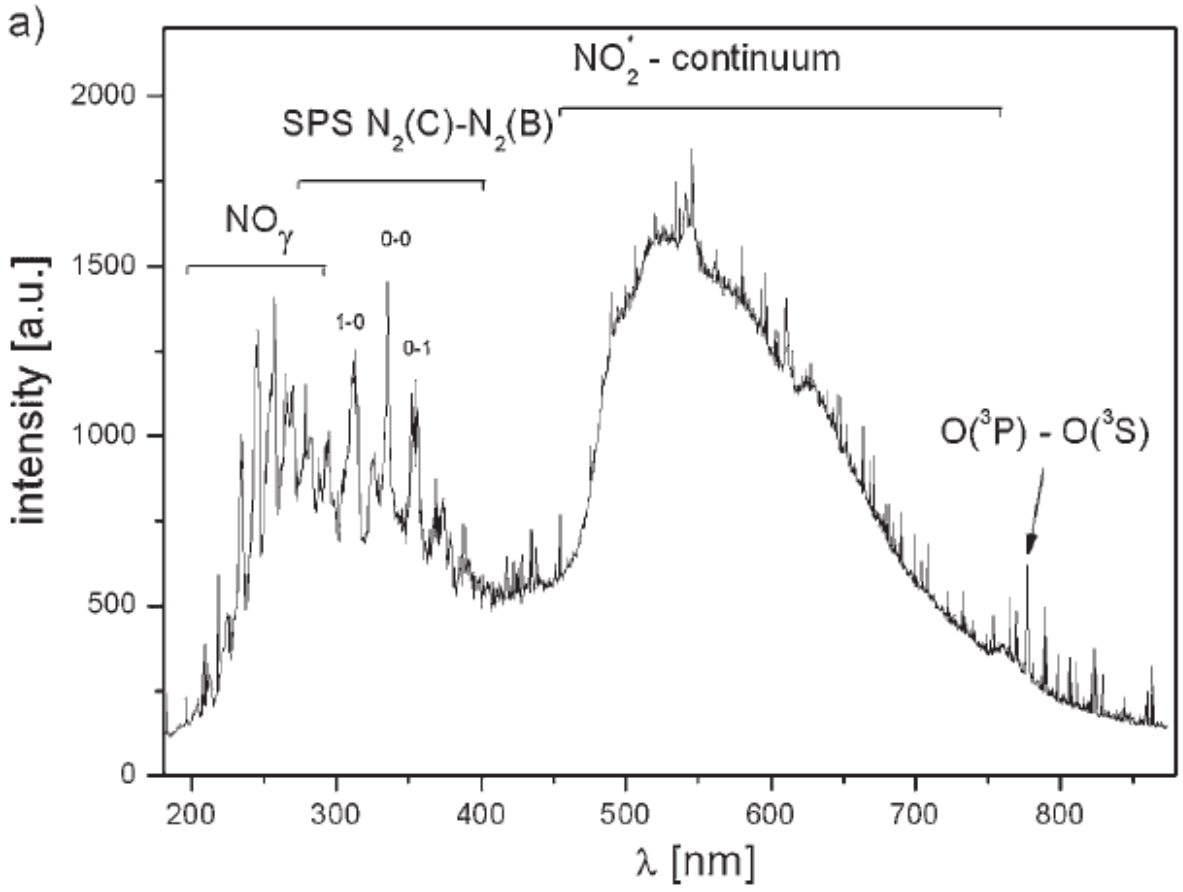

Figure 13: Continuum emission observed 3-4 mm from the nozzle of an atmospheric pressure plasma jet system in dry air. After (Lommatzsch *et al.* 2007). Reproduced with permission from Plasma Processes and Polymers (WILEY-VCH Verlag GmbH & Co. KGaA)

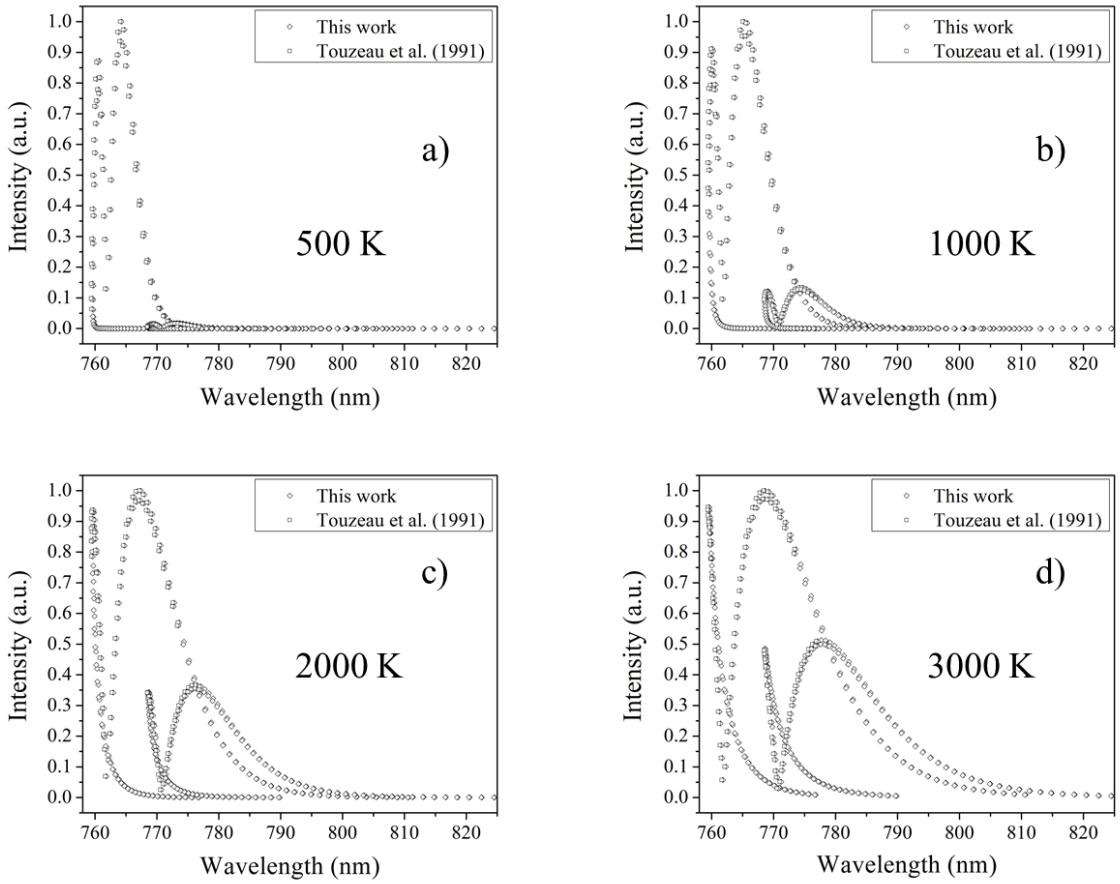

Figure 14: Theoretical intensity of the $O_2\left(b^1\Sigma_g^+, v'=0\right)\rightarrow O_2\left(^3\Sigma_g^-, v''=0\right)$ and $O_2\left(b^1\Sigma_g^+, v'=1\right)\rightarrow O_2\left(^3\Sigma_g^-, v''=1\right)$ transitions of the O_2 atmospheric band. Comparison between the present set of data and the one given by Touzeau *et al.* (1991).

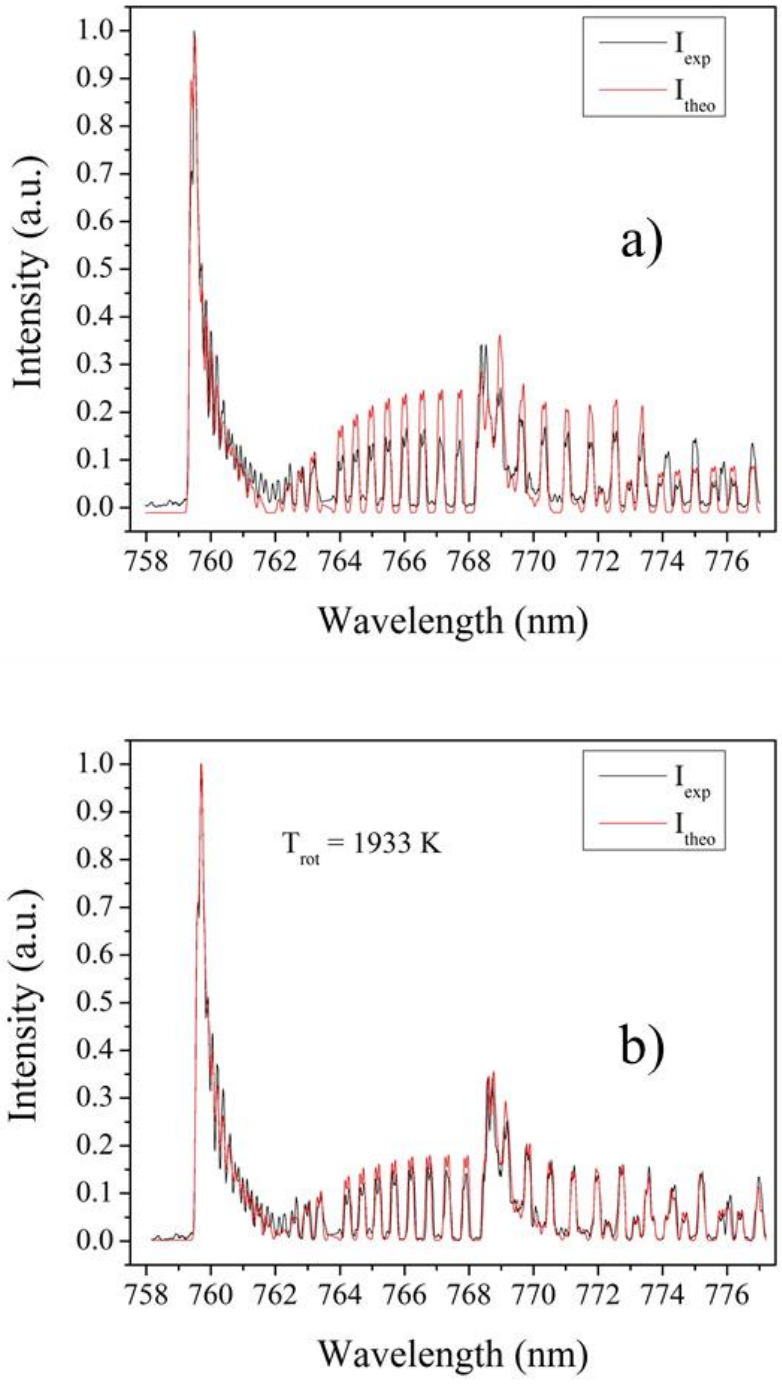

Figure 15: Synthetic spectrum the $O_2\left(b^1\Sigma_g^+, v'=0\right)\rightarrow O_2\left(^3\Sigma_g^-, v''=0\right)$ and $O_2\left(b^1\Sigma_g^+, v'=1\right)\rightarrow O_2\left(^3\Sigma_g^-, v''=1\right)$ transitions of the O_2 atmospheric band. a) Best fit with the data set by Touzeau *et al.* (1991). b) Best fit with the present data set. Microwave afterglow of a resonant cavity plasma. Ar-10%vol.O_2. Total flow rate: 1.1 standard litre per minute. Power: 500 W.

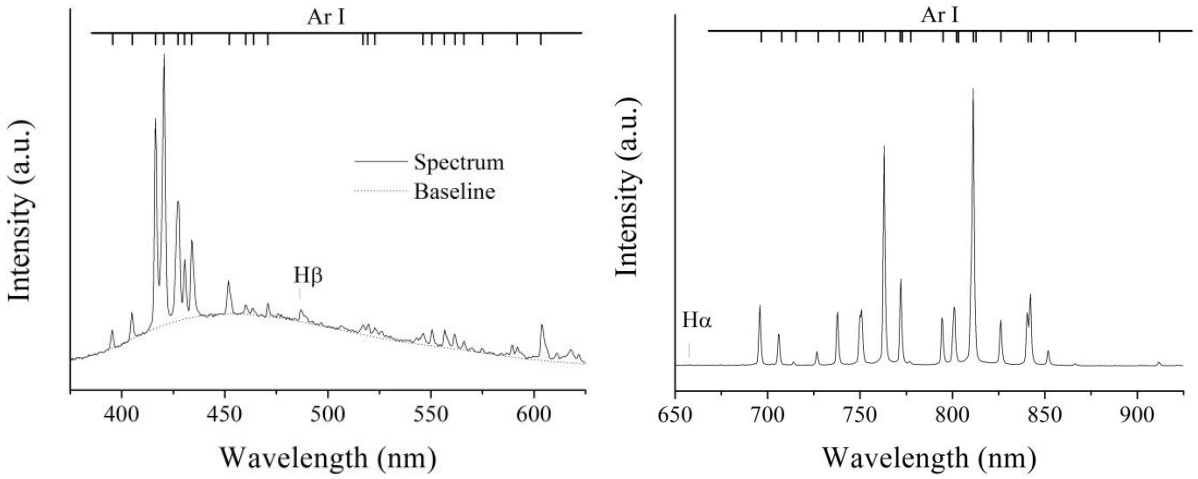

Figure 16: Optical emission spectrum of an argon surface-wave discharge at atmospheric pressure generated in a fused silica tube of 1 mm in inner diameter. (Flow rate = 1 standard litre per minute. Power = 71 W).

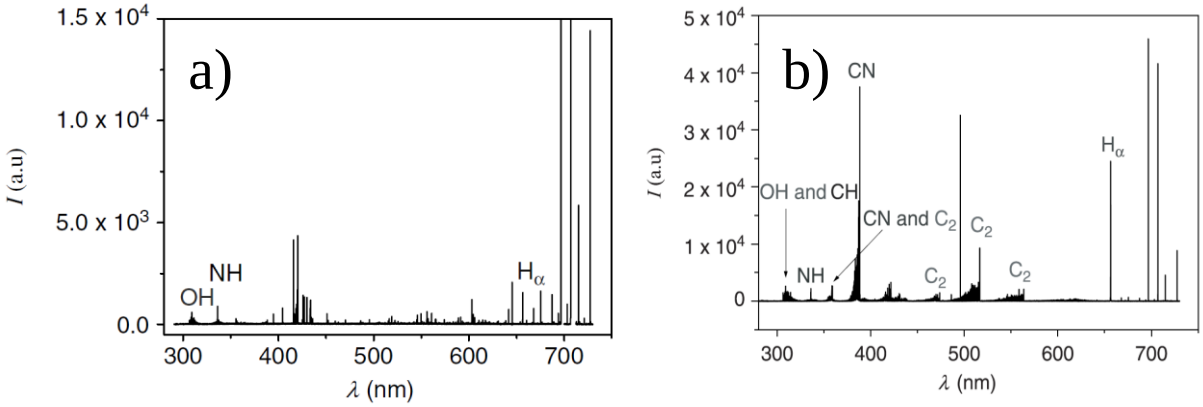

Figure 17: a) Optical emission spectrum of an argon surface-wave discharge at atmospheric pressure generated in a fused silica tube of 1.5 mm in inner diameter. b) Typical optical emission spectrum for an argon-alcohol mixture, the alcohol being either methanol, ethanol, butanol or propanol diluted at 20%. (Flow rate = 0.5 standard litre per minute. Power = 200 W). After (Jiménez *et al.* 2008). Reproduced with permission from Journal of Physics D: Applied Physics (Institute of Physics Publishing).

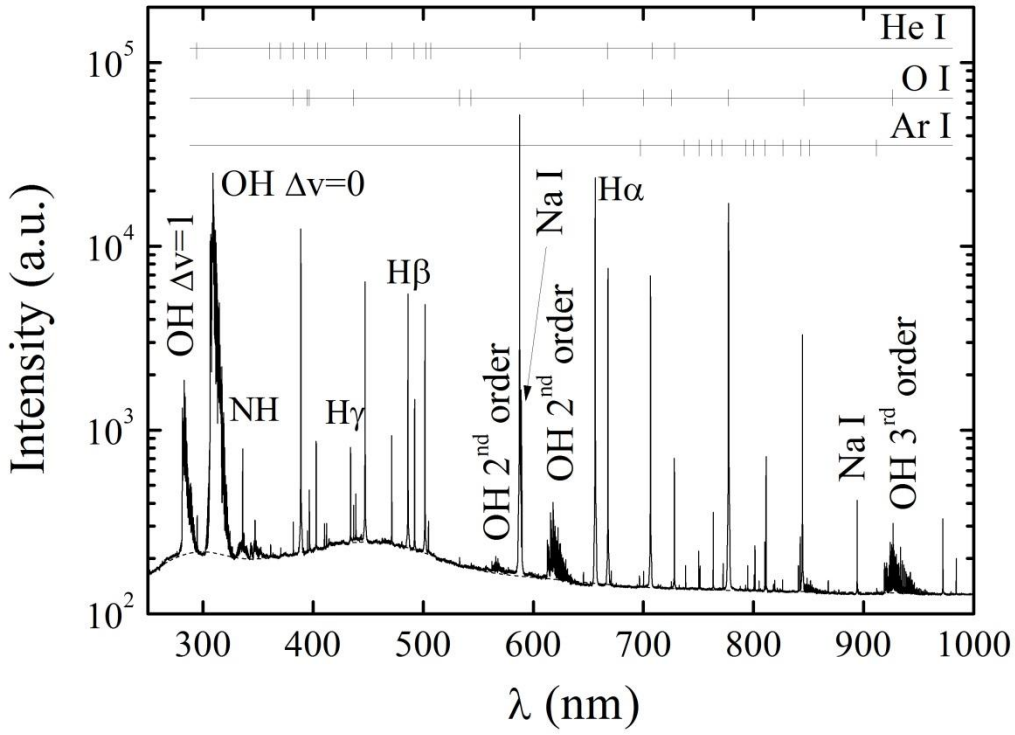

Figure 18: a) Optical emission spectrum of a helium surface-wave discharge at atmospheric pressure generated in a fused silica tube of 3 mm in inner diameter, after (Santos *et al.* 2014). (Flow rate = 2.1 standard litre per minute. Power = 180 W).

E_n (cm^{-1})	g_n	ω_e (cm^{-1})	$\omega_e x_e$ (cm^{-1})	$\omega_e y_e$ (cm^{-1})	B_e (cm^{-1})	D_e (cm^{-1})	α_e (cm^{-1})	β_e (cm^{-1})	r_e (Å)	State
0.000000×10^{0}	1	4.40121×10^{3}	1.21336×10^{2}	-8.12900×10^{-1}	6.08530×10^{1}	4.710×10^{-2}	3.0622×10^{0}	-1.822162×10^{-3}	0.74144	$X(^1\Sigma_g^+)$
0.000000×10^{0}		*8.74276×10^{-20}*	*2.41027×10^{-21}*	*-1.61478×10^{-23}*	*1.20881×10^{-21}*	*9.35616×10^{-25}*	*6.08289×10^{-23}*	*-3.61963×10^{-26}*	*7.4144×10^{-11}*	
9.170000×10^{4}	1	1.35809×10^{3}	2.08880×10^{1}	0.00000×10^{0}	2.00154×10^{1}	1.625×10^{-2}	1.1845×10^{0}	-2.969771×10^{-3}	1.29282	$B(^1\Sigma_u^+)$
1.82157×10^{-18}		*2.69777×10^{-20}*	*4.14929×10^{-22}*	*0.000000×10^{0}*	*3.97595×10^{-22}*	*3.22797×10^{-25}*	*2.35294×10^{-23}*	*-5.89928×10^{-26}*	*1.29282×10^{-10}*	
9.583850×10^{4}	6	2.46689×10^{3}	6.35100×10^{1}	5.52000×10^{-1}	3.10700×10^{1}	1.950×10^{-2}	1.4250×10^{0}	-5.912423×10^{-4}	1.03760	$c^3\Pi_u$
1.90378×10^{-18}		*4.90034×10^{-20}*	*1.26159×10^{-21}*	*1.09652×10^{-23}*	*6.17189×10^{-22}*	*3.87357×10^{-25}*	*2.83069×10^{-23}*	*-1.17447×10^{-26}*	*1.0376×10^{-10}*	
9.593610×10^{4}	3	2.66483×10^{3}	7.16500×10^{1}	9.20000×10^{-1}	3.42160×10^{1}	2.160×10^{-2}	1.6710×10^{0}	-7.954318×10^{-4}	0.98879	$a^3\Sigma_g^+$
1.90572×10^{-18}		*5.29354×10^{-20}*	*1.42329×10^{-21}*	*1.82753×10^{-23}*	*6.79682×10^{-22}*	*4.29072×10^{-25}*	*3.31935×10^{-23}*	*-1.58008×10^{-26}*	*9.8879×10^{-11}*	
1.000823×10^{5}	1	2.58890×10^{3}	1.30500×10^{2}	0.00000×10^{0}	3.26800×10^{1}	2.280×10^{-2}	1.8180×10^{0}	2.619563×10^{-3}	1.01180	$E(^1\Sigma_g^+)$
1.988081×10^{-18}		*5.14271×10^{-20}*	*2.59231×10^{-21}*	*0.000000×10^{0}*	*6.49170×10^{-22}*	*4.52910×10^{-25}*	*3.61136×10^{-23}*	*5.20362×10^{-26}*	*1.0118×10^{-10}*	
1.009110×10^{5}	1	1.19900×10^{3}	0.00000×10^{0}	0.00000×10^{0}	0.00000×10^{0}	0.000×10^{0}	0.0000×10^{0}	0.000000×10^{0}	~2.32	$F(^1\Sigma_g^+)$
2.00454×10^{-18}		*2.38175×10^{-20}*	*0.00000×10^{0}*	*0.00000×10^{0}*	*0.00000×10^{0}*	*0.000×10^{0}*	*0.0000×10^{0}*	*0.000000×10^{0}*	*$\sim2.32\times10^{-10}$*	

Table 1: Molecular constants of some H_2 states. For all theses states, $\omega_e z_e$=0.0, γ_e=0.0 and H_e=0.0. After (Rosen 1970) and (NIST 2014). Conversion to Joules (SI units –values in italics) is obtained by multiplying each term expressed in cm^{-1} by $100\cdot h\cdot c=1.98644568\times10^{-23}$. r_e in Å is converted in m.

α	$S(\alpha)$	$B(\alpha)$	$S(\alpha)/2B(\alpha)$
1.00E-04	-0.438	0.301	-0.728
2.00E-04	-0.439	0.301	-0.729
5.00E-04	-0.441	0.301	-0.733
1.00E-03	-0.441	0.299	-0.737
2.00E-03	-0.432	0.299	-0.722
5.00E-03	-0.430	0.308	-0.698
1.00E-02	-0.432	0.288	-0.750
2.00E-02	-0.449	0.280	-0.802
3.00E-02	-0.390	0.311	-0.627
4.00E-02	-0.442	0.336	-0.658
5.00E-02	-0.500	0.332	-0.753
6.00E-02	-0.534	0.317	-0.842
8.00E-02	-0.557	0.284	-0.981
1.00E-01	-0.548	0.258	-1.062
1.50E-01	-0.496	0.222	-1.117
2.00E-01	-0.444	0.207	-1.072
3.00E-01	-0.366	0.199	-0.920
5.00E-01	-0.274	0.206	-0.665
1.00E+00	-0.166	0.232	-0.358
2.00E+00	-0.076	0.270	-0.141
5.00E+00	0.023	0.332	0.035
1.00E+01	0.088	0.387	0.114
2.00E+01	0.151	0.447	0.169
5.00E+01	0.231	0.539	0.214
1.00E+02	0.293	0.617	0.237
2.00E+02	0.357	0.705	0.253
5.00E+02	0.448	0.838	0.267
1.00E+03	0.525	0.954	0.275
2.00E+03	0.607	1.086	0.279
5.00E+03	0.731	1.285	0.284
1.00E+04	0.837	1.460	0.287

Table 2: Parameters tabulated by Hindmarsh *et al.* (1967) and needed to determine broadening width and line shift caused by collisions with molecules interacting with a Lennard-Jones potential.

$O_2\left(b^1\Sigma_g^+\right)$		$O_2\left(X^3\Sigma_g^-\right)$	
$T_e^{'}$	13195.314 cm^{-1}	λ	1.984 cm^{-1}
$\omega_e^{'}$	1432.6661 cm^{-1}	γ	-0.0084 cm^{-1}
$\omega_e^{'}x_e^{'}$	13.9336 cm^{-1}	$\omega_e^{''}$	1580.1932 cm^{-1}
$\omega_e^{'}y_e^{'}$	-0.0143 cm^{-1}	$\omega_e^{''}x_e^{''}$	11.980804 cm^{-1}
$B_0^{'}$	1.391382 cm^{-1}	$\omega_e^{''}y_e^{''}$	0.047474736 cm^{-1}
$D_0^{'}$	5.486×10^{-6} cm^{-1}	$B_0^{''}$	1.43768 cm^{-1}
$B_1^{'}$	1.373135 cm^{-1}	$D_0^{''}$	5.02×10^{-6} cm^{-1}
$D_1^{'}$	5.586×10^{-6} cm^{-1}	$B_1^{''}$	1.4220 cm^{-1}
		$D_1^{''}$	4.8 cm^{-1}

Branch	ΔK ; ΔJ		S(J',J'')
^{R}R	+1 ; +1	$J'' = K''$	½ J"
^{R}Q	+1 ; 0	$J'' = K'' + 1$	½(J''+¼)
^{P}P	-1 ; -1	$J'' = K''$	½(J''+¾)
^{P}Q	-1 ; 0	$J'' = K''$-1	½(J''+1)

Table 3: Spectroscopic constants and Höln-London factors required to simulate the $O_2\left(b^1\Sigma_g^+, v'=0\right)\rightarrow O_2\left(^3\Sigma_g^-, v''=0\right)$ and $O_2\left(b^1\Sigma_g^+, v'=1\right)\rightarrow O_2\left(^3\Sigma_g^-, v''=1\right)$ atmospheric band transitions.